Università degli Studi di Milano-Bicocca
Dipartimento di Fisica "Giuseppe Occhialini"

The CERN implementation of the ENUBET/nuSCOPE beamline

Academic Year 2024-2025

Candidate:
Matteo Capitani
Student ID:
865438

Supervisor:
Prof. Francesco Terranova
Co-relators:
Dott. Antonio Branca
Dott. Nikolaos Charitonidis

SALVIATI: *Or vedete come è facile da intendersi.*
SAGREDO: *Tali son tutte le cose vere, doppo che son trovate;*
ma il punto sta nel saperle trovare.

Galileo Galilei
Dialogo sopra i due massimi sistemi del mondo

Abstract

Neutrino physics has entered an era of precision measurements, driven by the goal of resolving fundamental questions such as the existence of CP violation in the lepton sector, the neutrino mass ordering, and the precise values of oscillation parameters. Next-generation long-baseline experiments, namely the Deep Underground Neutrino Experiment (DUNE) and Hyper-Kamiokande, are set to address these questions with unprecedented statistical power. However, their ultimate sensitivity will be constrained by systematic uncertainties, which are currently dominated by an incomplete understanding of neutrino-nucleus interaction cross-sections in the intermediate energy range. Reducing these uncertainties from the current 10-20% level to the percent level is therefore key to reaching ultimate precision for the future neutrino oscillation program.

This thesis presents a comprehensive design study for the nuSCOPE (Neutrino SPS COmplex for Precision Experiments) facility, a next-generation short-baseline experiment conceived to address this challenge. nuSCOPE is based on the novel concept of a *monitored* and *tagged* neutrino beam, capable of providing a measurement of the neutrino flux with an accuracy of $\sim 1\%$, an order of magnitude improvement over existing facilities. Such precision will enable high-resolution measurements of absolute neutrino cross-sections, providing essential data to tune and validate the interaction models used by DUNE and Hyper-Kamiokande.

The work detailed in this thesis is based on a complete, end-to-end design of the nuSCOPE beamline, optimized for implementation at the CERN Super Proton Synchrotron (SPS) by CERN in the framework of Physics Beyond Collider. The proposed facility utilizes a 400 GeV slow-extracted proton beam impinging on a graphite target to produce a narrow-band beam of K^+ and π^+ mesons with a central momentum of 8.5 GeV and a momentum spread of 10%. The beamline optics, comprising a static focusing system of quadrupole and dipole magnets, was optimized using a multi-objective genetic algorithm to maximize the meson yield while ensuring the beam remains parallel through a 40-meter-long instrumented decay tunnel. This thesis presents the detailed configuration of all key components, including the target, a novel collimator design, the magnetic transfer line, and the hadron dump, with a proposed implementation in the existing TT61 tunnel at CERN.

The feasibility and robustness of the proposed design were validated through extensive Monte Carlo simulations using the FLUKA code. Two critical aspects were investigated

in depth: thermal effects on beamline components and the radiological assessment of the facility. The thermal analysis shows that the highest energy deposition occurs in the graphite target, leading to a peak temperature increase of approximately 402 K per beam pulse. A subsequent analysis of the induced thermo-mechanical stresses confirms that the peak Von Mises stress of 12.2 MPa remains well within the structural limits of graphite, ensuring the target's integrity. The temperature rise in other components, such as the copper collimator ($\sim$ 16 K), is modest, eliminating the need for complex active cooling systems.

The radiation protection study demonstrates the effectiveness of the proposed shielding, composed of cast iron and concrete. Prompt dose rate simulations confirm that the shielding is sufficient to allow for emergency access to the experimental tunnel during operation. The analysis of residual dose rates provides information for planning maintenance and intervention scenarios, identifying radiological hotspots while confirming that most areas become accessible after short cooling periods. A particular focus was placed on potential radiation damage of the silicon pixel trackers, which are essential for the neutrino tagging technique. The studies show that the total dose and the 1-MeV-neutron-equivalent fluence on the most exposed tracker are within the operational limits of current and proposed radiation-hard technologies.

In conclusion, this thesis delivers a complete and self-consistent design for the nuSCOPE facility. The detailed studies confirm that the proposed beamline is technically feasible, radiologically safe, and capable of meeting the demanding performance requirements for a new generation of precision neutrino cross-section measurements.

Contents

Chapter 1

Introduction to Neutrino Physics

This chapter will present an introduction to neutrino physics, beginning with the proposal of neutrino existence by W. Pauli and its discovery in 1956. Secondly, a brief overview of the phenomenology of neutrino oscillation is presented. The last sections will be devoted to the analysis of neutrino cross-sections and the main experiments that measure them.

1.1 Standard Model Neutrinos

Neutrinos are among the most elusive and mysterious particles of the Standard Model. They are leptons, with no electric charge and extremely small masses. They interact only through weak, gravitational interaction; this makes them particularly difficult to detect.

1.1.1 Discovery of the Neutrino

The birth of the neutrino dates back to the 1930s, when the beta decay spectrum of ^{210}Bi was first measured [1]. If only the electron and the recoiling nucleus were produced in beta decay, the energy spectrum would have appeared as a monochromatic line at the Q-value. Instead, what was observed was a continuous spectrum with an endpoint at the Q-value. To explain this result, two main hypotheses were considered: either the conservation of energy and momentum holds only statistically (as proposed by N. Bohr), or a new, undetectable particle, the neutrino, is emitted, carrying away the missing energy and spin (as suggested by W. Pauli). In a famous letter, Pauli proposed his solution to this puzzle: a new particle with half-integer spin, produced alongside the electron, that escapes detection [2].

History proved Pauli right. In 1956, at the Savannah River nuclear reactor in the USA, C. Cowan and F. Reines confirmed the existence of neutrinos [3]. The detection was based on the inverse beta decay reaction:

$$\bar{\nu}_e + p \rightarrow e^+ + n \tag{1.1}$$

The detection principle relied on the coincident measurement of photons from both the positron annihilation and the neutron capture reaction. Cowan and Reines used a water tank containing dissolved $CdCl_2$ to enhance the neutron capture cross-section, surrounded by 4200 L of liquid scintillator. The measured cross-section was:

$$\bar{\sigma} = (11 \pm 3) \cdot 10^{-44}\ \text{cm}^{-2} \tag{1.2}$$

In 1995, F. Reines was honoured with the Nobel Prize for his work on neutrino physics.

1.1.2 Neutrinos and Antineutrinos

In 1955, and even today, an open question in neutrino physics was whether neutrinos and antineutrinos were the same particle. If that were the case, the following reactions:

$$\nu_e + n \to e^- + p \tag{1.3}$$

$$\bar{\nu}_e + n \to e^- + p \tag{1.4}$$

should occur with the same cross-section. To test this, R. Davis performed an experiment at the Brookhaven nuclear reactor in the USA [4], searching for the reaction:

$$\bar{\nu}_e + {}^{37}\text{Cl} \to e^- + {}^{37}\text{Ar} \tag{1.5}$$

He used 4000 L of carbon tetrachloride (CCl_4) as the target medium. After exposure to the reactor antineutrino flux, the produced argon atoms were extracted by bubbling helium through the liquid. These atoms were then detected via their electron capture decays using proportional counters. Since the expected reaction 1.4 was not observed, Davis was able to set an upper limit that effectively demonstrated that ν_e can cause the reaction, whereas $\bar{\nu}_e$ cannot. Note that, in modern language, the 1955 Davis experiment is not a proof of the Dirac nature of neutrinos but only that Dirac neutrinos are different from antineutrinos. The Dirac versus Majorana nature of neutrinos is still an open issue and an active field of investigation. A similar result was later obtained at CERN for the muon neutrino: in interactions of ν_μ beams, only μ^- were observed in the final state [5].

Using similar techniques, R. Davis achieved the first observation of solar neutrinos, a discovery later acknowledged by the 2002 Nobel Prize in Physics.

1.1.3 Discovery of the Second Neutrino

In 1959, B. Pontecorvo investigated whether the neutrino emitted with the electron in β decays is the same as the one emitted in π decays [6]. The experiment was performed at the Brookhaven AGS using a 15 GeV proton beam impinging on a beryllium target [7], which produced the world's first neutrino beam by exploiting the production and decay of secondary pions and kaons. Ten spark chambers, each weighing 1 ton, were installed behind a shielding of 13.5 m of iron in order to filter out all hadrons and the majority of primary muons. By observing the resulting tracks, it was possible to distinguish between electrons and muons. Since a large excess of muon-like events was observed, this led to the conclusion that $\nu_\mu \neq \nu_e$.

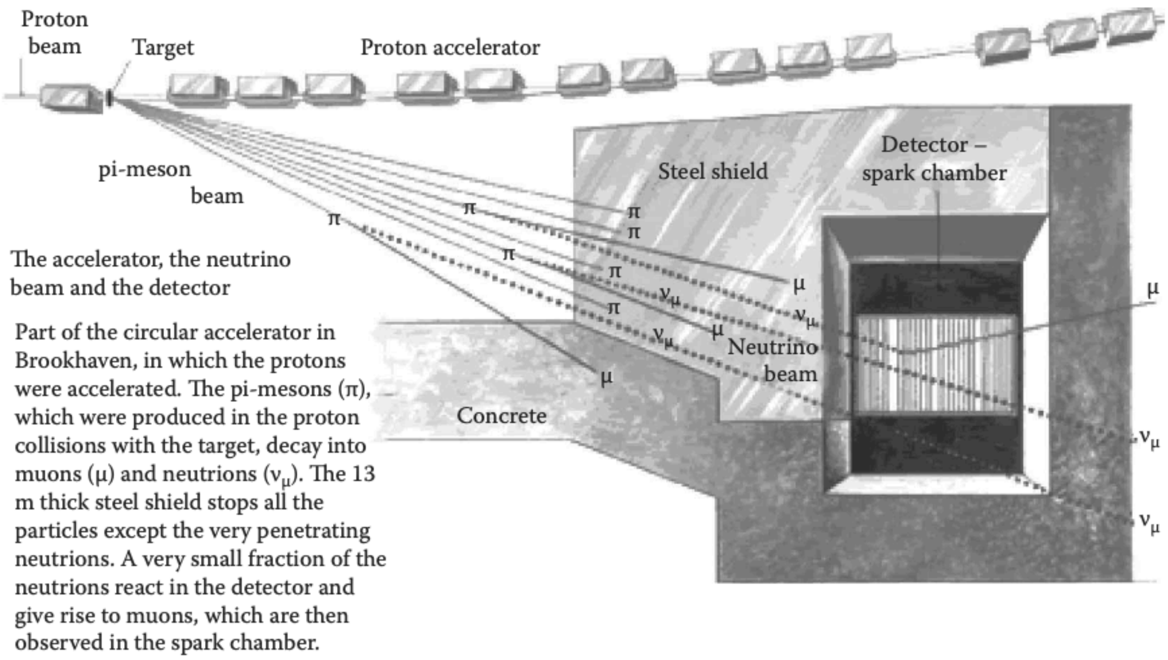

Figure 1.1: Schematic view of the AGS neutrino experiment. Figure taken from [2].

For the discovery of the muon neutrino, L. Lederman, M. Schwartz, and J. Steinberger received the Nobel Prize in Physics in 1988.

1.2 Neutrino Oscillations

If neutrinos have non-zero mass, the weak interaction eigenstates do not coincide with the mass eigenstates [8, 9]. This situation is analogous to the quark sector, where the two sets of eigenstates are related by the CKM matrix. The misalignment between the two bases gives rise to the phenomenon of *neutrino oscillations*. These oscillations can be observed as long as the neutrino wave packets maintain quantum coherence, and they result in a violation of the conservation of individual lepton flavour numbers [2].

1.2.1 Lepton Flavour Mixing

The origin of flavour mixing in the leptonic sector lies in the misalignment between the weak interaction eigenstates and the mass eigenstates. Specifically, this occurs because the neutrino mass matrix is not diagonal in the flavour basis, defined as the basis of weak eigenstates corresponding to the charged lepton mass eigenstates (e, μ and τ).

The transformation that relates flavour and mass eigenstate left-handed neutrino fields is encoded in the *lepton mixing matrix*, known as the PMNS (Pontecorvo-Maki-Nakagawa-Sakata) matrix:

$$\begin{pmatrix} \nu_e(x) \\ \nu_\mu(x) \\ \nu_\tau(x) \end{pmatrix}_L = U \begin{pmatrix} \nu_1(x) \\ \nu_2(x) \\ \nu_3(x) \end{pmatrix}_L = \begin{pmatrix} U_{e1} & U_{e2} & U_{e3} \\ U_{\mu 1} & U_{\mu 2} & U_{\mu 3} \\ U_{\tau 1} & U_{\tau 2} & U_{\tau 3} \end{pmatrix} \begin{pmatrix} \nu_1(x) \\ \nu_2(x) \\ \nu_3(x) \end{pmatrix}_L \tag{1.6}$$

In equation 1.6, the fields $\nu_{\ell L}$ represent the left-handed flavour eigenstate neutrinos, defined as those coupling via charged current to the charged leptons. The fields ν_{1L}, ν_{2L} and ν_{3L} are the left-handed neutrino mass eigenstates, with masses m_1, m_2 and m_3, respectively.

In compact form, equation 1.6 becomes:

$$\nu_{\alpha L}(x) = \sum_i U_{\alpha i} \nu_{iL}(x) \tag{1.7}$$

where $\alpha = e, \mu, \tau$ and $i = 1, 2, 3$. As the discussion involves only left-handed SM neutrinos, the subscript L and the space-time dependence x will be omitted henceforth.

As a consequence of flavour mixing, the neutrino that couples to a charged lepton via the charged current interaction is not a mass eigenstate, but rather a *coherent superposition of mass eigenstates*:

$$\mathcal{L}_{CC} = \frac{g}{\sqrt{2}} W_\mu^- \sum_\alpha \bar{\ell}_\alpha \gamma^\mu \nu_\alpha + \text{h.c.} = \frac{g}{\sqrt{2}} W_\mu^- \sum_\alpha \bar{\ell}_\alpha \gamma^\mu \sum_i U_{\alpha i} \nu_i + \text{h.c.} \tag{1.8}$$

Since it connects two orthonormal bases, the PMNS matrix must be unitary. A general 3×3 unitary matrix can be parametrized using three mixing angles and six phases. However, not all these phases are physically meaningful, as some can be eliminated by rephasing the fields.

If neutrinos are Dirac fermions, both the charged lepton and neutrino fields can be rephased:

$$\begin{aligned} \ell_\alpha &\longmapsto e^{i\phi_\alpha} \ell_\alpha \\ \nu_i &\longmapsto e^{i\phi_i} \nu_i \end{aligned} \tag{1.9}$$

The charged current interaction in equation 1.8 remains invariant if the PMNS matrix is transformed as:

$$U_{\alpha i} \longmapsto e^{i(\phi_\alpha - \phi_i)} U_{\alpha i} \tag{1.10}$$

There are five independent phase differences, so five unphysical phases can be absorbed, leaving only one physical CP-violating phase, similarly to the case of the CKM matrix in the quark sector.

If neutrinos are instead Majorana fermions, their mass terms are not invariant under field rephasing. Only the charged lepton fields can be redefined:

$$U_{\alpha i} \longmapsto e^{i\phi_\alpha} U_{\alpha i} \tag{1.11}$$

This means that three physical CP-violating phases remain in the Majorana case: one Dirac-like phase and two additional Majorana phases.

The PMNS matrix can therefore be written as the product of three rotation matrices with mixing angles θ_{12}, θ_{13}, θ_{23}, and a Dirac CP-violating phase δ_{CP}:

$$\begin{aligned} U &= \begin{pmatrix} 1 & 0 & 0 \\ 0 & c_{23} & s_{23} \\ 0 & -s_{23} & c_{23} \end{pmatrix} \begin{pmatrix} c_{13} & 0 & s_{13}e^{-i\delta_{CP}} \\ 0 & 1 & 0 \\ -s_{13}e^{i\delta_{CP}} & 0 & c_{13} \end{pmatrix} \begin{pmatrix} c_{12} & s_{12} & 0 \\ -s_{12} & c_{12} & 0 \\ 0 & 0 & 1 \end{pmatrix} P \\ &= \begin{pmatrix} c_{12}c_{13} & s_{12}c_{13} & s_{13}e^{-i\delta_{CP}} \\ -s_{12}c_{23} - c_{12}s_{13}s_{23}e^{i\delta_{CP}} & c_{12}c_{23} - s_{12}s_{13}s_{23}e^{i\delta_{CP}} & c_{13}s_{23} \\ s_{12}s_{23} - c_{12}s_{13}c_{23}e^{i\delta_{CP}} & -c_{12}s_{23} - s_{12}s_{13}c_{23}e^{i\delta_{CP}} & c_{13}c_{23} \end{pmatrix} P \end{aligned} \tag{1.12}$$

where $c_{ij} \equiv \cos\theta_{ij}$ and $s_{ij} \equiv \sin\theta_{ij}$. The matrix P is the identity in the Dirac case or a diagonal matrix containing the two Majorana phases in the Majorana case. Without loss of generality, one can choose the mixing angles in the range $\theta_{ij} \in \left[0, \frac{\pi}{2}\right]$ and the CP phase $\delta_{CP} \in [0, 2\pi[$.

The Majorana phases do not affect neutrino oscillation probabilities but can appear in lepton number violating processes such as neutrino-less double beta decay. On the other hand, the Dirac phase δ_{CP} can induce CP violation in neutrino oscillations, resulting in different oscillation probabilities for neutrinos and antineutrinos in vacuum [10].

1.2.2 Neutrino Oscillations in Vacuum

If neutrinos have masses and lepton flavour are mixed in CC interactions, lepton flavour is not conserved in neutrino propagation. This phenomenon is referred to as *neutrino oscillations*.

A weak eigenstate, ν_α, which is the state produced in the weak charged current interaction of a charged lepton ℓ_α, is the linear combination determined by the mixing matrix U[1] [11].

$$|\nu_\alpha(t=0)\rangle = |\nu_\alpha\rangle = \sum_{i=1}^{n} U^*_{\alpha i} |\nu_i\rangle \tag{1.13}$$

[1] It should be noted that the relation between flavour and mass eigenstate neutrino states involves the complex conjugate of the PMNS matrix, rather than the matrix itself as used for neutrino fields. This arises because the quantum field $\nu_\alpha(x)$ annihilates a neutrino of flavour α, whereas the neutrino state $|\nu_\alpha(\boldsymbol{p})\rangle$ is defined by the action of the corresponding creation operator $a^\dagger_\alpha(\boldsymbol{p})$ on the vacuum. For antineutrinos, the field takes the form $\bar{\nu}_\alpha(x) = \sum_i U^*_{\alpha i}\bar{\nu}_i(x)$, leading to the flavour eigenstate $|\bar{\nu}_\alpha\rangle = \sum_i U_{\alpha i} |\bar{\nu}_i\rangle$.

Each mass eigenstate, being an eigenstate of the vacuum Hamiltonian, evolves with its own phase factor $e^{-iE_i t}$, where $E_i = \sqrt{p^2 + m_i^2}$. This affects the coherent superposition, which no longer corresponds to a pure flavour eigenstate, as the non-zero neutrino mass introduces phase differences among the three eigenstates.

$$|\nu(t)\rangle = \sum_i U^*_{\alpha i} e^{-iE_i t} |\nu_i\rangle = \sum_i U^*_{\alpha i} e^{-iE_i t} \sum_\beta U_{\beta i} |\nu_\beta\rangle \tag{1.14}$$

The probability amplitude for a neutrino produced in the flavour eigenstate ν_α to be detected as flavour ν_β at time t is given by the square modulus of the scalar product of the two states [10]:

$$P(\nu_\alpha \to \nu_\beta) = |\langle \nu_\beta \rangle \, \nu(t)|^2 = \left| \sum_i U_{\beta i} U^*_{\alpha i} e^{-iE_i t} \right|^2 \tag{1.15}$$

Since neutrinos are ultra-relativistic particles ($E \simeq p$) in all practical contexts, the energy can be approximated as[2]:

$$E_i = \sqrt{p^2 + m_i^2} \simeq p + \frac{m_i^2}{2E} \tag{1.16}$$

Accordingly, the neutrino oscillation probability takes the form:

$$\begin{aligned} P(\nu_\alpha \to \nu_\beta) = \delta_{\alpha\beta} &- 4 \sum_{i<j} \mathrm{Re}\{U_{\alpha i} U^*_{\beta i} U^*_{\alpha j} U_{\beta j}\} \sin^2\left(\frac{\Delta m^2_{ji} L}{4E}\right) \\ &+ 2 \sum_{i<j} \mathrm{Im}\{U_{\alpha i} U^*_{\beta i} U^*_{\alpha j} U_{\beta j}\} \sin\left(\frac{\Delta m^2_{ji} L}{2E}\right) \end{aligned} \tag{1.17}$$

where $\Delta m^2_{ji} \equiv m_j^2 - m_i^2$ and $L \simeq ct$ denotes the distance travelled by neutrinos. For antineutrino oscillations, the matrix U must be replaced by its complex conjugate U^* in equation 1.17. Several observations can be made from Eq. 1.17:

First, neutrino oscillations require non-degenerate neutrino masses ($\Delta m^2_{ji} \neq 0$) and non-trivial flavour mixing ($U \neq$). The oscillation probability depends on the mixing angles θ_{12}, θ_{13}, and θ_{23}, as well as on two independent mass-squared differences, Δm^2_{21} and Δm^2_{32}. Oscillations also depend on the Dirac CP-violating phase δ_{CP}, but not on the Majorana phases. As a result, Dirac and Majorana neutrinos exhibit identical oscillation probabilities. This feature arises from the fact that neutrino oscillations conserve total lepton number, while the Majorana nature of neutrinos manifests only in processes that violate lepton number.

Another consequence of Eq. 1.17 is that CP violation, specifically the condition $P(\bar{\nu}_\alpha \to$

[2]This approximation is justified by the fact that the most recent measurements of neutrino masses provide upper limits: 0.8 eV for the ν_e, 0.19 MeV for the ν_μ, and 18 MeV for the ν_τ, all of which are several orders of magnitude smaller than typical neutrino energies.

$\bar{\nu}_\beta) \neq P(\nu_\alpha \to \nu_\beta)$, is possible only in appearance channels ($\beta \neq \alpha$), not in disappearance channels ($\beta = \alpha$). In fact, the survival probability is the same for neutrinos and antineutrinos:

$$P(\nu_\alpha \to \nu_\alpha) = 1 - 4 \sum_{i<j} |U_{\alpha i} U_{\alpha j}|^2 \sin^2 \left(\frac{\Delta m^2_{ji} L}{4E} \right) = P(\bar{\nu}_\alpha \to \bar{\nu}_\alpha) \tag{1.18}$$

because the combination $U_{\alpha i} U^*_{\beta i} U^*_{\alpha j} U_{\beta j}$ is real for $\alpha = \beta$ [10].

In many experimental contexts, the subleading terms in equation 1.17 can be neglected, allowing neutrino oscillations to be described using the two-flavour approximation[3]:

$$P(\nu_\alpha \to \nu_\beta) = P(\bar{\nu}_\alpha \to \bar{\nu}_\beta) = \sin^2 2\theta \sin^2 \left(\frac{\Delta m^2 L}{4E} \right) \tag{1.19}$$

In this simplified case, the oscillation amplitude is given by $\sin^2 2\theta$, while the oscillation length is proportional to the neutrino energy and inversely proportional to the squared mass difference:

$$L_{\text{osc.}}[\text{km}] = 2.48 \frac{E[\text{GeV}]}{\Delta m^2[\text{eV}^2]} \tag{1.20}$$

Consequently, the oscillation probability[4] becomes

$$P(\nu_\alpha \to \nu_\beta) = \sin^2 2\theta \sin^2 \left(\frac{\pi L}{L_{\text{osc.}}} \right) \tag{1.21}$$

The two-flavour approximation has been extensively employed for decades, prior to the advent of oscillation experiments capable of probing subdominant effects. In fact, the oscillations of solar and atmospheric neutrinos were found to be well described within the two-flavour framework using the parameters $(\Delta m^2_{\text{sol}}, \theta_{\text{sol}})$ and $(\Delta m^2_{\text{atm}}, \theta_{\text{atm}})$, respectively, under the conditions $\Delta m^2_{\text{sol}} \ll \Delta m^2_{\text{atm}}$ and both mixing angles being large.

This notation maps onto the three-flavour framework by identifying Δm^2_{sol} with the squared mass difference between ν_2 and ν_1, where the mass eigenstates are labelled such that $m_2 > m_1$. This implies $\Delta m^2_{21} = \Delta m^2_{\text{sol}} > 0$. The atmospheric mass splitting Δm^2_{atm} can then be identified with either $|\Delta m^2_{31}|$ or $|\Delta m^2_{32}|$.

Two possible mass orderings arise: the normal ordering, where $m_1 < m_2 < m_3$ (implying $\Delta m^2_{31} > 0$), and the inverted ordering, where $m_3 < m_1 < m_2$ (also implying $\Delta m^2_{31} > 0$). The mass configuration $m_1 < m_3 < m_2$ is incompatible with the condition $\Delta m^2_{\text{sol}} \ll \Delta m^2_{\text{atm}}$ and is therefore excluded.

If the baseline L and the neutrino energy E are chosen such that $\frac{\Delta m^2_{21} L}{E} \ll 1$, then oscillations can be well approximated by setting $\Delta m^2_{21} = 0$. In this limit, a single oscillation

[3]It is worth noting that, in the two-flavour case, oscillations do not violate CP symmetry.

[4]It is important to remark that the oscillation probability is not sensitive to the sign of Δm^2, nor to the octant of the mixing angle.

"frequency" remains, given by $\Delta m^2_{31} \simeq \Delta m^2_{32}$[5]. The appearance probability simplifies to

$$P(\nu_\alpha \to \nu_\beta) = \sin^2 2\theta^{\text{eff}}_{\alpha\beta} \sin^2\left(\frac{\Delta m^2_{31} L}{4E}\right), \qquad \text{with } \sin^2 2\theta^{\text{eff}}_{\alpha\beta} \equiv 4|U_{\alpha 3} U_{\beta 3}|^2 \quad (\beta \neq \alpha) \tag{1.22}$$

while the survival probability becomes

$$P(\nu_\alpha \to \nu_\alpha) = 1 - \sin^2 2\theta^{\text{eff}}_{\alpha\alpha} \sin^2\left(\frac{\Delta m^2_{31} L}{4E}\right), \qquad \text{with } \sin^2 2\theta^{\text{eff}}_{\alpha\alpha} \equiv 4|U_{\alpha 3}|^2(1 - |U_{\alpha 3}|^2) \tag{1.23}$$

These simplified formulae accurately describe the dominant oscillation behavior in atmospheric neutrinos, long-baseline accelerator experiments, and short-baseline reactor experiments [10].

The disappearance probability for muon neutrinos is given by

$$\begin{aligned} P(\nu_\mu \to \nu_\mu) &= 1 - \left(\cos^2\theta_{13} \sin^2 2\theta_{23} + \sin^4\theta_{23} \sin^2 2\theta_{13}\right) \sin^2\left(\frac{\Delta m^2_{31} L}{4E}\right) \\ &\simeq 1 - \sin^2 2\theta_{23} \sin^2\left(\frac{\Delta m^2_{31} L}{4E}\right) \end{aligned} \tag{1.24}$$

where terms proportional to $\sin^2\theta_{13}$ have been neglected.

The appearance probabilities for electron and tau neutrinos in a muon neutrino beam are instead given by:

$$P(\nu_\mu \to \nu_e) = \sin^2\theta_{23} \sin^2 2\theta_{13} \sin^2\left(\frac{\Delta m^2_{31} L}{4E}\right) \tag{1.25}$$

$$P(\nu_\mu \to \nu_\tau) = \cos^4\theta_{13} \sin^2 2\theta_{23} \sin^2\left(\frac{\Delta m^2_{31} L}{4E}\right) \tag{1.26}$$

It is important to note that the expressions above are subject to corrections from genuine three-flavour effects, which must be taken into account to match the precision of modern experiments.

In the opposite limit, where $\frac{\Delta m^2_{31} L}{E} \gg 1$, the fast oscillations driven by Δm^2_{31} are averaged out, and electron neutrino oscillations become dominated by Δm^2_{21}. Neglecting terms suppressed by $\sin^2\theta_{13}$, one obtains:

$$P(\nu_e \to \nu_e) = P(\bar{\nu}_e \to \bar{\nu}_e) \simeq 1 - \sin^2 2\theta_{12} \sin^2\left(\frac{\Delta m^2_{21} L}{4E}\right) \tag{1.27}$$

Equation 1.27 applies to long-baseline reactor neutrino experiments and to low-energy neutrinos, in the regime where matter effects can be neglected and vacuum oscillations dominate.

[5] This approximation is valid because all the mixing angles are of comparable magnitude.

1.2.3 CP Violation in Neutrino Oscillations

As discussed in Section 1.2.1, neutrino oscillations depend on the Dirac phase of the PMNS matrix, making it possible to observe CP violation in the lepton sector, namely, the fact that neutrinos and antineutrinos can oscillate with different probabilities in vacuum.

The general action of discrete symmetries on oscillation probabilities is given by:

$$P(\nu_\alpha \to \nu_\beta) \xrightarrow{\text{CP}} P(\bar{\nu}_\alpha \to \bar{\nu}_\beta) \tag{1.28}$$

$$\xrightarrow{\text{T}} P(\nu_\beta \to \nu_\alpha) \tag{1.29}$$

$$\xrightarrow{\text{CPT}} P(\bar{\nu}_\beta \to \bar{\nu}_\alpha) \tag{1.30}$$

Assuming CPT invariance, one has $P(\nu_\alpha \to \nu_\beta) = P(\bar{\nu}_\beta \to \bar{\nu}_\alpha)$; this implies that the CP and T-violating asymmetries in oscillations are equal:

$$A_{\alpha\beta} \equiv \frac{P(\nu_\alpha \to \nu_\beta) - P(\bar{\nu}_\alpha \to \bar{\nu}_\beta)}{P(\nu_\alpha \to \nu_\beta) + P(\bar{\nu}_\alpha \to \bar{\nu}_\beta)} = \frac{P(\nu_\alpha \to \nu_\beta) - P(\nu_\beta \to \nu_\alpha)}{P(\nu_\alpha \to \nu_\beta) + P(\nu_\beta \to \nu_\alpha)} \tag{1.31}$$

CPT conservation also implies that there is no CP violation in disappearance channels, i.e. $P(\nu_\alpha \to \nu_\alpha) = P(\bar{\nu}_\alpha \to \bar{\nu}_\alpha)$. CP violation manifests itself when the probability of an oscillation process differs from its CP-conjugate counterpart. A useful observable is

$$\Delta P_{\alpha\beta} = P(\nu_\alpha \to \nu_\beta) - P(\bar{\nu}_\alpha \to \bar{\nu}_\beta) \neq 0 \tag{1.32}$$

which corresponds to twice the CP-odd contribution in the three-flavour oscillation probability (Eq. 1.17) [2].

This quantity can be expressed as:

$$\Delta P_{\alpha\beta} = \pm 16 J \sin\left(\frac{\Delta m^2_{21} L}{4E}\right) \sin\left(\frac{\Delta m^2_{31} L}{4E}\right) \sin\left(\frac{\Delta m^2_{32} L}{4E}\right) \tag{1.33}$$

where

$$J \equiv \text{Im}\left(U_{e1} U^*_{\mu 1} U^*_{e2} U_{\mu 2}\right) \tag{1.34}$$

with a plus sign when (α, β, γ) is an even permutation of (e, μ, τ) and a minus sign otherwise. The quantity J is called the *Jarlskog invariant*[6] and it quantifies CP violation induced by the Dirac phase of the mixing matrix.

In the standard parametrization of the PMNS matrix, J can be written as:

$$J = \frac{1}{8} \cos\theta_{13} \sin 2\theta_{12} \sin 2\theta_{13} \sin 2\theta_{23} \sin\delta_{CP} \tag{1.35}$$

[6] J is called an *invariant* because it does not depend on the phase convention of the PMNS matrix, i.e. it remains unchanged under re-phasing of the lepton fields. Historically, J was introduced to parametrize CP violation in the quark sector [12].

It is clear that CP violation in the lepton sector requires all three mixing angles θ_{ij} to be non-zero and the Dirac phase to differ from both 0 and π. From Eq. 1.33, it also follows that all squared mass differences Δm^2_{ji} must be non-zero – that is, the three neutrino masses must be distinct. These conditions mirror those required for CP violation in the quark sector and can be summarized[7] as:

$$\begin{gathered} \theta_{12} \neq 0, \qquad \theta_{13} \neq 0, \qquad \theta_{23} \neq 0 \\ m_1 \neq m_2, \qquad m_2 \neq m_3, \qquad m_3 \neq m_1 \\ \delta_{CP} \neq 0, \qquad \delta_{CP} \neq \pi \end{gathered} \tag{1.36}$$

From Eq. 1.33, it is also evident that the CP-violating term in oscillations is universal, i.e. independent of the oscillation channel (up to a sign). This follows from the unitarity of the mixing matrix, which implies:

$$\mathrm{Im}\{U_{e1}U^*_{\mu 1}U^*_{e2}U_{\mu 2}\} = -\,\mathrm{Im}\{U_{e1}U^*_{\tau 1}U^*_{e2}U_{\tau 2}\} - \mathrm{Im}\{U_{\mu 1}U^*_{\tau 1}U^*_{\mu 2}U_{\tau 2}\} \tag{1.37}$$

and leads to the relation $\Delta P_{e\mu} = -\Delta P_{e\tau} = \Delta P_{\mu\tau}$.

The above formulae must be corrected in case neutrinos propagate through matter. The probability changes due to matter effects are sensitive to whether $m_3 > m_2$ (normal ordering) or $m_3 < m_2$ (inverted ordering). This feature is employed to establish the neutrino mass pattern by current accelerator neutrino experiments like NOνA and, in particular, by the next-generation DUNE experiment, which employs a particularly long L (1300 km) to enhance matter effects.

1.3 Neutrino Cross-Section

In the 21st century, following the discovery of neutrino oscillations and the resulting confirmation that neutrinos have mass, research efforts have shifted towards a deeper understanding of the origin of neutrino mass and the potential role neutrinos might play in explaining the matter-antimatter asymmetry observed in the Universe. Central to many of these experimental programmes is the need for neutrinos to interact with Standard Model particles. Consequently, a precise knowledge of neutrino cross-sections is a fundamental requirement for the neutrino physics community [13].

Although all known neutrino interactions with matter fall under the electroweak interaction framework (including its radiative corrections), computing the corresponding cross-sections is far from straightforward. In principle, one might expect that writing down the electroweak Lagrangian should suffice; in practice, the situation is much more complex.

[7]Today, these criteria are mostly of academic interest, as all θ_{ij} and Δm^2_{ji} have been measured. For many years, however, the only experimental information available on θ_{13} was an upper bound.

Several challenges arise: uncertainties in the initial state, nuclear effects, final-state interactions, and other complications all contribute to making the theoretical description difficult. Moreover, approximations valid in one energy regime often fail in another.

1.3.1 Neutrino-Electron Interactions

Among all neutrino interactions with matter, neutrino-electron scattering represents the simplest case. At leading order in perturbation theory, these processes can be described as the elastic scattering of neutrinos off free electrons, and their amplitudes can be computed exactly using standard Feynman rules [14].

1.3.1.1 Elastic Scattering

At low energies, neutrinos and antineutrinos can scatter elastically off electrons through the processes:

$$\nu_\alpha + e^- \to \nu_\alpha + e^- \tag{1.38}$$

$$\bar{\nu}_\alpha + e^- \to \bar{\nu}_\alpha + e^- \tag{1.39}$$

These interactions have no kinematic threshold, as the final state particles are the same as the initial ones. Their primary effect is the redistribution of energy and momentum between the outgoing neutrino and electron in the center-of-mass frame.

Figure 1.2 shows the two tree-level Feynman diagrams contributing to neutrino-electron elastic scattering. For ν_e, both charged-current (W exchange) and neutral-current (Z exchange) interactions contribute. In contrast, for $\nu_{\mu,\tau}$ only the neutral-current diagram is relevant.

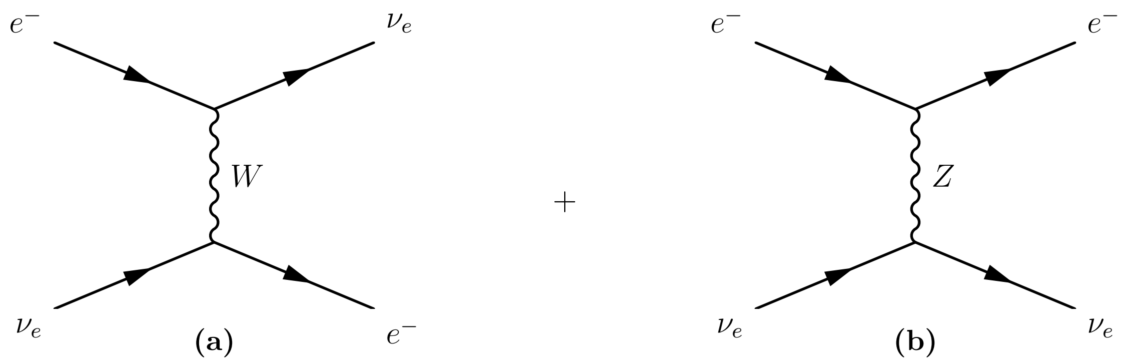

Figure 1.2: The two tree-level Feynman diagrams for the neutrino-electron elastic scattering: charged current (**a**) and neutral current (**b**).

The corresponding diagrams for antineutrino scattering are shown in Fig. 1.3. In this case, the charged-current process proceeds via an s-channel diagram (Fig. 1.3a), unlike the t-channel exchange seen in the neutrino case (Fig. 1.2a).

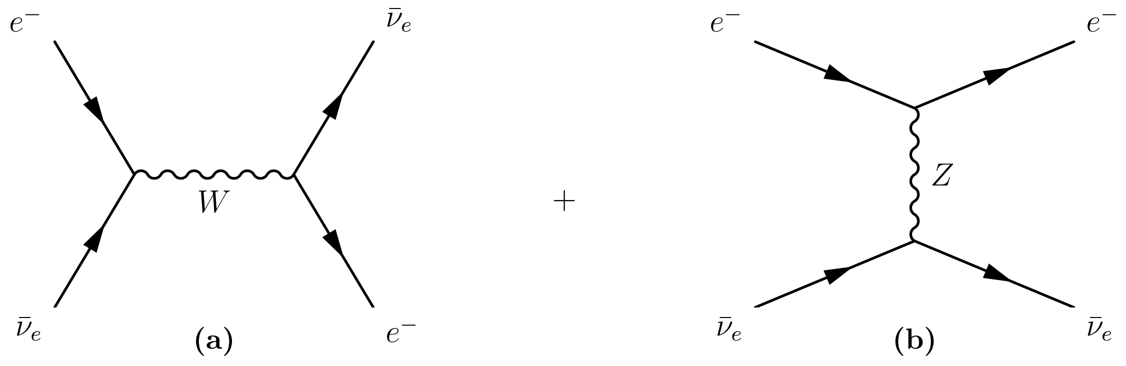

Figure 1.3: The two tree-level Feynman diagrams for the antineutrino-electron elastic scattering: charged current (**a**) and neutral current (**b**).

For the processes involving $\nu_{\mu,\tau}$ and their antiparticles,

$$\overset{(-)}{\nu}_{\mu,\tau} + e^- \to \overset{(-)}{\nu}_{\mu,\tau} + e^-, \tag{1.40}$$

only neutral-current interactions contribute at tree-level.

At energies much smaller than the W and Z boson masses ($s \ll m_W^2, m_Z^2$), the weak interaction can be approximated using an effective four-fermion theory. The low-energy effective Lagrangian for elastic scattering involving electron neutrinos (or antineutrinos) reads:

$$\begin{aligned}\mathcal{L}_{\text{eff}}(\nu_e e^- \to \nu_e e^-) = -\frac{G_F}{\sqrt{2}}\Big\{ &[\bar{\nu}_e \gamma^\rho (1-\gamma^5) e][\bar{e}\gamma_\rho (1-\gamma^5)\nu_e] \\ &+ [\bar{\nu}_e \gamma^\rho (1-\gamma^5)\nu_e][\bar{e}\gamma_\rho (g_V^\ell - g_A^\ell \gamma^5) e]\Big\}\end{aligned} \tag{1.41}$$

The first term corresponds to charged-current exchange, and the second to neutral-current contribution. This can be revised into a compact form:

$$\mathcal{L}_{\text{eff}} = -\frac{G_F}{\sqrt{2}}[\bar{\nu}_e \gamma^\rho (1-\gamma^5)\nu_e]\left\{\bar{e}\gamma_\rho \left[(1+g_V^\ell) - (1+g_A^\ell)\gamma^5\right] e\right\} \tag{1.42}$$

For $\nu_{\mu,\tau}$ and $\bar{\nu}_{\mu,\tau}$ elastic scattering, the effective Lagrangian only contains a neutral-current term:

$$\mathcal{L}_{\text{eff}} = -\frac{G_F}{\sqrt{2}}[\bar{\nu}_\alpha \gamma^\rho (1-\gamma^5)\nu_\alpha][\bar{e}\gamma_\rho (g_V^\ell - g_A^\ell \gamma^5) e] \tag{1.43}$$

Let us consider the general process:

$$\nu_i + e_i^- \to \nu_f + e_f^- \tag{1.44}$$

The Mandelstam variable s, representing the total energy squared in the center-of-mass frame, is defined as:

$$s = (p_{\nu_i} + p_{e_i})^2 = (p_{\nu_f} + p_{e_f})^2 \tag{1.45}$$

The other variables are given by:

$$t = (p_{\nu_i} - p_{\nu_f})^2 = (p_{e_f} - p_{e_i})^2 = q^2 \equiv -Q^2 \tag{1.46}$$

$$u = (p_{\nu_i} - p_{e_f})^2 = (p_{\nu_f} - p_{e_i})^2 \tag{1.47}$$

In general, the cross-section for neutrino-electron scattering scales with $G_F^2\, s$. For $s \gg m_e$, the cross-sections take the approximate form:

$$\nu_e + e^- : \quad \frac{G_F^2 s}{4\pi}\left[(1 + 2\sin^2\theta_W)^2 + \frac{4}{3}\sin^4\theta_W\right] \simeq 93 \text{ s/MeV}^2 \cdot 10^{-46} \text{ cm}^2 \tag{1.48}$$

$$\bar{\nu}_e + e^- : \quad \frac{G_F^2 s}{4\pi}\left[\frac{1}{3}(1 + 2\sin^2\theta_W)^2 + 4\sin^4\theta_W\right] \simeq 39 \text{ s/MeV}^2 \cdot 10^{-46} \text{ cm}^2 \tag{1.49}$$

$$\nu_{\mu,\tau} + e^- : \quad \frac{G_F^2 s}{4\pi}\left[(1 - 2\sin^2\theta_W)^2 + \frac{4}{3}\sin^4\theta_W\right] \simeq 15 \text{ s/MeV}^2 \cdot 10^{-46} \text{ cm}^2 \tag{1.50}$$

$$\bar{\nu}_{\mu,\tau} + e^- : \quad \frac{G_F^2 s}{4\pi}\left[\frac{1}{3}(1 - 2\sin^2\theta_W)^2 + 4\sin^4\theta_W\right] \simeq 13 \text{ s/MeV}^2 \cdot 10^{-46} \text{ cm}^2 \tag{1.51}$$

The differential cross-section for elastic neutrino-electron scattering, after a detailed calculation, is given by [14]:

$$\frac{\mathrm{d}\sigma}{\mathrm{d}Q^2} = \frac{G_F^2}{\pi}\left[g_1^2 + g_2^2\left(1 - \frac{Q^2}{2p_{\nu_i}\cdot p_{e_i}}\right)^2 - g_1 g_2 m_e^2 \frac{Q^2}{2(p_{\nu_i}\cdot p_{e_i})^2}\right] \tag{1.52}$$

The constants g_1 and g_2 carry information about the neutrino flavour. For electron neutrinos and antineutrinos, their values are:

$$g_1^{(\nu_e)} = g_2^{(\bar{\nu}_e)} = 1 + \frac{g_V^\ell + g_A^\ell}{2} = 1 + g_L^\ell = \frac{1}{2} + \sin^2\theta_W \simeq 0.73 \tag{1.53}$$

$$g_2^{(\nu_e)} = g_1^{(\bar{\nu}_e)} = \frac{g_V^\ell - g_A^\ell}{2} = g_R^\ell = \sin^2\theta_W \simeq 0.23 \tag{1.54}$$

For muon and tau neutrinos (and their antiparticles), one instead has:

$$g_1^{(\nu_{\mu,\tau})} = g_2^{(\bar{\nu}_{\mu,\tau})} = \frac{g_V^\ell + g_A^\ell}{2} = g_L^\ell = -\frac{1}{2} + \sin^2\theta_W \simeq -0.27 \tag{1.55}$$

$$g_2^{(\nu_{\mu,\tau})} = g_1^{(\bar{\nu}_{\mu,\tau})} = \frac{g_V^\ell - g_A^\ell}{2} = g_R^\ell = \sin^2\theta_W \simeq 0.23 \tag{1.56}$$

In the laboratory frame, where the initial electron is at rest ($\boldsymbol{p}_{e_i} = 0$), the momentum transfer squared is simply:

$$Q^2 = 2m_e T_e \tag{1.57}$$

with T_e representing the kinetic energy of the recoiling electron. The differential cross-section as a function of T_e then becomes:

$$\frac{\mathrm{d}\sigma}{\mathrm{d}T_e} = \frac{\sigma_0}{m_e}\left[g_1^2 + g_2^2\left(1 - \frac{T_e}{E_\nu}\right)^2 - g_1 g_2 \frac{m_e T_e}{E_\nu^2}\right] \tag{1.58}$$

where the constant σ_0 is defined as:

$$\sigma_0 = \frac{2G_F^2 m_e^2}{\pi} \simeq 88.06 \cdot 10^{-46}\ \mathrm{cm}^2 \tag{1.59}$$

From energy and momentum conservation, the electron kinetic energy as a function of the scattering angle θ is given by:

$$T_e = \frac{2m_e E_\nu^2 \cos^2\theta}{(m_e + E_\nu)^2 - E_\nu^2\cos^2\theta} \equiv T \tag{1.60}$$

Since $\cos\theta \leq 1$, this implies an upper limit to the kinetic energy, which occurs for forward scattering ($\cos\theta = 1$):

$$T_e^{\max}(E_\nu) = \frac{2E_\nu^2}{m_e + 2E_\nu} \equiv T_{\max} \tag{1.61}$$

Conversely, for a given kinetic energy T, the minimum neutrino energy required is:

$$E_\nu^{\min}(T) = \frac{1}{2}T\left(1 + \sqrt{1 + \frac{2m_e}{T}}\right) = \frac{T + |\boldsymbol{p}_e|}{2} \simeq \begin{cases} \sqrt{\frac{m_e T}{2}} & \text{for } T \ll m_e \\ T + \frac{m_e}{2} & \text{for } T \gg m_e \end{cases} \tag{1.62}$$

In practice, a minimum threshold energy T_{th} for the electron is required to discriminate signal from background. As a result, experiments measure an integrated cross-section above this threshold:

$$\begin{aligned}\sigma(E_\nu, T_{\text{th}}) = \frac{\sigma_0}{m_e}\Bigg[&(g_1^2 + g_2^2)(T_{\max} - T_{\text{th}}) \\ &- \left(g_2^2 + g_1 g_2 \frac{m_e}{2E_\nu}\right)\left(\frac{T_{\max}^2 - T_{\text{th}}^2}{E_\nu}\right) \\ &+ \frac{1}{3}g_2^2\left(\frac{T_{\max}^3 - T_{\text{th}}^3}{E_\nu^2}\right)\Bigg]\end{aligned} \tag{1.63}$$

Differentiating Eq. 1.60, one finds the angular differential cross-section in the lab frame:

$$\mathrm{d}T_e = \frac{4m_e E_\nu^2 (m_e + E_\nu)^2 \cos\theta}{\left[(m_e + E_\nu)^2 - E_\nu^2\cos^2\theta\right]^2}\mathrm{d}\cos\theta \tag{1.64}$$

This leads to the angular differential cross-section:

$$\frac{\mathrm{d}\sigma}{\mathrm{d}\cos\theta} = \sigma_0 \frac{4E_\nu^2(m_e+E_\nu)^2\cos\theta}{[(m_e+E_\nu)^2 - E_\nu^2\cos^2\theta]^2}\left[g_1^2 + g_2^2\left(1 - \frac{2m_eE_\nu\cos^2\theta}{(m_e+E_\nu)^2 - E_\nu^2\cos^2\theta}\right)^2 - g_1g_2\frac{2m_e^2\cos^2\theta}{(m_e+E_\nu)^2 - E_\nu^2\cos^2\theta}\right] \tag{1.65}$$

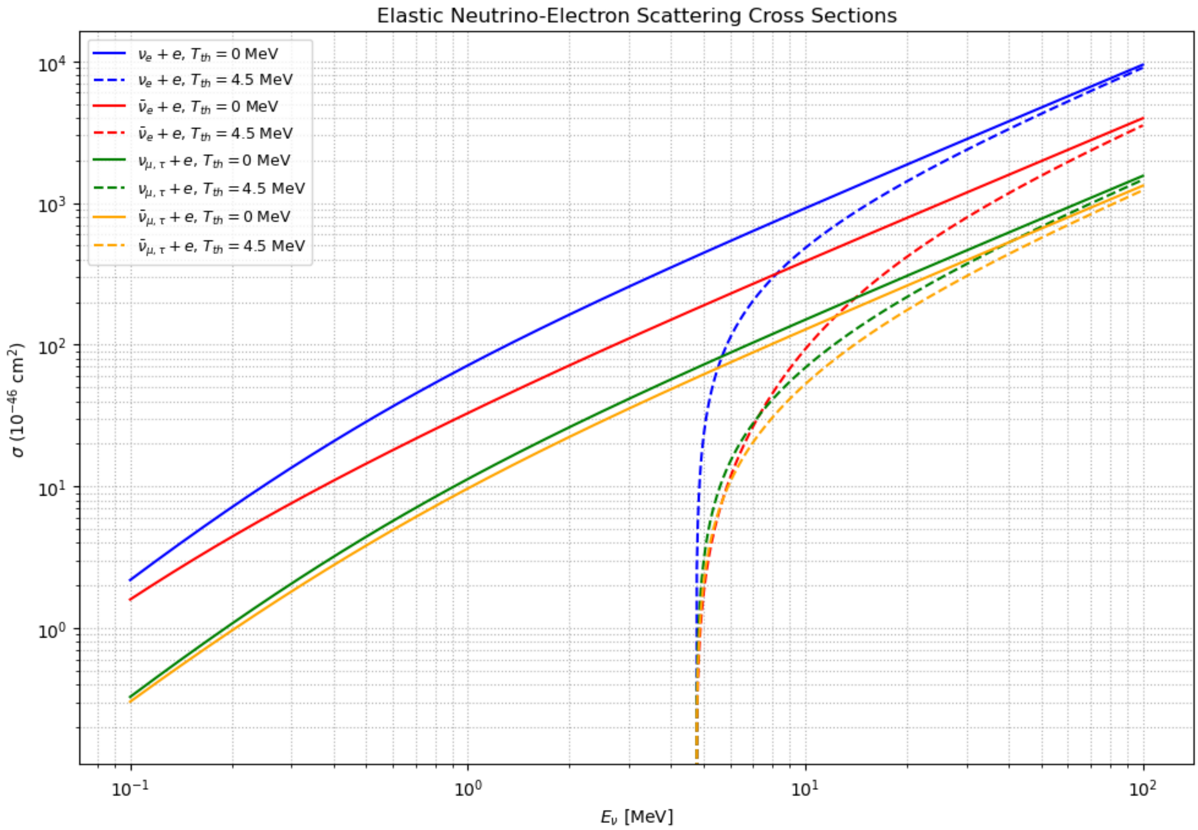

Figure 1.4: Neutrino-electron elastic scattering cross-sections as functions of the neutrino energy. The solid curves represent the cross-sections with no kinetic energy threshold, while the dotted curves reflect the Super-Kamiokande detection threshold, $T_{\mathrm{th}} = 4.5$ MeV [15], corresponding to $E_\nu^{\mathrm{th}} = 4.74$ MeV.

1.3.1.2 Neutrino-Electron Quasielastic Scattering

When a muon neutrino propagates through a medium and its energy exceeds the muon production threshold, it may undergo a process known as *inverse muon decay*:

$$\nu_\mu + e^- \to \nu_e + \mu^- \tag{1.66}$$

This is a quasielastic interaction mediated by the charged current.

In general, for reactions involving multiple particles in the final state,

$$\nu + A \to \sum_X X \tag{1.67}$$

with a stationary target A, and neglecting the neutrino mass, the threshold condition is obtained by requiring that the squared center-of-mass energy exceeds the squared sum of the masses of the final-state particles:

$$s = 2E_\nu m_A + m_A^2 > \left(\sum_X m_X\right)^2 \equiv M^2 \tag{1.68}$$

This leads to the following expression for the energy threshold:

$$E_\nu^{\text{th}} = \frac{M^2}{2m_A} - \frac{m_A}{2} \tag{1.69}$$

For the inverse muon decay in Eq. 1.66, this corresponds to a threshold of $T^{\text{th}} = 10.92$ GeV. The low-energy effective Lagrangian describing inverse muon decay takes the form:

$$\mathcal{L}_{\text{eff}}(\nu_\mu + e^- \to \mu^- + \nu_e) = -\frac{G_F}{\sqrt{2}} \left[\bar{\mu}\gamma^\rho(1-\gamma^5)\nu_\mu\right] \left[\bar{\nu}_e\gamma_\rho(1-\gamma^5)e\right] \tag{1.70}$$

At leading order, the differential cross-section with respect to the scattering angle is given by:

$$\frac{\mathrm{d}\sigma}{\mathrm{d}\cos\theta} = \frac{G_F^2 s}{2\pi}\left(1 - \frac{m_\mu^2}{s}\right) \tag{1.71}$$

However, at the energies relevant for this process, the contribution from the W boson propagator becomes significant. To account for this, one must introduce a factor of $m_W^2/(q^2 - m_W^2)$ into Eq. 1.71. Incorporating this correction, the total cross-section becomes:

$$\sigma = \frac{G_F^2 s}{\pi}\left(1 - \frac{m_\mu^2}{s}\right) \tag{1.72}$$

1.3.2 Neutrino-Nucleon Interactions

Neutrino-electron scattering can occur at all energy scales, even without an energy threshold, and is relatively straightforward to describe from a theoretical standpoint. In contrast, neutrino-nucleon interactions are significantly more complex to model. The large variety of possible final states poses a challenge for theoretical treatment. For this reason, the following discussion will concentrate on the intermediate energy regime, from 0.1 GeV to 20 GeV, which is particularly relevant for the upcoming generation of oscillation experiments.

Within this energy window, several distinct neutrino interaction mechanisms contribute to the total cross-section. These can be broadly categorized into three main processes [13]:

- **Elastic and quasielastic scattering**: the neutrino scatters off a nucleon, resulting in the emission of one or more nucleons.
- **Resonance production**: the neutrino excites the target nucleon into a baryon resonance, such as a Δ or N^*, which subsequently decays into mesons and nucleons.
- **Deep inelastic scattering (DIS)**: at sufficiently high energies, the neutrino probes the quark substructure of the nucleon, giving rise to hadronic showers.

This energy range is often referred to as the *transition region*, as it bridges the domain of quasielastic interactions, where the neutrino interacts with whole nucleons, and deep inelastic scattering, where the neutrino resolves individual partons within the nucleon. Although theoretical models exist for quasielastic, resonance, and deep inelastic scattering individually, a unified framework that smoothly connects these regimes has yet to be developed. Consequently, experimental data play a crucial role in constructing and validating empirical or semi-empirical models of neutrino interactions.

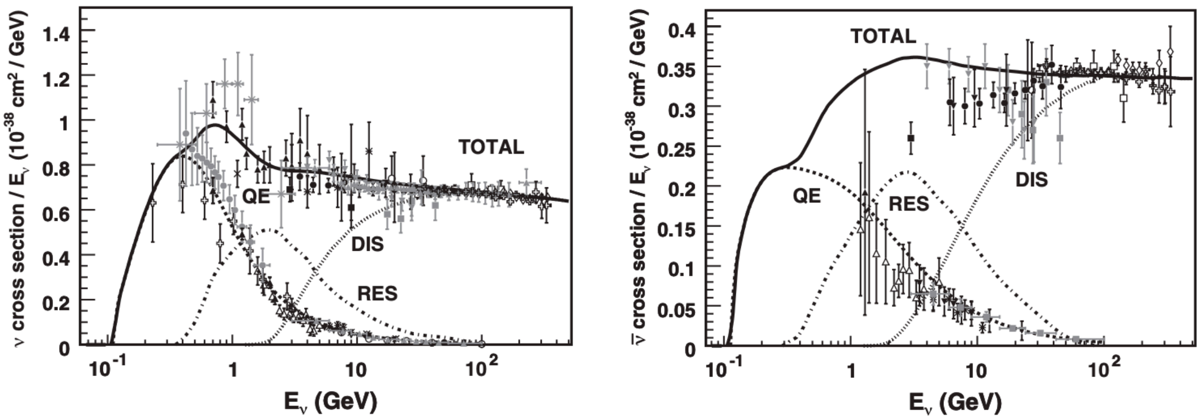

(a) Total neutrino CC cross-section per nucleon.

(b) Total antineutrino CC cross-section per nucleon.

Figure 1.5: Total charged current cross-sections for neutrinos and antineutrinos, normalized per nucleon and divided by the neutrino energy, plotted as a function of energy. Data points correspond to various experimental datasets. The dashed line shows the quasielastic contribution, the dot-dashed line represents resonance production, and the dotted line illustrates the deep inelastic component. Figure taken from [13].

Figure 1.5 displays the charged current cross-section measurements for both neutrinos and antineutrinos in the intermediate energy region. These measurements are based on the following typical reactions[8]:

$$\nu_\mu + N \rightarrow \mu^- + X \tag{1.73}$$

$$\bar{\nu}_\mu + N \rightarrow \mu^+ + X \tag{1.74}$$

A careful examination reveals that the total cross-sections tend to scale linearly with neutrino energy at higher energies. This behaviour is consistent with predictions from the quark-parton model [16]. On the other hand, cross-sections at lower energies are typically less well measured, owing both to historical limitations in data collection and to the experimental difficulties associated with disentangling the complex underlying processes. Moreover, antineutrino cross-sections are generally measured with less precision due to reduced statistics and increased background contamination.

1.3.2.1 Quasielastic Scattering

For neutrino energy less than 2 GeV, neutrino-hadron interaction are predominantly quasielastic (QE), thus they provide a large source of signal events in many neutrino oscillation experiments that operate in this energy regime. In a quasielastic interaction the neutrino scatters off an entire nucleon [13]. In a charged current neutrino QE interaction, the target neutron is converted to a proton; on the contrary, in the case of antineutrino scattering, the target proton is converted into a neutron,

$$\nu_\mu + n \rightarrow \mu^- + p \tag{1.75}$$

$$\bar{\nu}_\mu + p \rightarrow \mu^+ + n \tag{1.76}$$

The differential quasi-elastic cross-section off free nucleons can be expressed as [17]:

$$\frac{\mathrm{d}\sigma}{\mathrm{d}Q^2} = \frac{G_F^2 M^2}{8\pi E_\nu^2}\left[A \pm \frac{s-u}{M^2}B + \frac{(s-u)^2}{M^4}C\right] \tag{1.77}$$

where the $\pm$ sign discriminate neutrino from antineutrino scattering. Moreover, M is the nucleon mass, $s - u = 4ME_\nu - Q^2 - m^2$, E_ν is the incident neutrino energy, m the lepton mass, and Q^2 is the squared four-momentum transfer. The factors A, B and C are function of the vector (F_1, F_2), axial-vector (F_A) and pseudoscalar (F_P) form factors of the nucleon.

Historically, neutrino quasi-elastic scattering on deuterium was used to measure the axial-vector form factor of the nucleon, assuming the conserved vector current (CVC) hy-

[8] As will be discussed in Sec. 2.1, accelerator-based neutrino beams are predominantly composed of ν_μ, and thus the final-state lepton is generally a muon.

pothesis and neglecting the pseudoscalar contribution. The axial form factor is commonly parametrized with a dipole form:

$$F_A(Q^2) = \frac{g_A}{\left(1 + \frac{Q^2}{M_A^2}\right)^2} \tag{1.78}$$

where $g_A = 1.2694$ is precisely known from beta decay, and M_A (the axial mass) is extracted from fits to neutrino scattering data. Early experiments on deuterium found $M_A \sim 1.0$ GeV.

Recent high-statistics experiments have reported axial mass values higher than previous measurements ($M_A \sim 1.05 - 1.35$ GeV), especially on nuclear targets like carbon. This has raised questions, as larger M_A implies larger predicted cross-sections. Discrepancies of up to 30% have been observed between different experiments, such as MiniBooNE and NOMAD. Double differential cross-section measurements, such as those from MiniBooNE, are proving more reliable than extracted M_A values and are used to test and refine nuclear models.

Furthermore, antineutrino QE scattering remains less well studied, especially below 1 GeV. Precise measurements for both neutrino and antineutrino QE cross-sections are crucial for future CP violation studies. Hyperon production via antineutrino interactions is also possible but has only been measured with limited statistics. To date, all QE cross-section measurements at these energies have involved muon (anti)neutrinos. Direct measurements involving electron (anti)neutrinos are still lacking.

1.3.2.2 Neutral Current Elastic Scattering

Neutrino can also elastic scatter from nucleon via neutral-current interactions [13]:

$$\nu_\ell + p \to \nu_\ell + p \qquad \bar{\nu}_\ell + p \to \bar{\nu}_\ell + p \tag{1.79}$$

$$\nu_\ell + n \to \nu_\ell + n \qquad \bar{\nu}_\ell + p \to \bar{\nu}_\ell + p \tag{1.80}$$

Eqn 1.77 still applies in describing NC elastic scattering with the exception that the form factors include additional coupling factor to strange quarks. The strange axial-vector form factor, assuming a dipole form, is equal to

$$F_A^s(Q^2) = \frac{\Delta s}{\left(1 + \frac{Q^2}{M_A^2}\right)^2} \tag{1.81}$$

where Δs is the strange quark contribution to the nucleon spin and M_A is the same axial mass of the last section.

1.3.2.3 Resonant Single Pion Production

Up to this point, the focus has been on elastic and quasielastic interactions. However, when neutrinos carry sufficient energy, they can initiate inelastic scattering processes by exciting a target nucleon into a higher energy state. This leads to the formation of a baryonic resonance (N^*), which typically decays almost immediately into a nucleon and a single pion [13].

$$\nu_\mu + N \to \mu^- + N^* \Longrightarrow N^* \to \pi + N' \tag{1.82}$$

where $N, N' = p, n$. For scattering on free nucleons, there are seven possible single-pion production channels each for neutrinos and antineutrinos. Among these, three are charged current processes:

$$\nu_\mu\, p \to \mu^-\, p\,\pi^+ \qquad \bar{\nu}_\mu\, p \to \mu^+\, p\,\pi^- \tag{1.83}$$

$$\nu_\mu\, n \to \mu^-\, p\,\pi^0 \qquad \bar{\nu}_\mu\, p \to \mu^+\, p\,\pi^0 \tag{1.84}$$

$$\nu_\mu\, n \to \mu^-\, n\,\pi^+ \qquad \bar{\nu}_\mu\, n \to \mu^+\, n\,\pi^- \tag{1.85}$$

and four neutral current processes:

$$\nu_\mu\, p \to \nu_\mu\, p\,\pi^0 \qquad \bar{\nu}_\mu\, p \to \bar{\nu}_\mu\, p\,\pi^- \tag{1.86}$$

$$\nu_\mu\, p \to \nu_\mu\, n\,\pi^+ \qquad \bar{\nu}_\mu\, p \to \bar{\nu}_\mu\, n\,\pi^+ \tag{1.87}$$

$$\nu_\mu\, n \to \nu_\mu\, n\,\pi^0 \qquad \bar{\nu}_\mu\, n \to \bar{\nu}_\mu\, n\,\pi^0 \tag{1.88}$$

$$\nu_\mu\, n \to \nu_\mu\, p\,\pi^- \qquad \bar{\nu}_\mu\, n \to \bar{\nu}_\mu\, p\,\pi^- \tag{1.89}$$

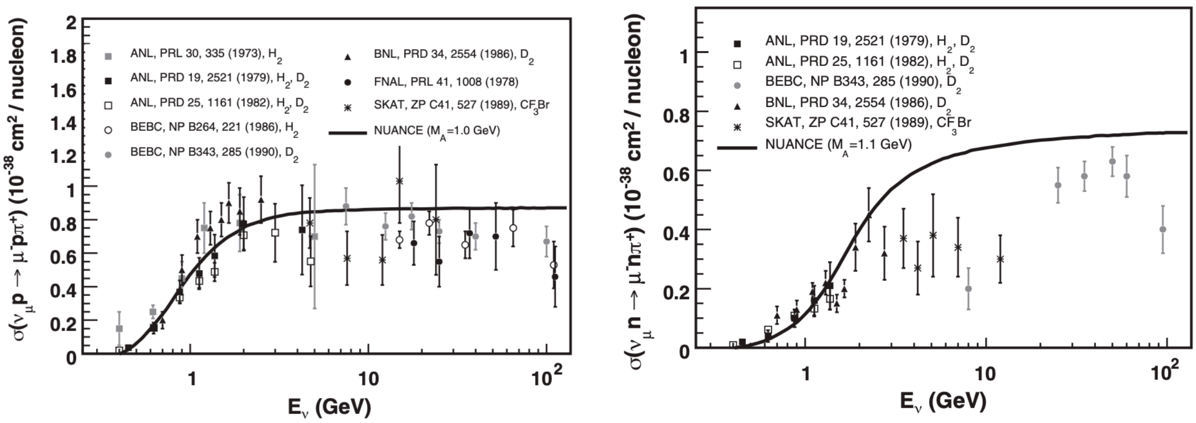

(a) Existing measurements of the cross-section for the CC reaction, $\nu_\mu p \to \mu^- p \pi^+$, as a function of neutrino energy.

(b) Existing measurements of the cross-section for the CC reaction, $\nu_\mu n \to \mu^- n \pi^+$, as a function of neutrino energy.

Figure 1.6: Existing measurements on light target for charged current pion production cross-section. The solid line is the prediction from the nuance neutrino event generator [18], assuming $M_A = 1.1$ GeV. Figures taken from [13].

Figure 1.6 shows historical measurements of single-pion production in charged current interactions. These results, obtained primarily using hydrogen or deuterium targets, provided early validation for cross-section models. In contrast, data on neutral current pion production are significantly more limited and are often expressed as NC/CC ratios.

In recent years, understanding neutrino-induced pion production has gained importance due to its impact on interpreting neutrino oscillation [19]. Both CC and NC processes contribute significantly. For instance, neutral current π^0 production is one of the dominant backgrounds in $\nu_\mu \to \nu_e$ appearance searches. Similarly, CC pion production complicates energy reconstruction in ν_μ and $\bar{\nu}_\mu$ disappearance measurements. Given that modern oscillation experiments often employ heavy targets (see Sec. 2.1), accurately modelling nuclear effects in pion production is crucial. These nuclear effects are complex, not fully understood, and play a non-negligible role. Once produced, a pion must traverse the nucleus to be detected. During this process, it may scatter, be absorbed, or undergo charge exchange, which alters its final state and kinematics.

Modern cross-section experiments (see Sec. 1.4) have increasingly emphasized final-state observables, reporting distributions of directly observed particles. Such measurements are less model-dependent than previous approaches. Recent results, expressed as NC/CC ratios and absolute cross-sections on carbon-based targets, have improved the situation. Still, similar studies on other nuclei, particularly argon and water-which are, respectively, the chosen material for DUNE [20] and Hyper-Kamiokande [21]-are important for the success of future precision experiments.

1.3.2.4 Coherent Pion Production

In addition to resonance-mediated processes, neutrinos can also produce single pions through coherent scattering. In this case, the neutrino interacts coherently with the entire nucleus, transferring very little energy to it. Such low-Q^2 interactions result in no detectable nuclear recoil and produce a pion emitted in the forward direction. Both charged and neutral current (CC and NC) coherent pion production channels are possible [13]:

$$\nu_\mu A \to \nu_\mu \; A\pi^0 \qquad\qquad \bar{\nu}_\mu A \to \bar{\nu}_\mu \; A\pi^0 \tag{1.90}$$

$$\nu_\mu A \to \mu^- A\pi^+ \qquad\qquad \bar{\nu}_\mu A \to \mu^+ A\pi^+ \tag{1.91}$$

Although their cross-sections are smaller compared to those of resonant single-pion production, coherent pion production has been observed across a wide energy range in both NC and CC modes. Figure 1.7 presents a compilation of measured coherent pion production cross-sections on various nuclear targets.

Most of these measurements have been performed at neutrino energies above 2 GeV. At lower energies, however, experiments have generally reported lower coherent production rates than predicted by models that otherwise describe high-energy data well. Theoretical modelling of coherent pion production remains challenging. A widely used approach relates neutrino-induced coherent production to pion-nucleus elastic scattering in the limit $Q^2 = 0$, with a nuclear form factor employed to extrapolate to non-zero Q^2 values [22].

Understanding and modelling coherent pion production is important, as it constitutes another potential source of background in neutrino oscillation experiments.

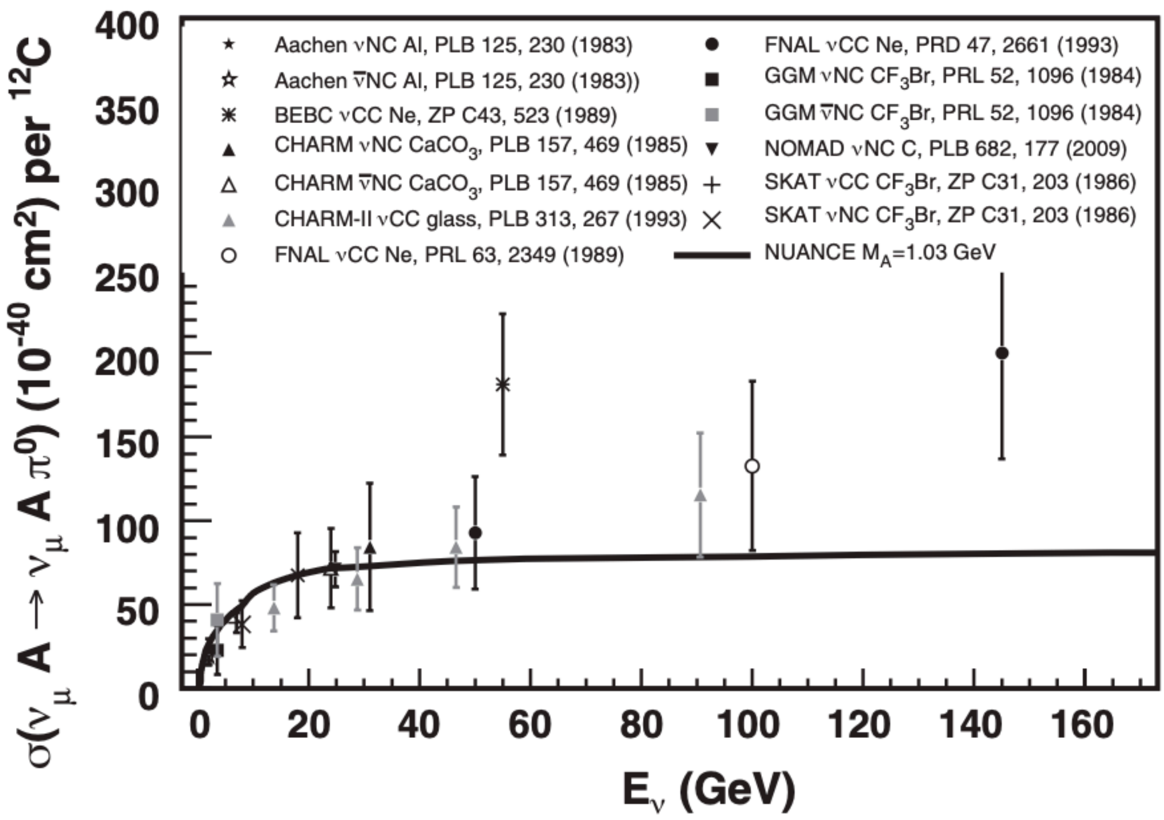

Figure 1.7: Measured absolute cross-sections for coherent pion production on different nuclear targets. Both NC and CC data are shown, with CC results scaled by a factor of 1/2 following the theoretical expectation $\sigma_{NC} = \frac{1}{2}\sigma_{CC}$. Measurements from different target nuclei have been normalized to carbon, assuming an $A^{1/3}$ scaling. Theoretical predictions from the NUANCE event generator [18] are also displayed. Figure taken from [13].

1.3.2.5 Multipion production

Baryonic resonances excited in neutrino–nucleon interactions can decay into final states with multiple pions, although such decays are less probable than their single-pion counterparts. Additional inelastic processes, such as deep inelastic scattering, can also lead to multipion production, depending on the neutrino energy [13].

Figure 1.8 presents available measurements of the di-pion production cross-section in neutrino interactions, focusing on the better-studied channel $\nu_\mu n \to \mu^- p \pi^+ \pi^-$. Due to the inherent difficulty in reconstructing events with multiple pions in the final state, experimental data are scarce. Furthermore, all current results date back to bubble chamber experiments conducted in the 1980s, using deuterium targets.

Enhancing the precision of multipion production measurements is useful for constraining backgrounds in high-energy neutrino oscillation experiments.

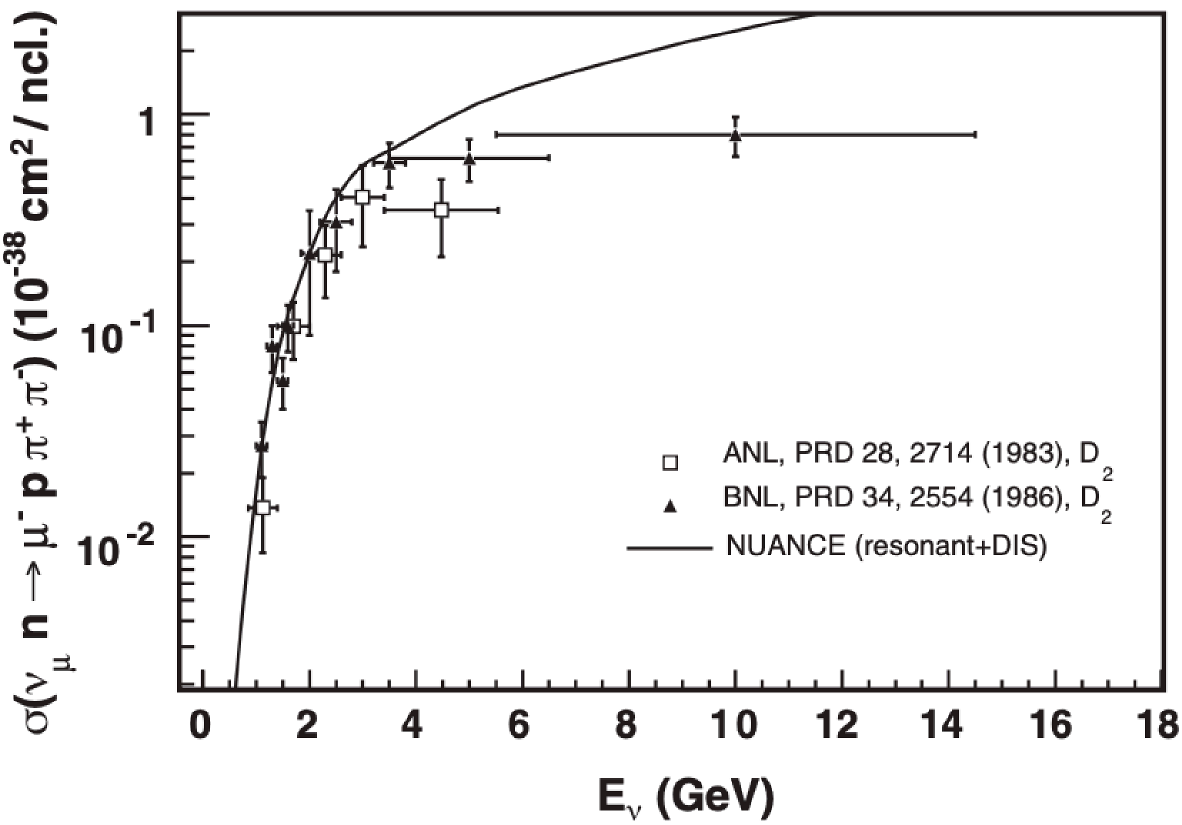

Figure 1.8: Existing measurements of the $\nu_\mu n \to \mu^- p \pi^+ \pi^-$ scattering cross-section. Also shown is the NUANCE prediction, which accounts for both resonant and DIS contributions to the multipion channel. Figure adapted from [13].

1.4 Neutrino Cross-Section Experiments

A precise knowledge of neutrino cross-sections in the GeV energy range is essential to investigate CP violation in the lepton sector [23]. However, the current precision in cross-section measurements is still insufficient for the requirements of modern neutrino oscillation experiments. At present, uncertainties on neutrino cross-sections are typically of the order of $\mathcal{O}(10\%)$ and represent the dominant source of *systematic uncertainty* in oscillation analyses.

1.4.1 Challenges for Precision Oscillation Physics

The discovery of a non-zero value for the θ_{13} mixing angle in 2012 by the Daya Bay experiment [24] marked a turning point in accelerator-based neutrino oscillation physics. This result, together with the approval of large-scale experiments like DUNE and Hyper-Kamiokande (HK), has initiated a new era of precision measurements, driven by unprecedented experimental complexity, significant investments, and long-term planning. Both DUNE and HK aim to study $\nu_\mu \to \nu_e$ oscillations at the GeV energy scale to precisely probe key parameters in the three-flavor framework, such as the CP-violating Dirac phase, the neutrino mass ordering, and the octant of the θ_{23} mixing angle [25].

Over the past five decades, accelerator neutrino beams have achieved increasingly high intensities (> 1 MW of average beam power), at the expense of precision. A major source of uncertainty lies in the determination of the neutrino flux, which directly impacts the precision of cross-section measurements. In conventional beamlines, the ν_μ flux is inferred indirectly from hadroproduction data, i.e., the mesons produced at the target, and detailed simulations of meson transport, interactions, and decays along the beamline.

As discussed in Sec. 1.3, the intermediate energy regime – from a few hundred MeV up to several GeV – is one of the most challenging regions for modeling neutrino-nucleus interactions. This energy window is particularly relevant for DUNE and HK, whose neutrino beams peak at approximately 3 GeV and 0.8 GeV, respectively. Moreover, their detector targets, argon ($Z = 18$) for DUNE and water ($Z = 1, 8$) for HK, highlight the need for accurate modeling of interactions on moderate-Z nuclei [20, 21]. Currently, the precision of cross-section modelling in this regime is limited to $\mathcal{O}(10 - 30\%)$, a level of uncertainty incompatible with the physics goals of DUNE and HK, which require a control of systematic effects at the $\mathcal{O}(1 - 4\%)$ level in the oscillation probability.

While both experiments plan to mitigate some of these uncertainties using the well-established *near-far cancellation technique*, where detector systematics are constrained by comparing neutrino interactions at near and far sites, this method is approaching its intrinsic limitations. In fact, systematic uncertainties are now becoming the dominant factor limiting the sensitivity of next-generation experiments.

To meet the demanding precision physics program of future facilities, the field must rely on new short-baseline experiments dedicated to precision cross-section measurements, up to the percent level. These efforts aim to reduce uncertainties on both inclusive and differential cross-sections, particularly in the energy range relevant for DUNE and HK.

While in the last two decades, the major advances in the neutrino cross-section experiments have been achieved by the previous generation of dedicated experiments (SciBooNE, MINERνA), the near detectors of long-baseline (K2K, MINOS, T2K-ND280, NOνA) and short-baseline experiments (MiniBooNE, MicroBooNE), the physics aim of the next generation of dedicated experiments will be to continue to improve on ν_e, ν_μ and $\bar{\nu}_\mu$ cross-section and to contribute to the short-baseline beyond the SM physics search.

1.4.2 Accelerator-based Neutrino Experiments

In this section, a concise overview of past, ongoing, and upcoming experiments which, in addition to studying neutrino oscillations, have significantly contributed to the measurement of neutrino-nucleus cross-sections is provided [26].

- **K2K** (KEK to Kamioka) was the first long-baseline neutrino oscillation experiment, specifically designed to observe $\nu_\mu \to \nu_\mu$ disappearance [27]. The experiment utilized a neutrino beam with a mean energy of 1.3 GeV directed toward the Super-Kamiokande detector, located 250 km away. The near detector complex included several sub-detectors, such as a 1 kton water Cherenkov detector and a plastic scintillator tracker known as "SciFi", which was later replaced by the extruded plastic scintillator tracker "SciBar". The majority of cross-section data was collected using SciBar, which measured energy deposits near the interaction vertex, the so-called *vertex activity*, to identify coherent scattering events [28].

- **MiniBooNE** (Mini-Booster Neutrino Experiment) operated a mineral-oil Cherenkov detector on the Fermilab Booster neutrino beamline, with $E_\nu \sim 600 - 800$ MeV [29]. Its primary objective was to test the LSND anomaly[9]. Although designed for short-baseline $\nu_\mu \to \nu_e$ appearance searches, the 4π geometry and large fiducial volume of the detector enabled high-statistics neutrino interaction measurements. In the absence of a near detector, MiniBooNE relied on ν_μ interactions to constrain systematics for the ν_e appearance signal and performed the first measurements of flux-integrated differential cross-sections.

- **SciBooNE** (SciBar Booster Neutrino Experiment) reused the SciBar detector from K2K and operated on the same Fermilab Booster beamline as MiniBooNE. It was particularly suited to measure interactions that MiniBooNE could not probe effectively, such as charged-current quasielastic scattering [31] and coherent pion production [32]. Additionally, SciBooNE provided a valuable cross-check of MiniBooNE results. While Cherenkov detectors offer full 4π angular coverage but limited tracking capabilities, tracker detectors like SciBar excel in reconstructing multi-track events, albeit with more limited acceptance.

- **MINOS** (Main Injector Neutrino Oscillation Search) was another long-baseline experiment, following K2K. It aimed to measure both $\nu_\mu \to \nu_\mu$ disappearance and $\nu_\mu \to \nu_e$ appearance signals [33]. MINOS used the on-axis NuMI beam, with adjustable energy spectra based on target and horn configurations; most data were taken in the low-energy mode, peaking at 3 GeV. Both near and far detectors were magnetized iron-scintillator sandwich trackers, allowing for muon momentum reconstruction via curvature and range and enabling charge separation of ν_μ and $\bar{\nu}_\mu$.

- **MINERνA** (Main Injector Experiment for ν-A) was placed upstream of the MINOS near detector and utilized a highly segmented tracker made of extruded plastic scintillator, similar to SciBar [34]. The detector also included passive nuclear targets

[9]The LSND experiment reported an excess of $\bar{\nu}_e$ candidate events potentially compatible with $\bar{\nu}_\mu \to \bar{\nu}_e$ oscillations at Δm^2 values between 0.2 eV^2 and 2 eV^2 [30]

to explore target-dependent cross-section effects. Charge separation was achieved using the downstream MINOS near detector. Data were collected under both low-energy (~ 3 GeV) and medium-energy (~ 7.5 GeV) NuMI configurations.

- **NOMAD** (Neutrino Oscillation MAgnetized Detector) operated at high energy (~ 17 GeV) and focused on $\nu_\mu \to \nu_e$ appearance searches [35]. With excellent control of flux systematics and a finely segmented, magnetized detector, NOMAD provided high-quality data on ν_μ-nucleon interactions, quasielastic scattering, coherent π^0 production, and single-photon events.

- **CHORUS** (CERN Hybrid Oscillation Research Apparatus) and **OPERA** (Oscillation Project with Emulsion-tRacking Apparatus) targeted $\nu_\mu \to \nu_\tau$ appearance. Both employed nuclear emulsions as the active medium in their main tracking systems. Thanks to their unrivaled spatial resolution, emulsions were ideal for identifying ν_τ interactions in OPERA [36] and for studying charged hadron multiplicities in CHORUS [37]. While mainly composed of hydrocarbon (about 60% by mass), emulsions also contain significant fractions of heavier elements like silver and bromine, complicating the interpretation of precision interaction measurements.

- **T2K** (Tokai to Kamioka) is one of the two major long-baseline neutrino oscillation experiments currently in operation. It employs the off-axis neutrino beam from J-PARC, peaking around 600 MeV, and the Super-Kamiokande detector at a distance of 295 km [38]. T2K is designed to measure $\nu_\mu \to \nu_e$ appearance to constrain θ_{13} and δ_{CP}, as well as $\nu_\mu \to \nu_\mu$ disappearance to study θ_{23}. While Super-Kamiokande provides some cross-section data, most measurements come from the near detector complex ND280, which includes the π^0 detector (P0D), fine-grained detectors (FGDs), gaseous argon TPCs, electromagnetic calorimeters (ECal), and the side muon range detector (SMRD). Analyses typically focus on P0D (water target) or FGD (hydrocarbon and water), with additional studies involving argon (TPC) and lead (ECal) targets.

- **NOνA** (NuMI Off-Axis ν_e Appearance) is the other major long-baseline experiment, using the NuMI beam at Fermilab. Although the on-axis beam energy peaks around 7 GeV, NOνA's detectors are placed off-axis to produce a narrow-band beam centered at 2 GeV [39]. This setup enhances sensitivity to $\nu_\mu \to \nu_e$ appearance and $\nu_\mu \to \nu_\mu$ disappearance, and helps constrain δ_{CP}, the neutrino mass ordering, and θ_{23}, complementing T2K's goals. Like MINOS, NOνA features identical near and far detectors. Although the liquid scintillator detector is too coarsely segmented for precise interaction studies, the unique beam configuration enables flux-integrated differential cross-section measurements [40].

Chapter 2

nuSCOPE

The following chapter begins with an overview of accelerator-based neutrino beam technologies and the next-generation long-baseline experiments, namely DUNE and Hyper-Kamiokande. The discussion then shifts to the nuSCOPE project, starting with a brief historical background and the proposed implementations at CERN. It continues with a comprehensive end-to-end description of the beamline instrumentation, and concludes with a dedicated comparison of neutrino detector options, specifically between the DUNE-style liquid argon detector and the Hyper-Kamiokande-style water Cherenkov detector.

2.1 Accelerator Neutrino Beams

Neutrino beams produced at accelerators have played a fundamental role in particle physics, enabling fundamental discoveries such as the identification of distinct neutrino flavours, the study of the weak nuclear force and its unification with electromagnetism, deep inelastic scattering to resolve the quark substructure of nucleons, and the observation of neutrino oscillations, a strong indication that neutrinos have non-zero mass [41].

A conventional neutrino beam is a facility in which a high-energy proton beam impinges on a nuclear target to produce secondary pions and kaons. These secondary mesons, in turn, decay into neutrinos, forming the neutrino beam. Such facilities have operated at all major high-energy laboratories worldwide, including Brookhaven, CERN, Fermilab, J-PARC, KEK, Los Alamos, and Protvino.

2.1.1 Accelerator Beam Concept

The idea of producing neutrino beams at accelerators was independently proposed by M. Schwartz [42] and B. Pontecorvo [6]. The first experimental implementation was carried out in 1962 by L. Lederman, M. Schwartz, and J. Steinberger [7], demonstrating the existence of the muon neutrino (see Sec. 1.1.3). In brief, a proton beam strikes a nuclear target, generating secondary mesons. These secondaries are highly boosted in the forward direction, though they retain a transverse momentum spread due to the production kinematics. The mesons then drift in a decay tunnel, where they decay into tertiary neutrinos. A subsequent shielding system, often called a *beam stopper* or *muon filter*, removes all charged particles, allowing only neutrinos to reach the detector [41].

The primary decay modes of secondary mesons produced in the target are:

$$\pi^{\pm} \rightarrow \mu^{\pm}\nu_{\mu} \qquad (\mathrm{BR} \sim 99.9\%) \tag{2.1}$$

$$K^{\pm} \rightarrow \mu^{\pm}\nu_{\mu} \qquad (\mathrm{BR} \sim 63.4\%) \tag{2.2}$$

$$K_L \rightarrow \pi^{\pm}\mu^{\mp}\nu_{\mu} \qquad (\mathrm{BR} \sim 27.2\%) \tag{2.3}$$

This makes the development of muon neutrino beams the natural choice. Some muons may also decay via $\mu^{\pm} \rightarrow e^{\pm}\nu_e\nu_{\mu}$ within the decay tunnel, leading to a small ν_e contamination. However, due to the long muon lifetime, this process is not an efficient source of electron neutrinos and is instead considered a background. Several proposals, including the original ENUBET design [43], aim to enhance the ν_e component by exploiting the K_{e3} decay:

$$K_L \rightarrow e^{\pm}\pi^{\mp}\nu_e \qquad (\mathrm{BR} \sim 40.5\ \%) \tag{2.4}$$

However, most ν_e beams are instead produced via beam dump experiments. Similarly, ν_{τ} beams are typically generated from $D_s \rightarrow \tau\nu_{\tau}$ decays. The energy spectra of neutrinos in conventional beams can be derived from the spectra of the parent π and K mesons and the kinematics of their decay in flight.

The 1962 neutrino experiment did not employ an extracted proton beam. Instead, protons circulating in the AGS accelerator impinged on an internal beryllium target located in a 3 m straight section of the accelerator. The resulting secondaries, produced at an angle of about 7.5° with respect to the beam axis, contributed to the neutrino flux. A deflector was used to direct the beam onto the target in a burst of duration 25 µs.

The concept of a fast-extracted external proton beam dedicated to neutrino experiments was first proposed at CERN [44]. There were three main motivations for this transition: first, the extraction efficiency onto an internal target was only 50-70%, while fast extraction achieved nearly 100% efficiency; second, the CERN team had developed a magnetic focusing device, a large lens, for capturing forward pions with much greater efficiency than collecting those at 7.5°, which could not fit within the synchrotron infrastructure; and third, this focusing device, the Van der Meer lens, was an electromagnet requiring pulsed operation to avoid overheating.

Short extraction pulses offer a key advantage for accelerator-based neutrino experiments: since the beam is only present for a small fraction of the machine's duty cycle, detectors equipped with sufficiently fast electronics can restrict their data acquisition to a narrow time window synchronized with the beam pulse. This dramatically reduces the background from cosmic-ray muons.

Accelerator neutrino beams can be classified, based on the width of the resulting neutrino energy spectra, into two main categories [45]. The *wide-band beam* configuration is designed to maximize the neutrino flux; this approach has been employed in all major discoveries related to neutrino oscillations, as the high neutrino yield compensates for their low interaction cross-section. However, wide-band beams lack precise control over the momentum and angular distribution of the secondaries within the beamline. Conversely, a *narrow-band beam* configuration provides excellent control over the momentum of the produced secondaries, thereby enabling precise determination of the neutrino energy. This advantage, however, comes at the cost of a significantly reduced neutrino flux.

2.1.2 Wide Band Beams

The focussing of the secondaries from the target is essential to enhance the neutrino flux to the detectors. Taking into consideration pion decay, the flux of neutrinos at a given angle θ with respect to the π direction is:

$$\Phi_\nu = \frac{A}{4\pi z^2}\left(\frac{2\gamma}{1+\gamma^2\theta^2}\right)^2 \tag{2.5}$$

where A is the size of the detector, z its distance from the decay point of the pion and γ is the relativistic boost of the pion [41]. Without focussing, Feynman parton model [46] predicts that pions would diverge from the target with a typical angle,

$$\theta_\pi \approx \frac{\langle p_T \rangle}{p_\pi} \approx \frac{280 \text{ MeV}}{p_\pi} = \frac{2}{\gamma} \tag{2.6}$$

The typical angle of neutrino production from pion decay, which is due to physics of decay and cannot be corrected, is $\sim 1/\gamma$; therefore, at first order, a perfect pion focussing would improve the neutrino flux by a factor of 25.

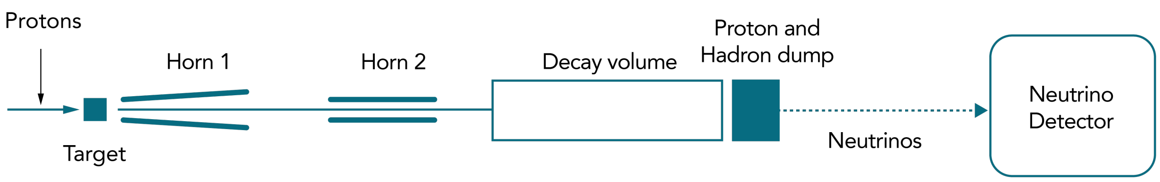

Figure 2.1: Layout of a wide-band beam where the focussing and momentum selection is typically performed by a set of horns. Figure adapted from [45].

2.1.2.1 Horn focusing

S. Van der Meer developed the concept of the *magnetic horn* [47], a focusing device designed to collect secondary π and K mesons produced in the target and direct them towards downstream detectors in order to enhance the neutrino flux.

The magnetic horn consists of two symmetric conductors: a current flows through the inner conductor and returns via the outer one, generating a toroidal magnetic field in the region between them. This field provides a Lorentz focusing force for particles of one charge and a defocusing force for those of opposite charge, thereby enhancing the ν_μ content of the beam while suppressing the antineutrino background (or vice versa).

Such a focusing device is rather uncommon in high-energy physics, as charged particles must physically traverse the conductors, leading to energy loss and multiple scattering. Furthermore, magnetic horns must withstand strong magnetic forces and significant thermal loads due to both the pulsed current and the beam energy deposited in the conductors. Finally, after prolonged operation, magnetic horns become highly radioactive and require remote handling [41].

a. Conical horns Van der Meer's original design featured a conical shape for the inner conductor. In this configuration, the magnetic field varies inversely with the radius:

$$B = \frac{\mu_0 I}{2\pi r} \tag{2.7}$$

As a result, the angular deflection of the pion, that is, the transverse momentum (p_T) kick, in the *thin-lens approximation* is given by:

$$\Delta\theta = \frac{Bx}{p} = \frac{\mu_0 I}{2\pi r}\frac{x}{p} \tag{2.8}$$

where I is the horn current, p is the pion momentum, and x is the path length of the pion within the magnetic field region. Since the incident pion angle and momentum are inversely proportional (see Eq. 2.6), the average incident angle of pions entering the horn is $\langle\theta_i\rangle \approx \langle p_T\rangle / p$. A pion is optimally focused when its final angle $\theta_f = 0$, meaning the transverse kick cancels its incident angle. The focusing condition is therefore:

$$\Delta\theta = \langle\theta_i\rangle \implies \frac{\mu_0 I}{2\pi r}\frac{x}{p} = \frac{\langle p_T\rangle}{p} \implies x = \langle p_T\rangle \frac{2\pi}{\mu_0 I} r \tag{2.9}$$

This implies that the path length x increases linearly with the radial entry point r of the pion into the horn[1]. Notably, the dependence on pion momentum p cancels out, indicating that the device produces a broad-band beam.

b. Parabolic horns The first evolution of the magnetic horn was the *parabolic horn*, whose inner conductor has a parabolic profile. This configuration allows focusing of

[1]Equation 2.9 is derived under the assumptions of a large source distance compared to the horn size ($\ell \gg x$) and the small-angle approximation for θ_i. These approximations do not hold for many modern horn configurations.

particles with a given momentum independently of their entry angle into the horn. The shape of the inner conductor follows the curve $z = ar^2$, where the parabolic parameter a is expressed in cm^{-1}.

The transverse momentum kick provided by the horn produces an angular deflection described by Eq. 2.8, with the path length in this case given by $x = 2ar^2$. A point source located upstream at a distance $\ell = f$, equal to the focal length, is focused if

$$f = \frac{\pi}{\mu_0 a I} p \tag{2.10}$$

There are two main differences compared to the conical horn:

- the parabolic horn focuses particles of a given momentum p for all entry angles (under the small-angle approximation), not only the average one;
- a single parabolic horn provides *monochromatic focusing*, in contrast to the broad momentum acceptance of a conical horn.

2.1.2.2 Multi-horn Systems

The use of multiple focusing elements can significantly improve the neutrino flux, as each subsequent horn can refocus pion trajectories that were not properly aligned by the previous one [41].

A single horn provides a specific transverse momentum kick $\Delta\theta$, which depends on the horn geometry, current, and particle momentum. The horn is typically optimized to deliver a kick that matches the most probable entrance angle $\langle\theta_i\rangle = \langle p_T\rangle / p$, where $\langle p_T\rangle$ is the average transverse momentum of pions exiting the target. However, many particles deviate from this average p_T, entering the horn at a variety of angles. As a result, their outgoing angle will be $\theta_f = |\theta_i - \Delta\theta|$.

A particle entering with $\theta_i = \langle\theta_i\rangle$ will be perfectly focused. On the other hand, particles with entrance angles $\theta_i = 0$ or $\theta_i = 2\langle\theta_i\rangle$ will both emerge with $\theta_f = \langle\theta_i\rangle$.

A second horn, placed downstream of the first, can further reduce the angular divergence of the beam. It sees the particles as coming from a virtual point source with angular spread from 0 to $\langle\theta_i\rangle$, and can reduce this spread by a factor of 2. To avoid perturbing already well-focused particles, its aperture must be wider. A third horn, placed even farther downstream, could reduce the divergence by an additional factor of 2, for a total reduction by a factor of 8, provided the point-source approximation still holds.

Most modern neutrino beams for the study of neutrino oscillations, including T2K, NOνA, DUNE, and Hyper-Kamiokande, exploit two- or three-horn configurations.

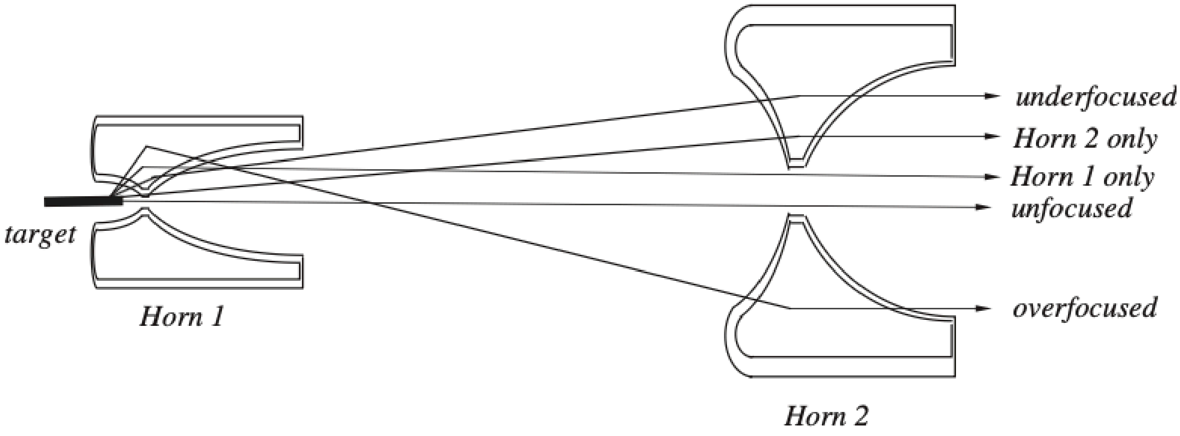

Figure 2.2: Two-lens focusing system: a second lens, placed farther from the target than the first, improves the collection efficiency for particles over- and under-focused by the first horn. Figure adapted from [41].

2.1.2.3 Quadrupole-focused Beams

Quadrupole-based focusing systems are generally less efficient than magnetic horns in terms of neutrino flux, but they offer notable advantages in cost and design simplicity. This is largely because quadrupole magnets are standard components in accelerator infrastructures and do not require pulsing, making them suitable for slow-extraction (slow-spill) beams [41].

A single quadrupole magnet focuses particles in one transverse plane while simultaneously defocusing them in the orthogonal plane. Consequently, two quadrupoles arranged in sequence can produce a net focusing effect in both planes. However, this setup introduces astigmatism, since the focal points in the horizontal and vertical planes do not coincide. This issue can be mitigated by using a triplet configuration, which improves optical focusing across both transverse directions. Although the aperture of a quadrupole is typically much smaller than that of a horn, this is not a major drawback for very high-energy beams. In this regime, the angular spread of secondary particles from the target decreases as $\sim 1/p$ (see Eq. 2.6), making their trajectories more collimated. As a result, high-momentum secondaries are naturally matched to the smaller acceptance of quadrupole systems.

Quadrupole systems focus secondaries with a specific momentum value, and this momentum-selective focusing leads to a distinctive double-peak structure in the resulting neutrino energy spectrum, associated with π and K decays.

Despite providing a perfect focus for particles at the designed momentum $\langle p \rangle$, quadrupole triplets act as wide-band systems if the neutrino detector is positioned relatively close to the beam source. The over- and under-focusing of particles around the design momentum $\langle p \rangle$ contributes to this broad energy acceptance. The geometric interpretation involves an optical source located at a distance u upstream of a lens of diameter $2a$, producing rays that focus at two positions $v_\pm$, defined as:

$$v_\pm = \frac{(D-u)a}{R \pm a} \tag{2.11}$$

with corresponding focal lengths:

$$f_\pm = \frac{1}{\frac{1}{u} \pm \frac{1}{v_\pm}} \tag{2.12}$$

The focal length of a quadrupole triplet can be expressed as:

$$f^* = \frac{6}{k^2L^3} = 6 \times \frac{p^2a^2}{0.09 \times B_0^2L^3} \tag{2.13}$$

where $k = 0.3B_0/(pa)$, p is the secondary momentum in GeV, a is the quadrupole aperture, L is the length of the quadrupole, and B_0 is the field at the pole tip in Tesla. Once the quadrupole is tuned to focus particles with the design momentum $\langle p \rangle$, the source distance u is given by:

$$u = \frac{\langle p \rangle^2 a^2}{6 \times (0.09 \times B_0^2L^3)} \tag{2.14}$$

The boundaries of the momentum acceptance region, $p_\pm$, can be approximated as:

$$\left(\frac{p_\pm}{\langle p \rangle}\right)^2 \approx \frac{\theta_i}{\theta_i \pm \theta_f} \tag{2.15}$$

where $\theta_i = a/u$ is the angular acceptance of the quadrupole, and θ_f is the angular spread needed to illuminate the detector. As the distance between source and detector increases, the accepted momentum range narrows, making quadrupole focusing more suitable for short-baseline applications such as the nuSCOPE experiment.

2.1.3 Narrow Band Beams

In many experimental contexts can be useful to produce fewer neutrinos with more carefully-selected parameters: for example, wide-band beams have large "wrong-sign" content, i.e. $\bar{\nu}_\mu$ in a ν_μ beam and vice versa; or it can be desirable to select neutrinos of a given energy in order to study cross-sections or neutrino oscillations at a particular energy.

2.1.3.1 Dichromatic Beam

The first *dichromatic beam* dates back to the 1970s at Fermilab [48], with a similar configuration soon developed at CERN [49]. This type of beamline employs dipole magnets located downstream of the target to remove "wrong-sign" secondaries and select a narrow band of mesons with a defined momentum. These selected pions and kaons are then transported to a decay tunnel, where their decays generate the tertiary neutrino beam [41].

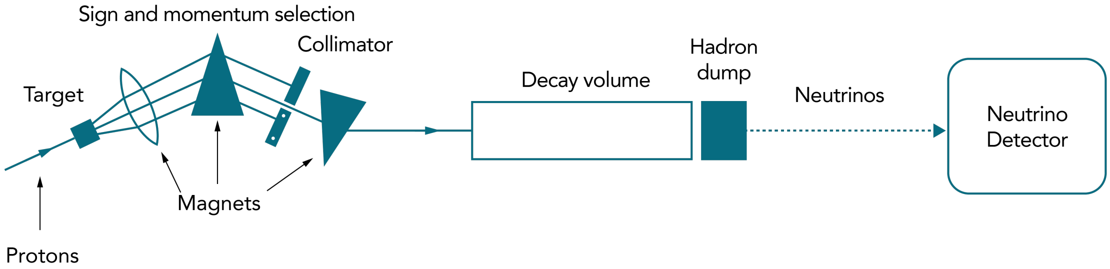

Figure 2.3: A typical layout for a narrow-band beam. After the target, a set of quadrupoles, dipoles, and collimators (slits) selects the sign and momentum and steers the secondaries toward the decay volume. All charged particles but neutrinos are stopped at the hadron dump located before the neutrino detector. Figure adapted from [45].

The term "dichromatic" refers to the fact that the resulting neutrino spectrum features two distinct energy peaks, corresponding to neutrinos from π and K decays. The energy of the neutrino produced in a two-body decay can be expressed as:

$$E_\nu = \frac{1 - \left(\frac{m_\mu}{m_{\pi,K}}\right)^2}{1 + \gamma^2\theta^2} E_{\pi,K} \tag{2.16}$$

where θ is the angle between the neutrino and the meson directions, and $E_{\pi,K}$ is the energy of the parent meson. Even though the secondary beam is selected to have a fixed momentum, the presence of both pions and kaons leads to two distinct neutrino energy peaks. Additionally, meson decays occurring at non-zero angles θ contribute to a smearing of the energy spectrum.

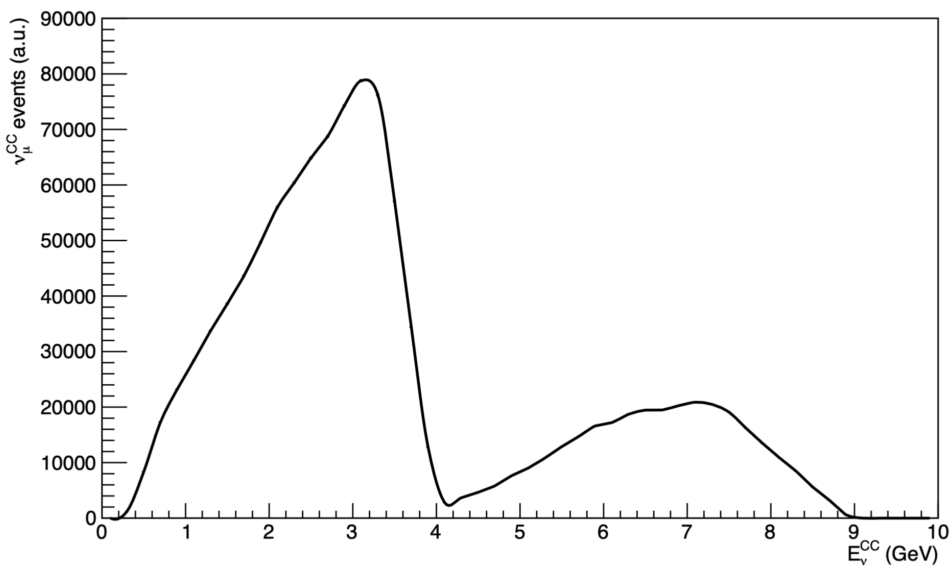

Figure 2.4: Expected spectrum for the NP06/ENUBET monitored neutrino beam. The high-energy peak is associated with ν_μ from kaon decays in the decay tunnel. Figure adapted from [45].

Since meson decays can occur as soon as the secondaries are produced, some neutrinos are emitted upstream of the magnetic selection system. These decays contribute to a "wide-band background" underlying the dichromatic peaks. To reduce this contamination, the primary proton beam is directed onto the target at an angle with respect to the axis of the decay tunnel. This geometry ensures that the neutrinos produced in early decays are predominantly emitted away from the forward beam direction and is also employed in the nuSCOPE beamline.

2.1.3.2 Off-axis Beam

The concept of an off-axis neutrino beam was first introduced by the BNL E889 experiment [50], and is now most notably implemented in the T2K experiment [38]. The estimate of the wide-band neutrino flux (Eq. 2.5) implicitly relies on the linear relationship between the energy of neutrinos emitted along the flight axis and the energy of their parent mesons [41].

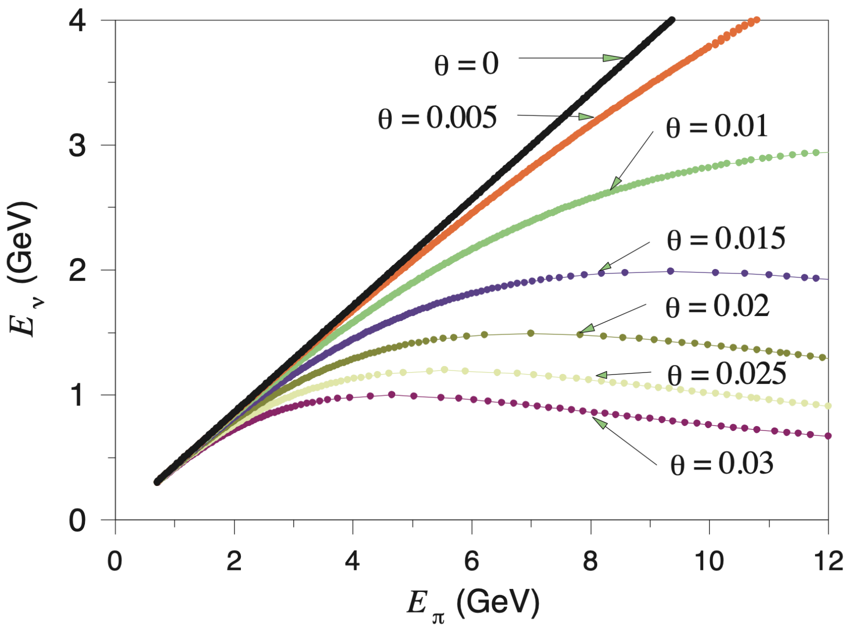

Figure 2.5: Neutrino energy from pion decay as a function of pion energy for different choices of decay angles (in radians). Figure adapted from [51].

In the limit where mesons are perfectly aligned with the decay pipe axis, and under appropriate conditions, mesons of different energies can all contribute to the production of neutrinos with nearly the same energy. This behaviour is illustrated in Fig. 2.5, which shows the correlation between meson and neutrino energies for several off-axis angles. On-axis neutrinos have a linear dependence on the meson energy, while for off-axis configurations, this dependence becomes weaker. Consequently, at sufficiently large off-axis angles, the neutrino energy becomes nearly independent of the pion energy. As a result, a broad-spectrum pion beam can be used to generate a narrow-band neutrino flux.

2.2 Future Long-Baseline Neutrino Experiments

Long-baseline accelerator neutrino experiments produce neutrinos via the in-flight decay of pions and kaons [25]. The distance separating the decay tunnel from the detector is known as the facility's *baseline*.

These experiments operate with baselines ranging from several hundred to thousands of kilometers, constrained only by the Earth's size. This is possible because neutrinos interact extremely weakly and can travel through the Earth with negligible beam loss. However, the neutrino flux at the detector location decreases with distance, following an inverse-square law: it scales as L^{-2}.

The physics reach of long-baseline experiments critically depends on an accurate characterization of the neutrino flux and flavor composition at production, i.e., at the end of the decay tunnel before oscillation effects occur. This information is obtained from a dedicated neutrino detector placed just downstream of the decay tunnel, referred to as the *near detector*. In most cases, the near and far detectors are built using the same detection technologies, so that the associated systematic uncertainties cancel out at leading order.

The discovery of the non-zero value of θ_{13} has sparked an ambitious experimental program that led to the development of two high-sensitivity long-baseline neutrino experiments: Hyper-Kamiokande and DUNE.

2.2.1 The Hyper-Kamiokande Experiment

The T2K facility employs the J-PARC proton accelerator operating at an energy of 30 GeV, supporting a beamline equipped with three magnetic horns. The focused mesons travel and decay within a 96 m-long decay tunnel [38]. Originally designed for a nominal beam power of 750 kW, the facility was later identified as an ideal candidate for a high-statistics experiment aimed at precisely measuring the CP-violating phase δ_{CP} in the leptonic sector. Achieving this goal requires a beam power of 1.3 MW and a far detector larger than Super-Kamiokande (SK) [52]. The Hyper-Kamiokande project responds to this need by constructing a far detector five times larger than SK, fully exploiting the upgraded J-PARC beam. Approved in January 2020, Hyper-K is expected to begin data collection in 2027 [53].

Hyper-Kamiokande follows the same conceptual design as T2K: it will be a water Cherenkov detector with a water mass of 258 kton, housed in a cylindrical stainless steel tank of 68 m diameter and 71 m height. Like SK, the detector is optically divided into an Inner Detector (ID) and an Outer Detector (OD). This separation enables the suppression of backgrounds and provides mechanical support for photomultiplier tubes (PMTs) facing both inward and outward. The OD consists of 8 cm PMTs combined with wavelength-shifting plates, and serves as a cosmic muon veto system. The inner volume is instrumented with approximately 20 000 50 cm PMTs developed by Hamamatsu

Photonics, along with about 800 multi-PMT modules. These PMTs inherit the proven technology developed for SK, but with better quantum efficiency and a dynode structure. Each PMT features a dark noise rate of approximately 4 kHz and an active area of about 2000 cm^2, yielding around 6 photoelectrons/MeV. The multi-PMT modules are composed of 3-inch PMTs arranged at slightly varying angles, improving event reconstruction and the control of detector systematics [54].

The HK detector will be located in the Tochibora mine, about 295 km from the J-PARC accelerator in Tokai, beneath the Nijuugo Mountain near Hida City at a depth of 1750 m.w.e.. It will be positioned 2.5° off-axis from the beam direction to produce a narrow-band neutrino spectrum peaking around 0.6 GeV. At this baseline, matter effects are negligible, simplifying the extraction of CP-violating effects.

Hyper-K is designed to measure CP violation by comparing the $\nu_\mu \to \nu_e$ and $\bar{\nu}_\mu \to \bar{\nu}_e$ oscillation probabilities. Additionally, its large volume and excellent resolution allow for studies of natural neutrino sources. Following the methodology of Super-Kamiokande, HK will also be sensitive to the neutrino mass ordering by measuring the sign of Δm^2_{31}, even without relying on matter effects [55].

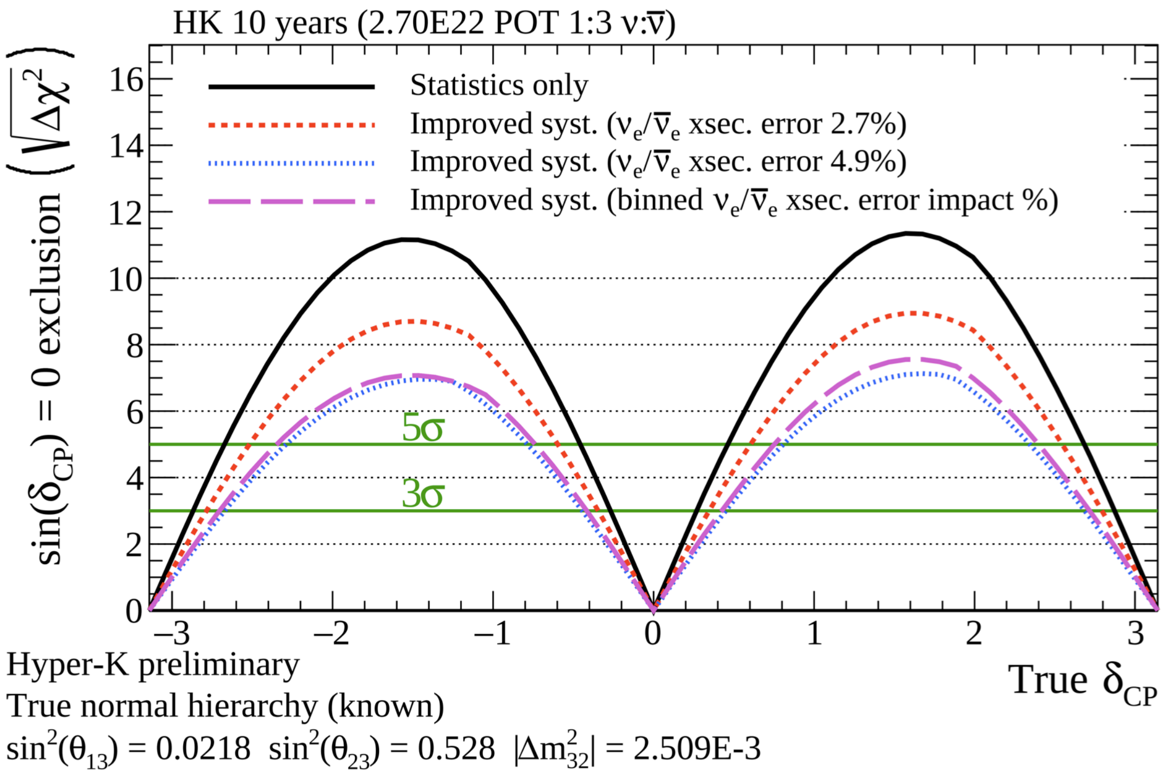

Figure 2.6: Hyper-Kamiokande's projected sensitivity to CP violation over a ten-year period, assuming normal mass ordering. Figure reproduced from [56].

Figure 2.6 shows HK's expected sensitivity to CP violation as a function of the true value of δ_{CP}, with an annual delivery of 2.7×10^{21} protons-on-target (PoT) from J-PARC. Sensitivity to δ_{CP} arises primarily from $\nu_\mu \to \nu_e$ appearance measurements, while precision on $\sin^2\theta_{23}$ and Δm^2_{31} is driven by ν_μ disappearance. Over ten years, HK could exclude CP conservation for about 61% of the possible δ_{CP} values (assuming normal ordering).

Both HK and DUNE will have the capability to determine whether the atmospheric mixing angle θ_{23} is maximal ($\theta_{23} = 45°$) or deviates from it. Determining the so-called octant of θ_{23} has implications for several neutrino flavour models. HK will be able to resolve the octant at 3σ confidence for $\sin^2\theta_{23} < 0.47$ or $\sin^2\theta_{23} > 0.55$.

To complement the near detector system, the HK collaboration is developing an Intermediate Water Cherenkov Detector (IWCD) [54]. The design, inspired by the PRISM concept [57], will also be implemented in DUNE. The IWCD consists of a vertical shaft equipped with PMTs, located 1 km from the neutrino source. The detector module is movable along the shaft to sample off-axis angles between 1° and 4°, allowing it to probe different neutrino energy spectra. This provides a direct, data-driven method to extrapolate the neutrino flux between near and far detectors. Since the near detector cannot be a water Cherenkov detector due to the intense beam, the IWCD helps mitigate systematic mismatches between near and far detector responses [25].

2.2.2 The DUNE Experiment

The design strategy of the Deep Underground Neutrino Experiment (DUNE) [58] differs significantly from that of Hyper-Kamiokande. While water Cherenkov detectors provide clear scalability advantages due to the low cost of the target material, they suffer from limited resolution. In particular, the reconstruction of neutrino interactions is challenged by the presence of final-state particles below Cherenkov threshold and by high-multiplicity events that lead to overlapping Cherenkov rings. DUNE, by contrast, employs a smaller detector volume but utilizes liquid argon time projection chambers (LArTPCs) to achieve high-precision neutrino event reconstruction.

The DUNE project consists of two main facilities designed to support the U.S. program in particle and astroparticle physics over the coming decades [25]. The first facility is a new superbeam, based on the same accelerator infrastructure used for NOνA, but with upgraded performance [20]. Neutrinos are generated via the interaction of primary 120 GeV protons, accelerated by the Fermilab Main Injector, with a solid target. Secondary mesons are focused by three magnetic horns and decay in a 194 m long helium-filled decay pipe. The accelerator is designed to provide a beam power of 1.2 MW, corresponding to about $1.1 \cdot 10^{21}$ PoT/year, for Phase I operations. This wide-band beam, with a spectrum centered around 2.5 GeV, is directed toward two LArTPCs located 1300 km away. Each of the first two modules has a fiducial mass of 17 kton. In Phase II, the beam intensity will be increased to 2.1 MW, and two additional modules will be added, bringing the total mass to 40 kton.

The second facility is an underground laboratory at the Sanford Underground Research Facility (SURF), in Lead, South Dakota, situated in the former Homestake gold mine.

The excavation of the experimental cavern was completed in August 2024, and it will host the four far detector modules.

Thanks to the on-axis wide-band beam and the superior resolution of LArTPCs, DUNE can study neutrino oscillations over a broad energy range. This includes both the first (2.5 GeV) and second (0.6 GeV) oscillation maxima, enabling the reconstruction of the full sinusoidal oscillation pattern. This is essential to remove correlations among oscillation parameters. DUNE will be capable of simultaneously determining the value of the CP-violating phase δ_{CP}, the mass ordering, and the octant of θ_{23}, without relying on external constraints.

The first DUNE TPC module adopts the *Horizontal Drift* configuration, with a drift length of 3.5 m and a cathode operated at -180 kV. Each module includes two cathodes and three anodes. The anode planes are organized into modules called Anode Plane Assemblies (APAs), with typical dimensions of 6×2.3 m^2. These components are assembled on site. The cryogenic system employs a *membrane cryostat*, a corrugated stainless-steel container with both liquid and gaseous argon, surrounded by insulation layers to minimize heat transfer. The readout electronics is placed inside the cold volume to reduce electronic noise. The LArTPC records both the ionization electrons and the prompt 128 nm scintillation light produced by argon de-excitation. DUNE adopts the X-ARAPUCA photon detection system [59], which improves light collection efficiency by shifting the wavelength of UV photons into the visible range, where SiPMs are more efficient, and trapping the light within an enclosed reflective volume covered by SiPMs.

The second far detector module adopts the *Vertical Drift* concept [60], developed to take advantage of recent LArTPC advancements. It features a drift length of 6.5 m with a cathode voltage of -300 kV, allowing electrons to drift vertically toward anodes located at the top and bottom of the cryostat. In this design, the traditional wire-based anode is replaced by silicon strip arrays on PCBs, simplifying construction and reducing cost. Since the strips are opaque to light, X-ARAPUCA modules are installed on the lateral walls of the cryostat and inside the cathode.

The DUNE near detector complex [61] has multiple functions: it monitors the initial neutrino flux and flavor, identifies systematic effects in the near-to-far extrapolation, and helps constrain neutrino cross-sections. The near detector LArTPC, called ND-LAr, shares the detection medium with the far detectors but is adapted for the high event rate near the beam source. ND-LAr has limited acceptance for muons above 0.7 GeV, so a dedicated muon spectrometer is also included. Both ND-LAr and the spectrometer are mounted on an horizontally movable platform in order to implement the PRISM concept to study off-axis neutrino fluxes at different energies.

The final component of the near detector station is the SAND detector (System for on-Axis Neutrino Detection) [61], a magnetized spectrometer that continuously monitors the on-axis beam flux. SAND reuses components from the former KLOE detector, including its superconducting solenoid magnet (providing up to 0.6 T) and high-granularity lead-scintillator sampling calorimeter [62]. The inner tracker consists of straw-tube detectors.

Thanks to the long baseline and wide-band beam, DUNE is expected to determine the sign of Δm^2_{31} (i.e., the neutrino mass ordering) within the first two years of Phase I, which is scheduled to begin data collection in 2030. The full sensitivity to δ_{CP} and the θ_{23} octant will be achieved in Phase II [63].

In addition to its long-baseline program, DUNE's underground location (∼4300 m.w.e.) enables a complementary physics program with natural neutrino sources. Compared to Hyper-Kamiokande, DUNE is more sensitive to proton decay in the $p \to K^+\bar{\nu}$ channel, as kaons are below the Cherenkov threshold in water. Conversely, HK is more competitive in the $p \to e^+\pi^0$ decay channel due to its larger target volume. For a galactic supernova explosion, HK would observe a large number of elastic scattering events on electrons, while DUNE benefits from the larger charged-current cross-section on argon.

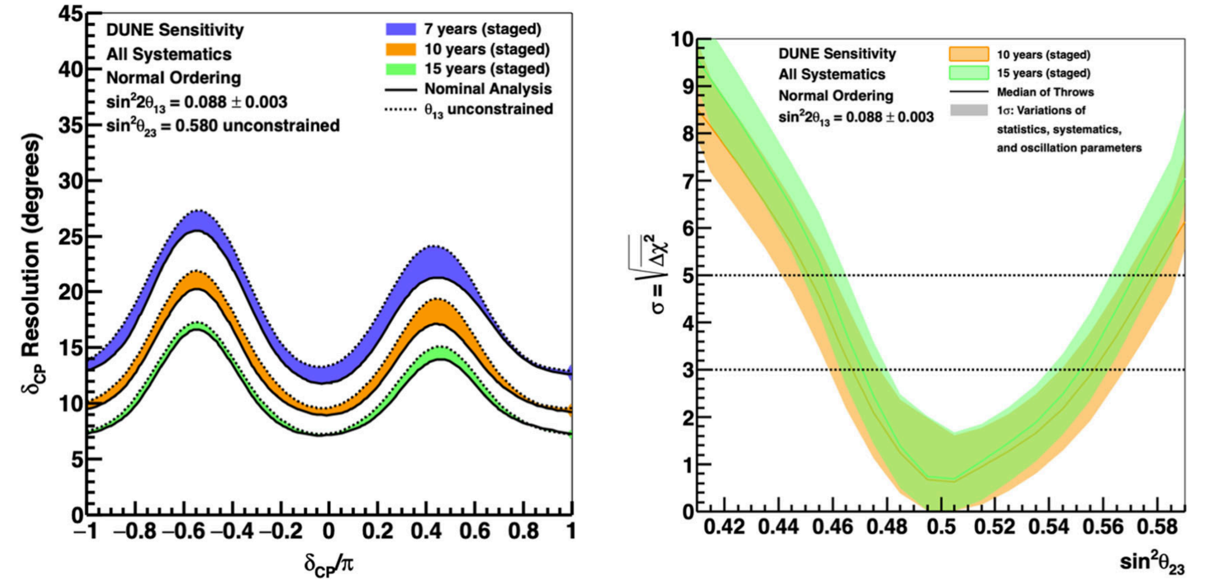

(a) Resolution for the DUNE measurement of δ_{CP} as a function of the true value of δ_{CP} for seven, ten and fifteen years of exposure. The band width shows the impact of applying an external constraint on θ_{13}

(b) Sensitivity to the determination of the θ_{23} octant as a function of the true value of $\sin^2\theta_{23}$ for ten and fifteen years of exposure, assuming normal mass ordering.

Figure 2.7: DUNE sensitivity and resolution to some oscillation parameters, such as (a) the value of δ_{CP} and (b) the octant of θ_{23}. Figures reproduced from [63].

2.3 The nuSCOPE Experiment Proposal

The physics reach of next-generation long-baseline experiments such as Hyper-Kamiokande and DUNE relies heavily on the ability to control systematic uncertainties. Both experiments benefit from unprecedented statistics enabled by intense neutrino beams and massive detectors; however, these advantages can only be fully exploited if systematic effects are kept under tight control. The primary tool to constrain these uncertainties is the near detector, which provides precise measurements of the unoscillated flux, interaction cross-sections, and detector response.

To further mitigate systematics, these experiments implement a comprehensive reduction strategy that includes auxiliary data from hadron production experiments – performed on full-scale replicas of the DUNE and HK targets – and high-precision measurements of neutrino cross-sections from dedicated facilities. It is within this broader experimental program that the **nuSCOPE/ENUBET** project is positioned [23].

2.3.1 Monitored Neutrino Beams

Beam diagnostics play a crucial role in estimating the neutrino flux and characterizing the properties of the beam. Over the years, the power of accelerator-based neutrino beams has increased by several orders of magnitude, pushing diagnostic systems to focus on radiation hardness and rate capabilities, while improvements in precision have been limited [45]. Current diagnostics can determine the neutrino flux with a typical precision of approximately 10%. While sufficient for some applications, this level of uncertainty is inadequate for the next generation of oscillation experiments, which require cross-section measurements at the percent level.

Achieving such precision demands a paradigm shift in the approach to beam monitoring. Instead of relying on indirect estimators, diagnostics must be based on observables directly correlated with the neutrino flux on a particle-by-particle basis [64].

A conceptual breakthrough dates back to the 1970s, when B. Pontecorvo proposed a technique to directly measure the leptons produced in a beam dump experiment [65] and associate them in time with the corresponding neutrino observed in the detector. Since each neutrino produced from a charged meson decay is accompanied by a charged lepton, counting these leptons allows for a direct determination of the neutrino flux, bypassing the exact knowledge of the hadronic production rate. Pontecorvo noted that an even more ambitious facility could be developed in the far future by instrumenting the decay tunnel of a conventional neutrino beam to track the charged leptons and parent pions. Facilities implementing this idea are referred to as *tagged neutrino beams*, which will be addressed in detail in Sec. 2.3.2.

A more readily achievable step toward precision flux determination is the implementation of a *monitored neutrino beam* [43]. This design is based on a conventional beamline, where the cylindrical walls of the decay tunnel are instrumented with cost-effective particle detectors that serve as real-time beam diagnostics.

Figure 2.8 illustrates the layout of the ENUBET monitored neutrino beam. Protons are extracted from the accelerator and transported to a solid target via a transfer line. Upon interacting with the target, they produce a range of secondary hadrons, including short-lived ones like K_S and charmed mesons. These short-lived hadrons can yield neutrinos in the forward direction, often alongside non-interacting primary protons and high-momentum secondaries. However, such particles are typically absorbed in the proton dump, and their associated neutrons have a negligible probability of reaching the off-axis detector. Only secondaries within the beamline's momentum acceptance are collected, sign-selected, and focused by the optics system before entering the decay tunnel. Alongside these desired particles, background components such as tertiary particles ($e^{\pm}$, γ, $\mu^{\pm}$, $\pi^{\pm}$), off-momentum mesons, and halo muons, produced by pion decays in the transfer line, can also enter the tunnel, even if they fall outside the nominal momentum acceptance [64].

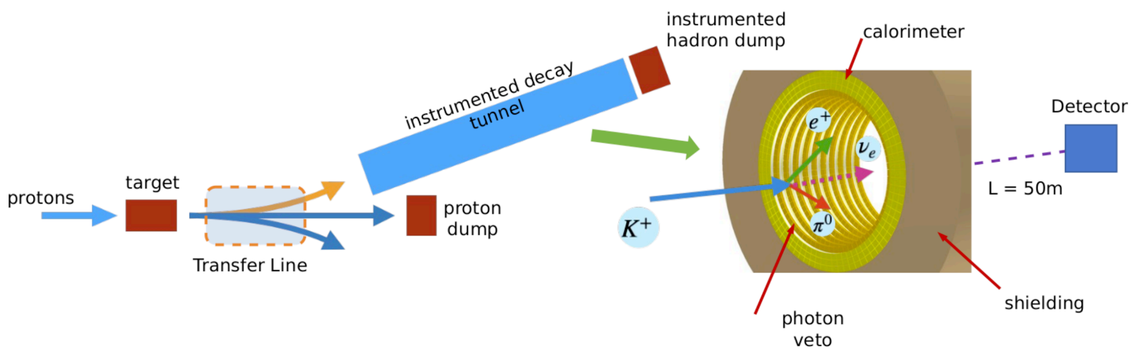

Figure 2.8: Layout of the ENUBET monitored neutrino beam facility. Figure adapted from [43].

The secondaries transported to the tunnel must have a small angular divergence, as the beam envelope must remain within the tunnel's aperture. This design choice is critical because most of the beam instrumentation is placed along the cylindrical tunnel walls.

Unlike tagged neutrino beams, a monitored neutrino beam does not require associating charged leptons to specific neutrino interactions in the neutrino detector. Therefore, the timing resolution of the calorimetric detectors can be relaxed to the nanosecond scale, as it is only necessary to identify coincident hits and suppress pile-up. Event reconstruction in this setup is restricted to the spatial region around the lepton's impact point [64].

Currently, the most advanced implementation of this concept is the NP06/ENUBET project.

2.3.2 Tagged Neutrino Beams

As outlined in the previous section, the concept of neutrino tagging originated in the 1970s and was initially explored in the Soviet Union during the 1980s [66]. However, these early efforts did not succeed in reaching their physics goals due to the overwhelming charged particle rates in the decay tunnel and the limited spatial and temporal resolution of the available tracking technologies. In recent years, the idea has experienced renewed interest, driven by significant advancements in detector capabilities.

The *neutrino tagging* (NuTag) technique [67] aims to complement the information extracted from neutrino interactions by exploiting the kinematics of their production processes [68]. In accelerator-based neutrino beams, muon neutrinos are primarily generated via the experimentally well-understood decays $\pi^{\pm} \to \mu^{\pm}\nu_{\mu}$ ($\bar{\nu}_{\mu}$) and $K^{\pm} \to \mu^{\pm}\nu_{\mu}$ ($\bar{\nu}_{\mu}$). By accurately measuring the momenta and directions of the parent mesons and resulting muons, it becomes possible to reconstruct the kinematics of the produced neutrinos. These are referred to as *tagged neutrinos*. This method allows for an energy resolution better than 1% on the neutrino energy, a substantial improvement over the $10-30\%$ resolution typically achievable with conventional neutrino detectors [67].

Neutrino tagging offers several key advantages:

- **Improved flux determination**: the ability to reconstruct nearly all beam neutrinos originating from pion and kaon decays enables a highly precise determination of the neutrino flux and its composition in energy, flavour, and chirality.

- **Background rejection**: in appearance experiments, a major background is represented by the intrinsic ν_e component of the beam. Since these are not associated with any tagged ν_{μ}, the tagging technique allows for their identification and rejection, leading to improved signal purity.

- **High-resolution energy reconstruction**: the energy of tagged neutrinos is derived from the parent pion momentum, which can be measured with excellent precision using a magnetic spectrometer. For $\pi^{\pm}$ in the $\mathcal{O}(1-10)$ GeV range, resolutions of $\mathcal{O}(0.1-1\%)$ are achievable, with almost no uncertainties on the energy scale. This surpasses the performance of calorimetric or kinematic methods relying solely on neutrino interactions.

- **Improved flavour and interaction channel identification**: since the tagged neutrino energy is independent of the interaction final state, comparing it to the energy deposited in the detector provides insight into the nature of the interaction. For example, this method allows one to distinguish between neutral-current and charged-current interactions, since NC events release less visible energy.

- **Refined modelling of neutrino interactions**: a well-characterized neutrino flux and precise energy reconstruction provide a powerful tool to improve theoretical models used to extract the neutrino energy from observed interactions with nuclei.

- **Event-by-event chirality tagging**: the tagging technique enables the determination of the neutrino chirality for each event. Consequently, the alternation of beam polarity is no longer needed and both ν and $\bar{\nu}$ events can be recorded simultaneously. This effectively doubles the statistics relative to traditional beams.

2.3.3 A Brief History of the Experiment

As discussed in the previous sections, the concept of a tagged neutrino beam was originally proposed in the 1970s [65] and first tested experimentally in the 1980s [66]. However, these early attempts were unsuccessful in achieving their physics goals due to the inadequate tracking capabilities of detectors at the time. For the following three decades, the idea was largely set aside, as the focus of the neutrino physics community shifted towards the experimental discovery of oscillations and the coarse determination of the relevant mixing parameters. This long period of exploratory measurements culminated in 2012 with the discovery of a non-zero value for θ_{13}.

Meanwhile, the steady increase in the intensity of accelerator-based neutrino beams opened the path for a new generation of long-baseline experiments, most notably DUNE and Hyper-Kamiokande, designed to explore the lepton sector of the Standard Model with unprecedented precision. These are the first neutrino oscillation experiments expected to transition from being limited by statistical uncertainties to being dominated by systematics [69].

The dominant source of systematic uncertainties is our incomplete understanding of neutrino cross-sections in the GeV energy range. Current theoretical models and phenomenological approaches fail to reproduce experimental data with better than 10% accuracy, primarily due to nuclear effects in neutrino-nucleon interactions (see Sec. 1.3). Conventional short-baseline experiments (see Sec. 1.4) are unable to determine the neutrino flux at the percent level, an essential requirement to support the physics program of DUNE and HK.

In this context, the original idea of Pontecorvo regained relevance. In 2015, A. Longhin, L. Ludovici, and F. Terranova proposed a new concept: the *monitored neutrino beam*, implemented in the ENUBET project (Enhanced NeUtrino BEams from kaon Tagging) [43].

ENUBET officially began in 2016 as an ERC-funded project. Between 2016 and 2018, the collaboration identified the optimal detector technology for monitoring positrons from kaon decays, which are the main source of ν_e in short-baseline experiments. This instrumentation was validated through prototype testing [70], and a full simulation of the e^+ reconstruction chain, from detector response to particle identification, was successfully developed.

Since March 2019, ENUBET has been part of the CERN Neutrino Platform (as NP06/ENUBET), aimed at developing next-generation neutrino beams and detectors. Between 2019 and 2021, NP06/ENUBET demonstrated that a high-intensity monitored neutrino beam could be operated without the need for a magnetic horn, by using slow proton extraction [64]. This achievement reduced the instantaneous particle rate at the decay tunnel by nearly a factor of 50, and enabled the monitoring of all neutrino flavours by detecting both positrons from kaon decays and muons from pion/kaon decays.

From 2021 to 2023, the ERC project reached its objective and ended in 2022. Meanwhile, the hornless beamline design was refined, including its optics, simulation of tertiary interactions, radiation studies, and flux predictions at the neutrino detector. In November 2021, the first small-scale calorimeter prototype, ENUBINO, was built and tested at CERN to validate the design for a full-scale demonstrator [71]. During 2022–2023, this demonstrator, a 1.65 m long instrumented tunnel section covering 90°, was tested at the T9 beamline at CERN East Area, confirming the scalability, efficiency, and particle identification performance of the proposed technology in a high-flux, irradiated environment [72].

Simultaneously, the use of long proton extraction opened the door to realizing a full *tagged neutrino beam*, as pursued by the NuTag Collaboration since 2022 [67, 68]. The NuTag proposal builds on the development of fast, radiation-hard silicon trackers pioneered by the NA62 Gigatracker [73], and further improved within the LHC upgrade program [74]. These technologies enable tracking of both the parent mesons and their daughter leptons inside the decay tunnel, making true neutrino tagging feasible for the first time. The long-standing technical limitations that plagued this concept since the 1970s have now been overcome, and in February 2025, NA62 reported the first observation of a tagged neutrino candidate, based on data collected in 2022.

In 2023, the ENUBET and NuTag collaborations merged into a new joint effort to assess the feasibility of constructing such a facility at CERN [75]. The design was further refined within the framework of the Physics Beyond Colliders (PBC) study group at CERN, culminating in the optimized beamline concept presented in this thesis, tentatively referred to as SBN@CERN. In May 2025, the collaboration officially adopted the name **nuSCOPE** (Neutrino SPS COmplex for Precision Experiments).

2.3.4 Possible Implementation at CERN

The nuSCOPE beamline can be served, in principle, by different proton drivers around the world, such as the PS and SPS at CERN, Fermilab's Main Injector, or J-PARC beam. However, the choice of the CERN SPS is particularly attractive when the mean secondary momentum corresponds to 8.5 GeV because the number of pions produced per proton hitting the target scales roughly with the energy of the primary protons and the secondary yield at 8.5 GeV is close to maximum [71].

CERN's North Area is usually the prime location for fixed-target experiments at CERN due to the availability of a slow extraction from the SPS at the Long Straight Section 2 (LSS2) and of the existing infrastructure and beamlines [76]. The ideal location in the CERN North Area could be the ECN3 cavern due to its depth and radio-protection limits. However, starting from LHC Run 4 in 2030 [77], the SHiP experiment will occupy that cavern [78].

Due to radiation constraints, the beamline cannot be placed in the surface halls EHN1 and EHN2. Additionally, the beamline's bending angle (see Sec. 2.4) makes its implementation difficult in experimental halls like EHN1 and EHN2, as they are predominantly long rather than wide. A placement beneath EHN1 is also excluded due to the presence of technical galleries below the building and the associated challenges of excavating near the Lion River.

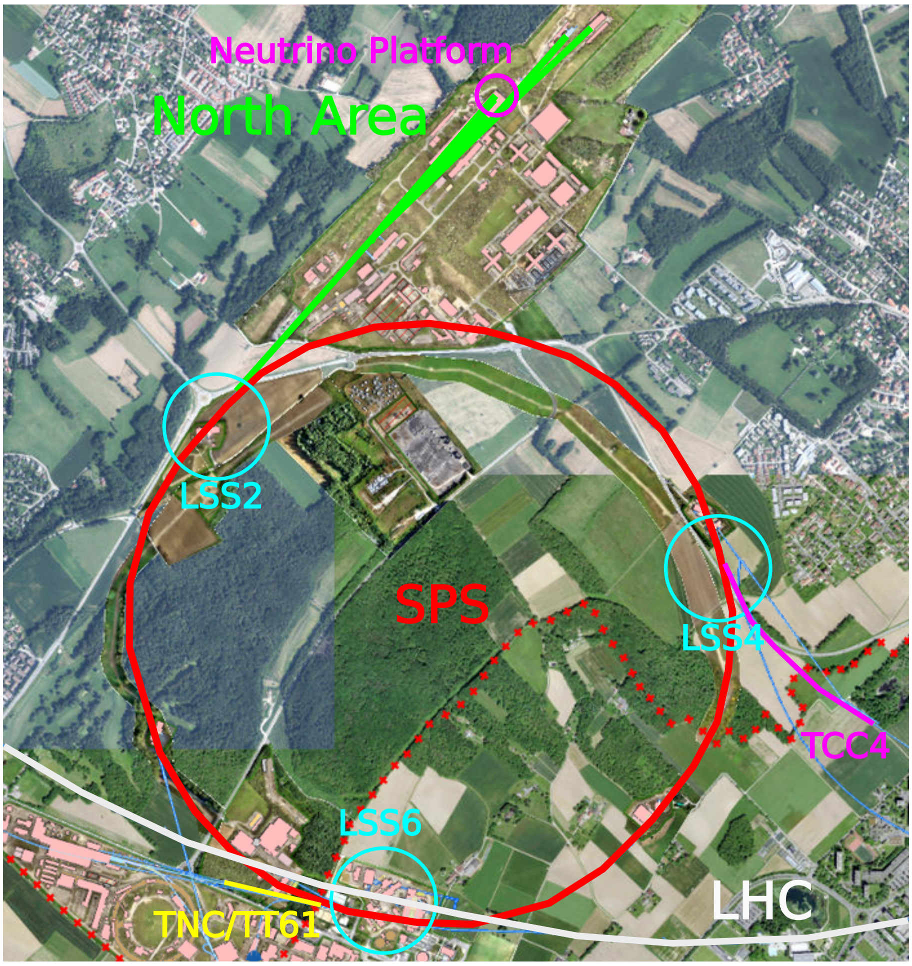

Figure 2.9: Satellite view of the CERN SPS complex. The three experimental areas at the SPS are located at the three Long Straight Sections: LSS2, LSS4, and LSS6. The Neutrino Platform, which houses the ProtoDUNE detectors, is located at the ends of the H2 and H4 beamlines in the North Area. Figure adapted from [76].

2.3.4.1 Implementation at ECN4

The CERN Accelerator and Technology Sector has examined the feasibility of constructing a new underground cavern, ECN4, originally proposed for the BDF/SHiP facility. This site, located on the Jura side of TCC2 (which currently houses the EHN1 beamline targets), is also considered for the nuSCOPE beamline due to similar infrastructure requirements. However, the significantly lower beam intensity required by nuSCOPE, $1 \cdot 10^{13}$ PoT/spill and up to 2-3 $\cdot\, 10^{18}$ PoT/year, compared to $4 \cdot 10^{13}$ PoT/spill and ten times higher annual PoT for BDF/SHiP, implies reduced demands on shielding, cooling, and radiation protection. As a result, nuSCOPE gains greater flexibility in the placement of the experimental area.

Several core components of the ECN4 design remain applicable. The beam extraction could be implemented via a new junction cavern, ideally using a shared SPS cycle, since a dedicated cycle would require extensive R&D and may compete with other experiments. Downstream of the junction cavern, a fully underground transfer tunnel would be excavated, leading to a graphite target and a compact beam dump (e.g., XTAX-type). Due to the lower intensity, a simple target system is sufficient. No auxiliary access building is expected, as the beamline terminates shortly after the decay tunnel. The experimental hall can be placed at surface level, similarly to the EHN1 Neutrino Platform, thanks to the natural upward bending of the beamline. This allows for nearby detector deployment, removing the need for deep underground halls.

2.3.4.2 Implementation at SPS LSS6

In addition to the LSS2-based North Area extraction, the possibility of installing the nuSCOPE facility downstream of LSS4 or LSS6 is also being considered. These locations serve LHC Beam 2 (LSS4) and Beam 1 (LSS6), as well as AWAKE and HiRadMat, respectively. While both LSS4 and LSS6 already host extraction systems, they lack the electrostatic ZS septa needed for a slow extracted beam. Among the two, LSS6 appears more favourable due to its depth and downstream infrastructure.

A conceptual study [79] has proposed a *non-local* slow extraction scheme, where ZS septa are installed in LSS4 or LSS5, upstream of LSS6, enabling beam extraction via orbit bumps without interfering with the fast extraction systems for the LHC. This non-local solution resembles existing schemes in the PS [80] and avoids complex modifications in LSS6. Two drift spaces longer than 20 m have been identified in LSS4 and LSS5 as suitable locations for the five required ZS septa modules. LSS4 is presently the baseline candidate, although LSS5 could be considered pending further feasibility studies. The beam would undergo two orbit bumps and oscillate through the SPS ring until it is extracted by the magnetic septa in LSS6. Importantly, this setup would allow the beamline to be operated without competing for protons with other projects.

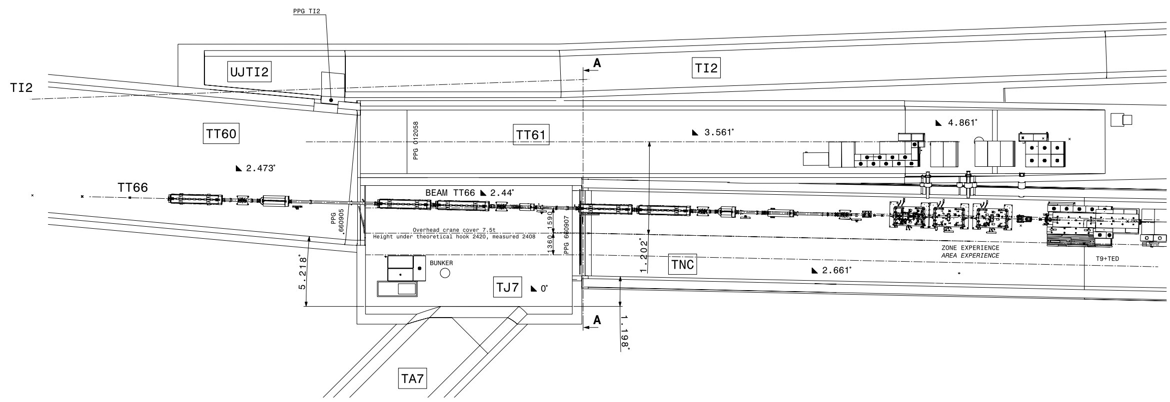

Figure 2.10: Technical drawing of the start of the TT61/TNC complex. In the TCC6 (TT60) cavern and in TNC, the transfer line of HiRadMat can be seen, while in TT61 the electronics shielding of HiRadMat is depicted. The TI2 tunnel houses the LHC Beam 1 extraction.

The extracted beam could then be directed into TCC6 and subsequently into the TT61 or TNC tunnels (Fig. 2.10). These tunnels, previously used in the West Area Neutrino Facility (WANF), are both suitable in terms of geometry and radiation protection constraints. TNC, with a width of 5.8 m, is slightly more spacious than TT61 (4.5 m), and already includes parts of the HiRadMat facility [81] such as the dump. The placement of the beamline would follow the TT61 slope, maintaining the 18° bending angle of the achromatic bend to preserve particle background suppression (Fig. 2.11). The decay tunnel and detector pit would need to be excavated regardless of the exact tunnel selected.

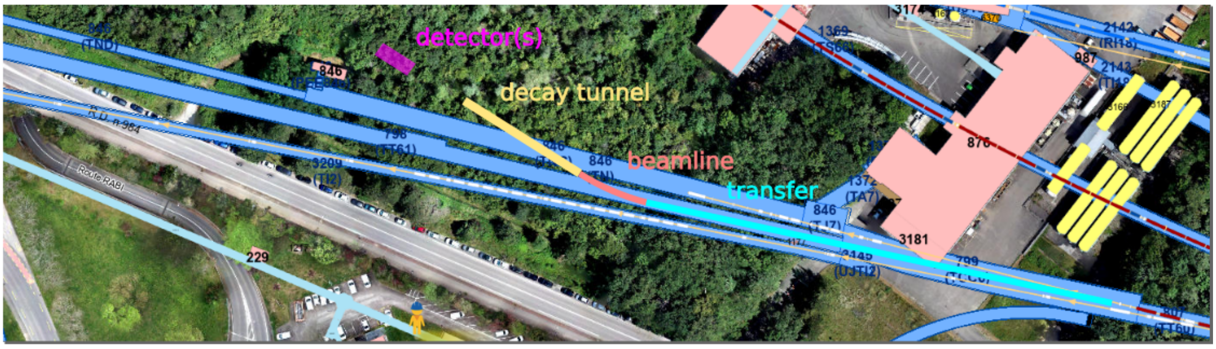

Figure 2.11: Satellite view of the proposed site of the nuSCOPE beamline.

HiRadMat facility does not need to be decommissioned in this case, since the proposed design ensures minimal interference with the facility's operation, except possible access restrictions (that are also valid now, e.g, during the LHC filling). The decay tunnel would be excavated above the TNC tunnel to maintain vertical separation, while a secondary beam dump (described in Sec. 3.5) would be placed between the end of the tunnel and the detector area. A key benefit of this configuration is the short $\sim$ 25 m baseline between the decay tunnel and the detector, which increases neutrino interaction statistics by minimizing the number of secondary decays before the start of the decay tunnel.

To realize this configuration, several modifications of the existing transfer lines at LSS6 are necessary: installation of ZS septa in LSS4, modifications to the SPS orbit (including additional bumper magnets and double orbit bumps), and the construction of a new transfer line with a final focus. The target station in TT61/TNC would resemble that used in K12, featuring a simple graphite target and an XTAX-type beam dump [76].

This layout currently appears to be the most promising option for implementing the nuSCOPE beamline, and therefore, it is the one assumed in this thesis.

2.4 Beamline Instrumentation

As mentioned above, the nuSCOPE proposed beamline (Fig. 2.12) aims to produce kaons and pions with a central momentum of $p = 8.5$ GeV and a momentum bite of $\pm$ 10%. The beamline (along with the target) has been optimized to generate a meson beam that is transported parallel throughout the 40 m long decay tunnel, in order to allow for the decay products to be detected by the specially instrumented tunnel. The entire beamline has a transverse cross-section of 4×4 m^2 and a longitudinal length of approximately 23 m [76].

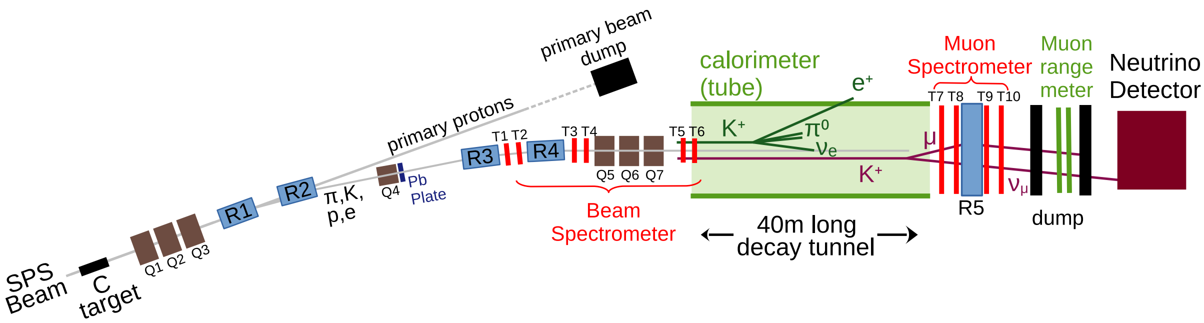

Figure 2.12: Layout of the experimental setup of the nuSCOPE beamline. The beamline (not to scale) combines instrumentation from both ENUBET (in green) and NuTag (in red). The first part of the beamline contains the magnetic optics elements: rectangular bending magnets (blue) and quadrupole magnets (brown). Figure taken from [76]

The beamline instrumentation features three key elements: the calorimeters located along the decay tunnel walls, the instrumented hadron dump, and the silicon pixel trackers. These devices are employed for lepton monitoring and enable a high-precision measurement of both ν_e and ν_μ fluxes. The monitoring relies on the technology and techniques developed over a decade by the ENUBET collaboration. In parallel, the meson reconstruction and tagging system is implemented using four silicon pixel detectors placed on either side of the fourth bending magnet. These trackers provide momentum measurements of the parent mesons. Two additional tracking detectors located upstream of the decay tunnel determine the particle trajectories. The decay muon momentum is measured by four more detectors placed symmetrically around an extra bending magnet positioned downstream of the decay tunnel. The neutrino detectors under consideration for being employed in the nuSCOPE beamline are presented in Sec. 2.5.

2.4.1 Neutrino Monitoring in the Tunnel Wall

In order to monitor the ν_e flux and the high-energy tail of the ν_μ spectrum, large-angle charged leptons originating from kaon decays are detected within the decay tunnel. To this end, the tunnel walls are equipped with a longitudinally segmented sampling calorimeter, selected as a cost-effective option for full-length coverage. This system is complemented by a photon veto, known as the t_0 *layer*, which provides timing information and suppresses photon background [82].

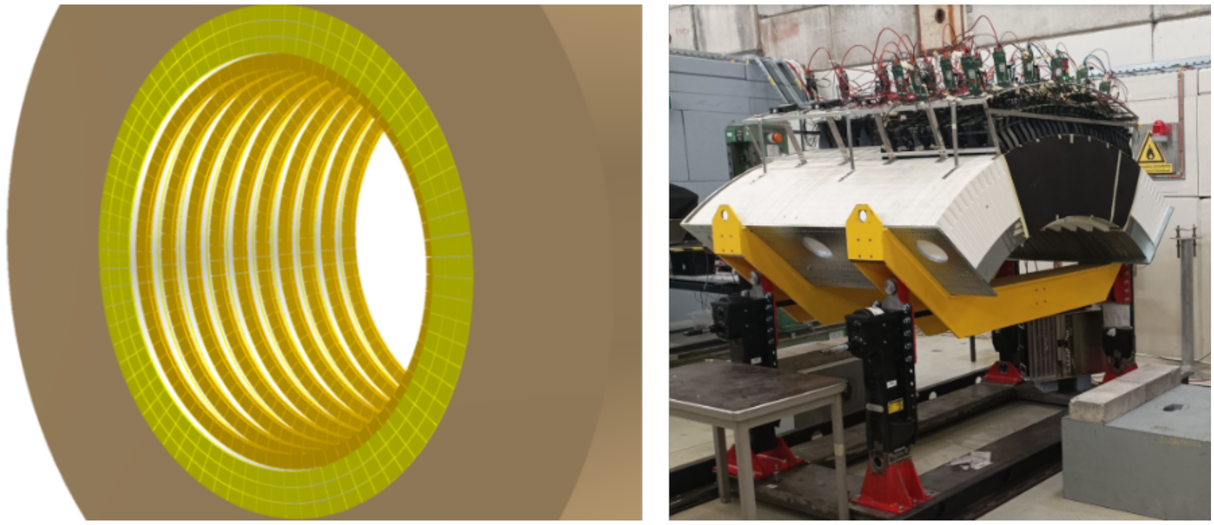

Figure 2.13: *Left*: layout of the instrumented decay tunnel. The three radial layers of calorimeter modules (light green) line the inner wall of the tunnel. Below them, yellow rings of plastic scintillator tiles form the photon veto (t_0 layer). Optical fibres (not shown) transmit light radially outward across the neutron shielding (light brown) to SiPMs (not shown). *Right*: ENUBET demonstrator module during a test beam at CERN-PS. Figures adapted from [76].

Each calorimeter module, called Lateral Compact Module (LCM), consists of alternating layers of iron and plastic scintillator: five iron plates (1.5 cm thick) interleaved with four scintillator tiles (0.7 cm thick), for a total module depth of 11 cm (equivalent to $4.3X_0$). Scintillator tiles have a transverse size of 3×3 cm^2. The modules are arranged in three concentric radial layers, each covering 1.825° of azimuthal angle. The photon veto system consists of scintillator rings installed on the innermost part of the tunnel. This t_0 layer distinguishes electromagnetic showers initiated by photons from those induced by positrons and provides absolute timing for particle identification [76].

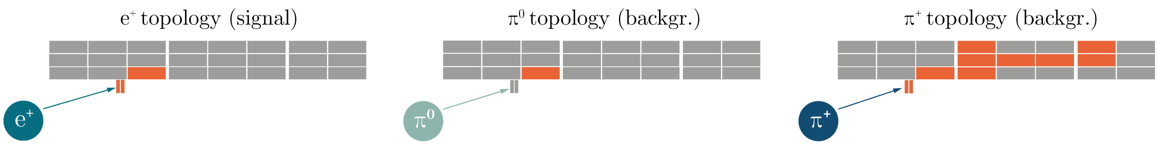

Figure 2.14: Energy deposition patterns in the calorimeter for different particle types. *Left:* e^+ creates a compact electromagnetic shower. *Center:* π^0 mimics e^+ showers but is vetoed via photon detection. *Right:* π^+ undergoes hadronic interactions, producing a broader, more diffuse shower. Figure adapted from [83].

Scintillation light from both the calorimeter and the t_0 layer is collected using pairs of Wavelength Shifting (WLS) fibres attached to the front face of each tile. These fibres transport light to Silicon PhotomMultipliers located outside the tunnel, beyond a 30 cm borated polyethylene (BPE) shielding layer. This shielding protects the SiPMs and readout electronics from neutron radiation.

2.4.2 Instrumented Hadron Dump

The low-energy component of the ν_μ flux originates primarily from π^+ decays. This contribution cannot be monitored by the instrumented decay tunnel, as the accompanying muons produced in these decays are nearly collinear with the beam axis and thus fall outside the geometric acceptance of the calorimeter. The only viable method to detect these forward muons is by placing dedicated detectors downstream of the hadron dump. This requirement imposes strict constraints on the layout and performance of the muon detection system [76].

The proposed solution involves installing multiple detector layers interleaved with passive absorbers, enabling the reconstruction of both the spatial and energy distribution of muons through range-out techniques. These layers will be positioned downstream of the hadron dump. A preliminary design of the muon detection system has been developed. The dump consists of a 2 m-long iron block; immediately following it is the first muon station, succeeded by an additional 2 m iron absorber. Seven further muon stations are placed downstream, each separated by 50 cm of iron. This configuration has been optimized such that no detectable muon flux remains beyond the final detection layer.

2.4.3 Spectrometers for Neutrino Tagging

To enable a kinematic reconstruction of neutrinos produced via two-body decays of pions and kaons, the beamline is instrumented with two dedicated spectrometers, located upstream and downstream of the decay tunnel. These are referred to as the *beam* and *muon* spectrometers. Each spectrometer comprises a dipole magnet positioned between two pairs of silicon pixel tracking planes, allowing for precise measurements of charged particle momentum, direction, timing, and spatial coordinates.

In order to minimize the length of the upstream region[2], the beam spectrometer reuses the final bending magnet of the beamline (R4). However, since the downstream magnetic field configuration, due to the final quadrupole triplet (Q5–Q7), can introduce uncertainties, the system includes two supplementary tracking planes (T5–T6) placed immediately before the decay tunnel entrance to accurately determine the beam particle trajectory [76].

The tracking will be performed in 4D, incorporating time-of-flight information for each hit. To reconstruct complete tracks and decays chains and associate them to neutrino interactions, timing resolutions of about 40 ps (beam spectrometer) and 100 ps (muon spectrometer) are required.

[2]It is essential to minimize the length of the beamline upstream of the decay tunnel, since secondary mesons begin to decay immediately after production, causing a lower neutrino yield. For a beamline length of 23 m, approximately 5 % of the π^+ and 30 % of the K^+ will decay before reaching the tunnel.

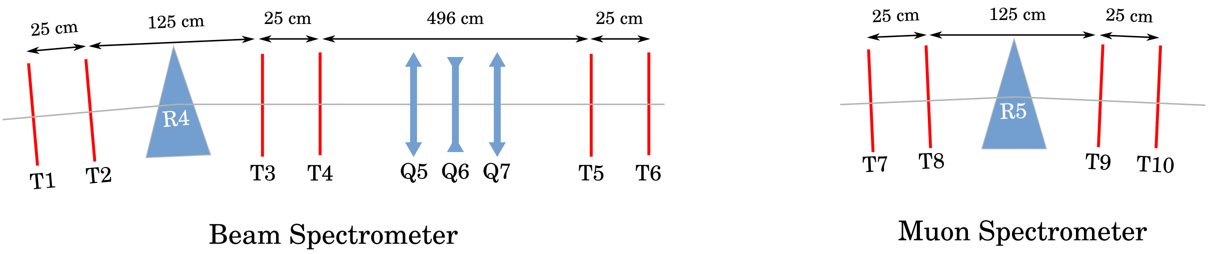

Figure 2.15: Layout of the beam (left) and muon (right) spectrometers. Figure adapted from [76].

This tracking strategy builds on the experience of the NA62 experiment, which developed radiation-hard silicon pixel sensors capable of operating at fluxes of up to 2 MHz/mm^2 with a timing precision of 130 ps [73]. For the muon spectrometer, a hybrid technology is foreseen: fast silicon pixels will be employed in the central region with the highest track density, while more cost-effective and scalable technologies such as Micromegas or scintillating fibres will be used in the outer regions.

To fulfil the stringent requirements of the beam spectrometer, especially in terms of rate capability, cooling efficiency, and material budget, next-generation silicon tracking technologies are necessary. Among the viable options, micro-channel cooling plates represent the most promising solution. These devices, developed for the NA62 GigaTracker [73] and the LHCb VELO upgrade (TimeSPOT) [84], consist of thin silicon substrates, typically a few hundred microns thick, etched with internal micro-channels through which a coolant circulates. While the TimeSPOT technology already satisfies all nuSCOPE requirements, the GigaTracker would require further developments, especially to improve radiation hardness and time resolution.

2.5 Neutrino Detectors

The nuSCOPE beamline is designed to provide accurate neutrino cross-section measurements in the intermediate energy range. To take full advantage of the beamline's precision, the experimental setup will include detectors optimized both for this task and for compatibility with the needs of long-baseline experiments. In particular, argon and water targets are considered to reduce systematics related to nuclear effects across different atomic numbers. The final detector configuration will depend on the specific implementation constraints at the site, but the total fiducial mass is expected to fall in the 500-1000 ton range, given the beam intensity and integrated protons delivered by nuSCOPE [76].

2.5.1 Liquid Argon TPC

Among the argon-based detector options for nuSCOPE, the most suitable candidates are the ProtoDUNE detectors and their upcoming upgrades [85]. During LHC Run 4, these detectors, based on the same technology as the first two DUNE modules, will undergo upgrades to support validation activities for DUNE Phase II [86]. The upgraded ProtoDUNEs, along with the third DUNE module, are expected to retain the imaging and reconstruction capabilities at the GeV scale, while improving the photon detection system. These improvements aim to enhance the performance at lower energies (e.g., for solar and supernova neutrinos) and increase sensitivity to potential BSM signals.

Although the fourth DUNE module is still under R&D and foreseen to include a pixelated readout for better spatial and energy resolution, such upgrades are not strictly required for nuSCOPE. The Phase I DUNE detectors and the ProtoDUNEs are already optimized for neutrinos in the 0.5-5 GeV range, which covers the energy domain of interest. However, implementing neutrino tagging requires a time resolution better than 1 ns, which depends on the number of detected photoelectrons. For this reason, the improved photon detection system under development for Phase II would be a key feature for enabling tagging in a liquid argon detector. An upgraded ProtoDUNE with enhanced photon readout would therefore be a suitable solution for nuSCOPE.

2.5.2 Water Cherenkov Detectors

Water Cherenkov detectors offer lower spatial and energy resolution compared to liquid argon TPCs at the GeV scale, but their simpler construction and lower cost make them attractive for large-scale applications. Since Hyper-Kamiokande uses water as a target material, a water-based detector at nuSCOPE would allow direct cross-section measurements on the same medium, helping reduce systematics from nuclear effects.

At CERN, a water Cherenkov demonstrator called WCTE is now being tested [87]. WCTE is a 40-ton prototype for the Intermediate Water Cherenkov Detector (IWCD) [54], currently in construction in Japan. These detectors are well-suited for fast timing applications, as Cherenkov light propagates faster than argon scintillation light, allowing for sub-nanosecond time resolution even with low photodetector coverage. WCTE also explores the use of multi-PMT modules instead of traditional large-area PMTs, aiming to improve linearity and energy reconstruction.

While the 40-ton WCTE demonstrator is valuable for Hyper-Kamiokande R&D, a larger fiducial mass, on the order of several hundred tons, is needed to meet the nuSCOPE physics goals for water targets. A dedicated water Cherenkov or water-based scintillator detector of this scale would represent the ideal detector for cross-section measurements of relevance for Hyper-Kamiokande.

Chapter 3

Beamline Design

This chapter presents the beamline layout designed for the monitored neutrino beam at the CERN SPS, with a focus on the implementation proposed in this thesis. It describes the configuration and functionality of each key element, including the target, collimator, focusing system, and hadron dump. The design has been optimized to match the ENUBET criteria for narrow-band beams, ensuring precise control of secondary particle fluxes.

3.1 Beamline Description

The nuSCOPE beamline is designed to produce, momentum select, and transport K^+ and π^+ mesons with a central momentum of $p = 8.5$ GeV. The main goal is to deliver a quasi-monochromatic meson beam that stays approximately parallel throughout the 40 m-long decay tunnel. The momentum spread of the beam is equal to 10% and is acceptable for the purposes of the nuSCOPE beamline.

The meson beam is produced from a thin graphite target impinged by 400 GeV protons extracted from CERN's SPS and subsequently focussed by a copper collimator. The first three quadrupole magnets downstream of the target provide the necessary transverse phase advance to maximize the number of secondary particles entering the momentum selection section. Momentum selection is performed by a set of bending magnets that deflect the secondary beam by a total of 18°, selecting particles within a ±10% momentum bite around the central value. A final quadrupole triplet ensures that the beam entering the decay tunnel is collimated and parallel. Primary protons and off-momentum secondaries are directed to the hadron dump where they are absorbed [88].

Many options were studied [88] as proton drivers. At CERN, the only feasible option is the SPS, mainly for the reason of the enhanced meson production yield at 400 GeV compared with lower momenta.

The beamline design has evolved over several iterations, following developments from ENUBET, NuTag, and eventually the nuSCOPE collaboration. A first complete optimization was presented in 2023 by the ENUBET collaboration [64]. Subsequent improvements were implemented by the Conventional Beams Working Group (CBWG) of the PBC study group at CERN [71], and further refined in 2025 by the nuSCOPE collaboration in view of the European Strategy for Particle Physics Update [88].

Parameter	**Value**
Primary proton momentum (GeV)	400
Beamline meson momentum (GeV)	8.5
Proton spill duration (s)	4.8 or 9.6
Spill intensity (protons/spill)	10^{13}
Event rate (THz)	$1-2$
Instantaneous power on target (W)	$170-340$
K^+ yield per proton	$1.3 \cdot 10^{-3}$
π^+ yield per proton	$1.9 \cdot 10^{-2}$
K^+ rate (GHz)	2.7
π^+ rate (GHz)	40
Annual proton intensity (PoT/year)	$2.1-3.2 \cdot 10^{18}$
Total proton requirement	$1.4 \cdot 10^{19}$

Table 3.1: Beamline parameters and specifications of the optimized nuSCOPE beamline. Yields and rates refer to the entrance of the decay tunnel. The total proton requirement corresponds to reaching a 1% statistical uncertainty on the inclusive ν_e cross-section. Adapted from [76].

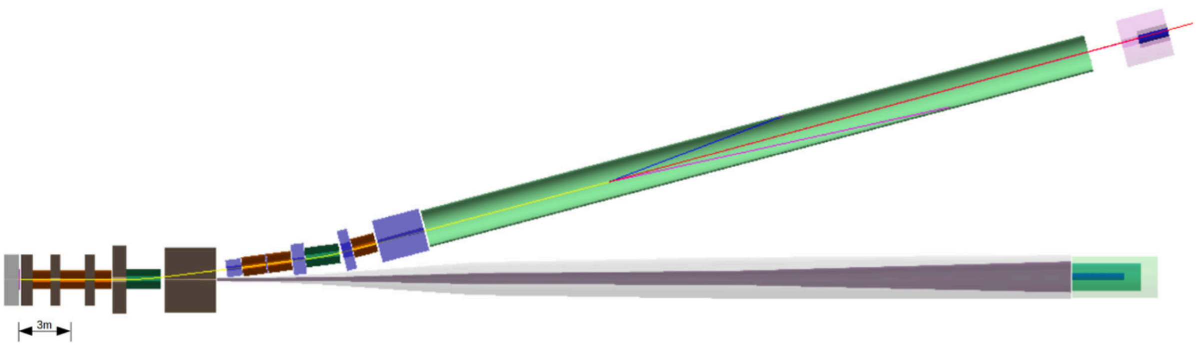

Figure 3.1: The 2023 ENUBET beamline as implemented in G4Beamline, GEANT4, and FLUKA. Protons hit the target (not shown, on the left); secondaries are selected by the transfer line and directed into the decay tunnel (light green). From left to right: the quadrupole triplet (orange) and collimators (brown), a double-bend momentum selection section with two dipoles (green), two quadrupoles, and a momentum collimator (brown), followed by the last quadrupole and two Inermet180 collimators (blue). The instrumented tunnel contains a K_{e3} decay event, where the red track represents the outgoing ν_e. The hadron dump absorbs all particles except neutrinos. Non-interacting protons and off-momentum particles are stopped in the downstream proton dump (dark green). Figure adapted from [64].

The 2025 optimization campaign demonstrated that a piece-wise approach, where the production target and the beamline optics are optimized independently, leads to sub-optimal results [76]. To achieve the best outcome, the target configuration and beamline optics must be carefully matched and optimized in a self-consistent manner. In Table 3.1 are reported the parameters of the optimized nuSCOPE beamline.

The tagging system based on pixel detectors imposes strict constraints on the maximum tolerable particle flux, which is limited to $\mathcal{O}(100\ \text{MHz/mm}^2)$ due to readout limitations [76] The optimization aimed at reducing the flux to $\mathcal{O}(10\ \text{MHz/mm}^2)$ to limit pile-up and ensure efficient detector operation.

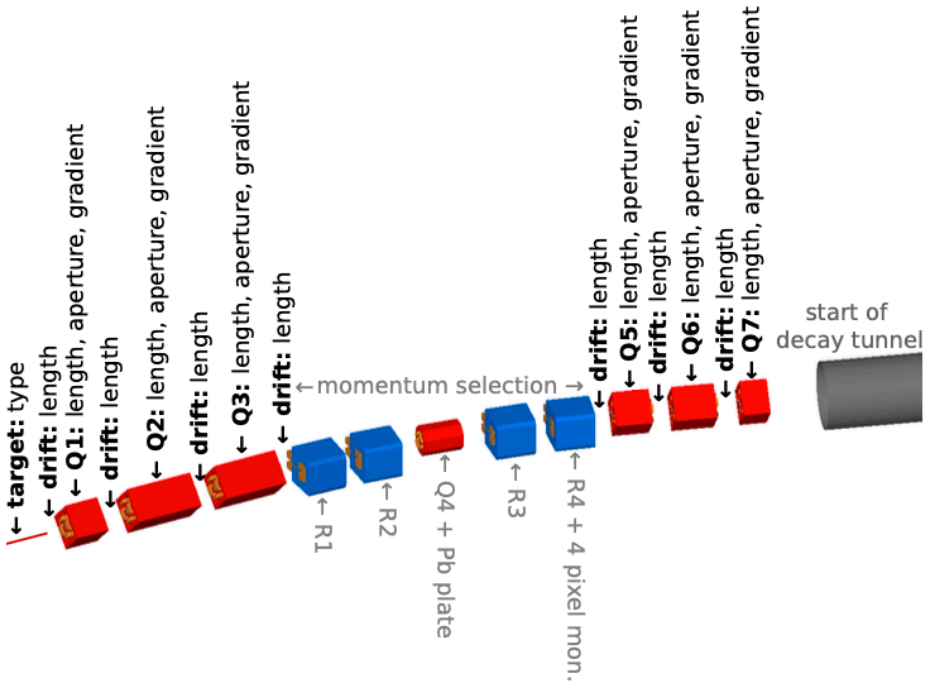

Figure 3.2: 3D layout of the nuSCOPE beamline optimized in 2025. Parameters tuned by the MOGA algorithm are highlighted in black; fixed parameters are shown in grey. Figure adapted from [76].

The beamline design was optimized using a multi-objective genetic algorithm (MOGA), which simultaneously tunes 26 parameters. These include:

- **Drift spaces:** a total of 7 free parameters define the distances between elements in the upstream and downstream quadrupole triplets;
- **Quadrupole parameters:** each quadrupole in both triplets has three free parameters; aperture, length, and gradient, amounting to 18 in total;
- **Production target:** the optimizer selects among 18 precomputed graphite target configurations, varying in length (70-130 cm), radius (2.5-30 mm), and density (1.7-2.26 g/cm^3) – 1 additional free parameter.

Following the optimization, the beamline achieves a K^+ yield of $1.26 \cdot 10^{-3}$ K^+/PoT and a π^+ yield of $1.9 \cdot 10^{-2}$ π^+/PoT within a ±10% momentum bite. Importantly, for a 4.8 s SPS spill containing 10^{13} PoT, the resulting particle flux at the pixel trackers remains within the 10-40 MHz/mm^2 range, well within the operational limits of the silicon detectors.

3.2 Target Optimization

The target is the first element of the beamline encountered by the primary proton beam after extraction from the SPS. Since the production rate of secondary particles – on which the downstream neutrino interaction rate depends – is highly sensitive to the target configuration, selecting an appropriate material and geometry is essential for the nuSCOPE facility.

The optimization of the target was carried out using the Monte Carlo simulation codes FLUKA [89, 90, 91, 92, 93, 94, 95] and G4Beamline [96]. Among the materials considered in the initial studies were graphite, beryllium, and Inconel-718[1], all commonly employed in moderate- to high-power neutrino beamlines.

Graphite is a widely used target material in neutrino facilities due to its ability to withstand high thermal loads and its good meson production performance. Inconel, although already employed at CERN in various contexts [98], shows a slightly lower kaon yield and requires a more complex cooling infrastructure.

The end-to-end optimization performed in 2024–2025 led to a revised configuration. In particular, the optimal solution was identified as a modified version of the former CNGS target [99], featuring a length of 130 cm, a radius of 3 mm, and a density of 2.26 g/cm^3. The target is slightly off-axis (0.5°) with respect to the transfer line in order to reduce the contribute of the so-called wide-beam background (see Sec. 2.1.3.1)

It is worth noting that manufacturing a thin, high-density graphite target with such small dimensions presents technical challenges, because of voids and pores in the manufacturing process [100]. Two strategies were considered: (*i*) constructing a segmented target composed of smaller graphite rods, as in the CNGS design, or (*ii*) reducing the graphite density to 2.0 g/cm^3 to facilitate machining. For the simulations and modelling performed in this thesis, the second option was adopted.

The target and the collimator are housed within a stainless steel shielding structure, similar to the one used today to serve the K12 beamline of the North Area and NA62 experiment [101]. This assembly provides the primary shielding for the two most irradiated components of the beamline, containing the intense radiation produced when the primary proton beam strikes the target and collimator. The shielding block measures 270 cm in

[1] Inconel is a nickel–chromium superalloy developed for high-temperature and high-stress environments. It is widely used due to its resistance to oxidation and corrosion [97].

length and has a cross-sectional area of 240×180 cm^2. Within this block, a hollow cavity is designed to accommodate both the target and the collimator. The total mass of the shielding structure is estimated to be approximately 85 ton.

The exact target housing and geometry details need to be investigated in a dedicated study and lie outside the scope of this thesis.

3.3 Collimator Optimization

In a beamline such as that of nuSCOPE, the target collimator plays a crucial role in the selection and shaping of the secondary particle beam, in particular, the charged mesons produced by the interaction of the primary proton beam with the target. Its primary function is to define the angular and spatial acceptance of the beam, imposing geometric constraints that allow particles with trajectories compatible with the transfer line and decay tunnel to be accepted and transported downstream. In this way, the collimator improves control over the beam, reducing the presence of unwanted particles or particles at excessively large angles, which would otherwise contribute to background or noise in downstream detectors. Furthermore, by limiting the entry of such particles, the collimator protects the beamline components, especially the first quadrupole triplet, from radiation damage and thermal stress. In this context, the collimator becomes a highly irradiated component and may reach high temperatures, requiring careful consideration in its design.

In both the original ENUBET optimization and the updated 2025 version, no collimator was initially simulated. At the beginning of this thesis work, it was assumed that the collimator design could be inherited from the T10 collimator used today by NA62 [101] experiment. The T10-NA62 collimator is constructed from a copper alloy (CuCrZr), chosen for its excellent mechanical and thermal properties. It has a total length of 95 cm, an aperture of 1.5 cm, and is water-cooled to manage the heat load during operation. However, the NA62 beamline is optimized for the transport of very high-energy secondaries (75 GeV), allowing for a smaller aperture to match the highly collimated beam. Moreover, the collimator's considerable length, necessary for the very precise momentum selection in the K12 beamline, introduces an unnecessary amount of material for nuSCOPE. Finally, the use of water cooling introduces additional complexity that is ideally avoided. Although FLUKA cannot simulate detailed heat transfer, it allows for the scoring of deposited energy, which provides an estimate of the instantaneous temperature increase. The necessity of water cooling for nuSCOPE is further discussed in Sec. 4.2.2.

While the thermal and mechanical properties of CuCrZr justify its continued use, the dimensions of the collimator have been revised. In particular, the length has been halved to 50 cm, in order to minimize the material in the beamline and reduce the loss of secondaries, especially kaons, due to premature decay before entering the decay tunnel.

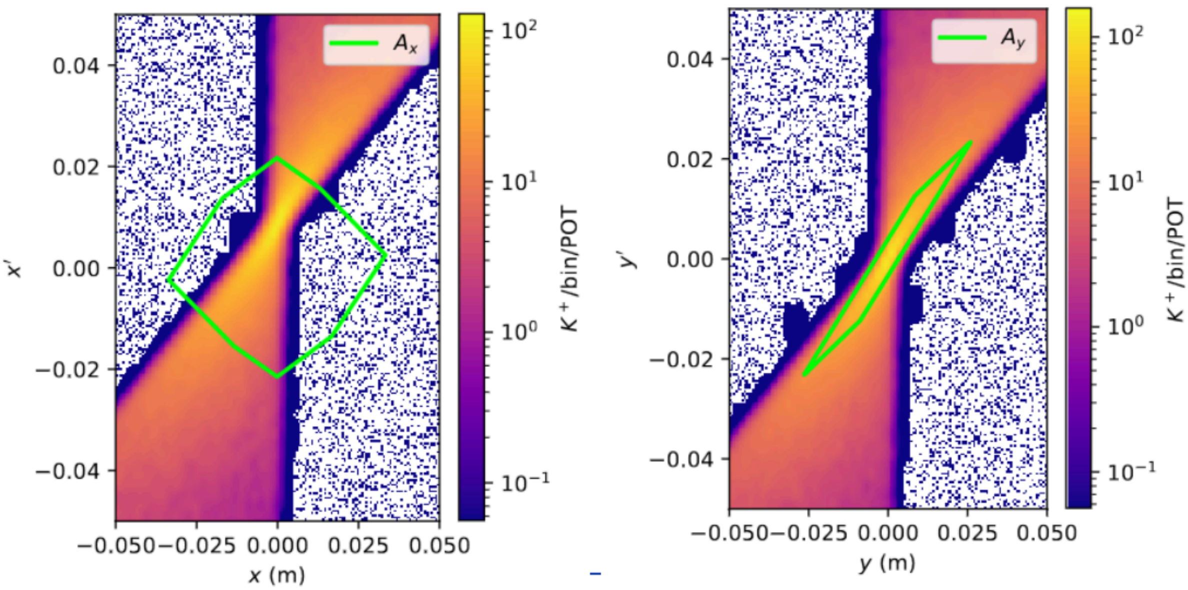

Figure 3.3: Optimized angular and spatial acceptance profiles of the secondary beam at the end of the target. The plots show the x–x' and y–y' phase space projections, with the green contours defining the accepted region. Figure adapted from [88].

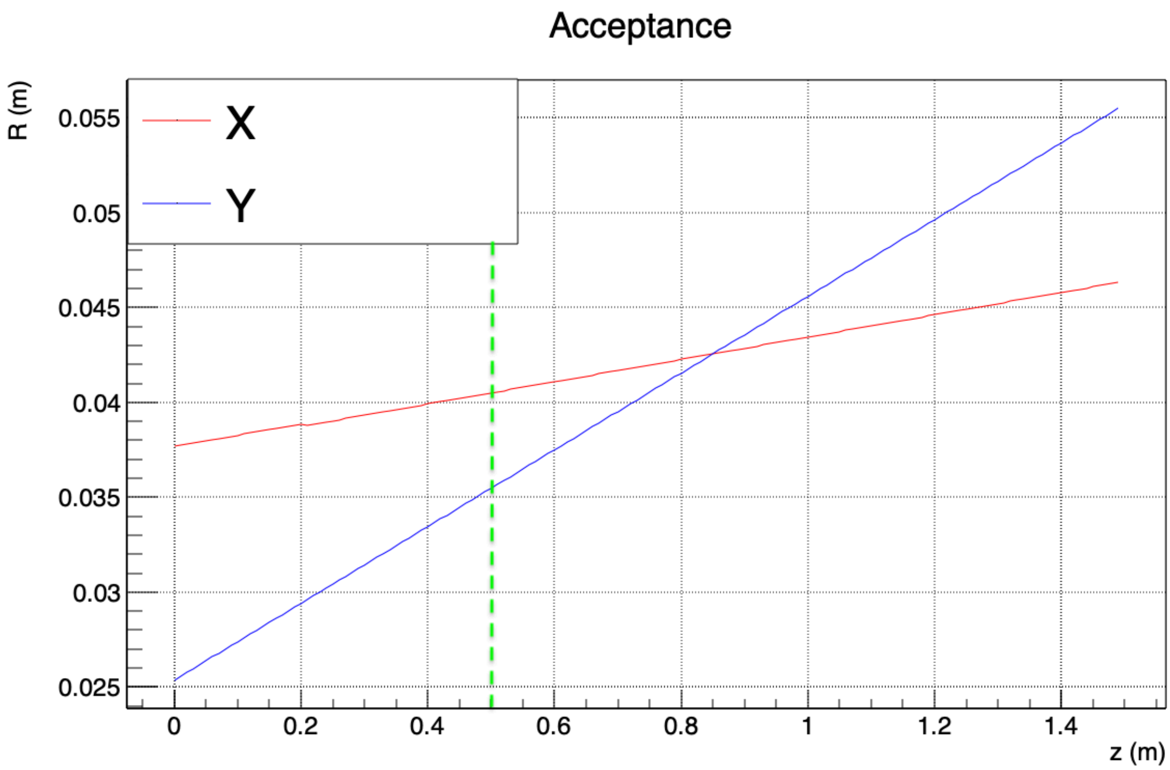

Figure 3.4: Evolution of the beam envelope in physical space (x and y) as a function of distance from the end of the target. A collimator length of 50 cm is indicated by the green line. The maximum of the two transverse dimensions (in this case x) determines the chosen collimator radius.

The initial optimization campaign was performed analytically. The geometric acceptance of the beam immediately downstream of the target was calculated during the 2025 re-optimization. Figure 3.3 shows the phase space distribution of the secondary particles in the x–x' (and equivalently y–y') plane. Using this information, it is possible to extrapolate the evolution of the beam envelope along the beamline. Figure 3.4 presents this evolution as a function of the distance from the target. A total collimator aperture of 48.6 mm radius was selected based on this initial study.

This first optimization used a single degree of freedom: the radius of the collimator aperture. While effective in reducing material, the approach is purely geometric, treating x and y symmetrically and ignoring the actual figure of merit, the number of kaons within the momentum bite ($p = 8.5$ GeV $\pm$ 10%) that reach the decay tunnel. A second optimization campaign was thus performed after implementing the full nuSCOPE transfer line in FLUKA.

The second campaign proceeded in two steps. First, a 1D scan of pion and kaon yields at the entrance of the decay tunnel was performed. Figure 3.5 shows that the yields begin to decrease significantly below a collimator radius of 30 mm, remaining approximately constant above this value. Based on this, a second, 2D optimization was carried out, allowing independent variation of x and y dimensions.

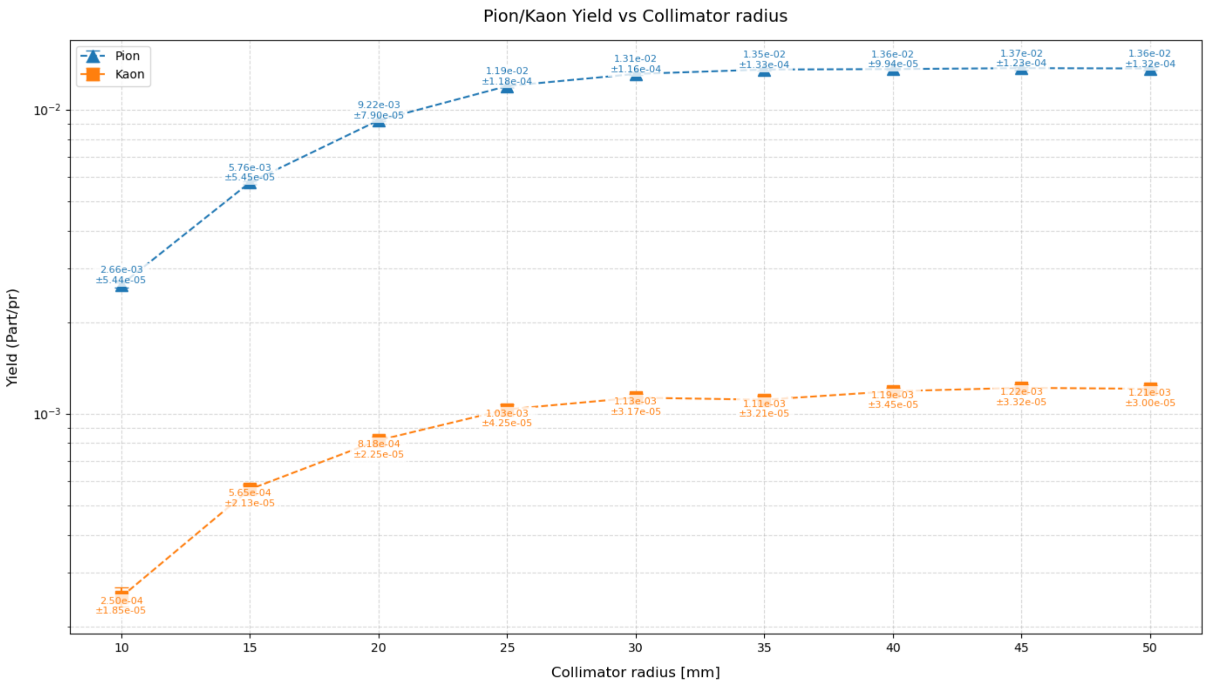

Figure 3.5: Pion and kaon yield at the entrance of the decay tunnel as a function of the collimator radius. Yield drops significantly below 30 mm, indicating the minimum acceptable aperture.

For the 2D optimization, the aperture shape was changed from circular to square, leading, in a first approximation, to a 21% increase in front surface area[2]. The dimensions in x and y were varied from 10-50 mm in steps of 5 mm. The results are shown in Fig. 3.6, where each cell represents a combination of x and y dimensions. The contours indicate 90% (green), 95% (blue), and 98% (red) yield levels with respect to the maximum configuration. Errors are not shown for clarity but remain small: 0.3–0.5% for pions and 1–1.5% for kaons, decreasing with aperture size.

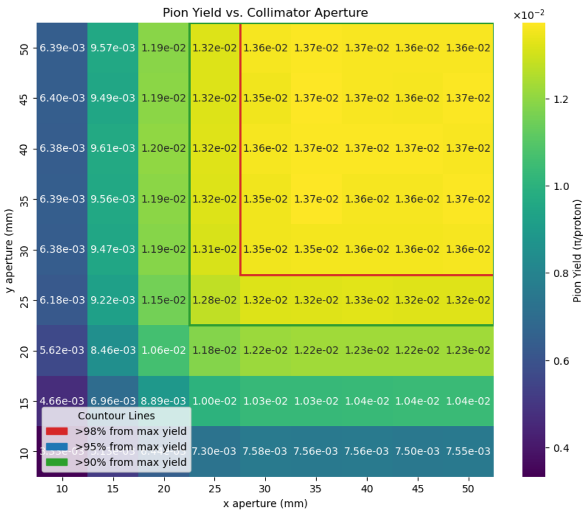

(a) Pion yield heatmap.

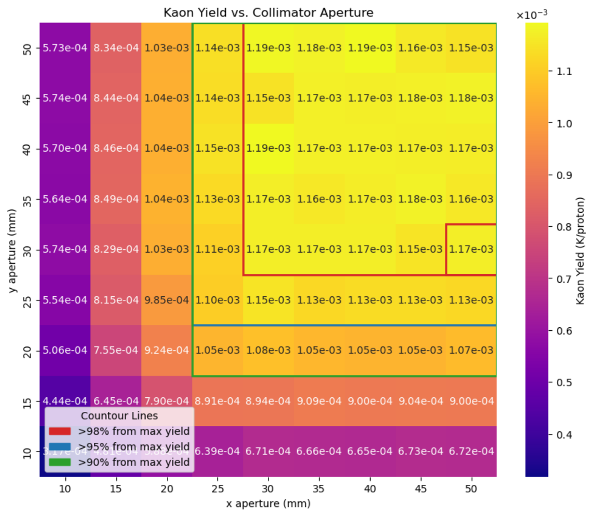

(b) Kaon yield heatmap.

Figure 3.6: Pion and kaon yield per primary proton as a function of the square aperture dimensions in x and y. Each cell corresponds to a specific configuration in x and y. Contours represent 90%, 95%, and 98% of the maximum yield.

The simulation confirmed the result of the 1D study: a square aperture of 30×30 mm^2 provides negligible secondary beam loss (<2%). Thus, the final collimator design adopted for the nuSCOPE beamline consists of a 50 cm long CuCrZr block with a 30×30 mm^2 square aperture.

Figure 3.7 shows the number of π^+ and K^+ produced per primary proton as a function of the distance along the beamline, together with their ratio. A notable drop in the number of particles is observed at the location of the collimator, which is designed to remove off-axis secondaries. Downstream of the collimator, the number of both species decreases approximately exponentially, indicating that no major beam losses occur along the rest of the transfer line. The π^+/K^+ ratio increases with distance due to the shorter lifetime and lower Lorentz boost of kaons, which makes them more likely to decay or get lost in the beamline components, such as magnet apertures or the beam pipe walls.

[2]This estimate compares the area of a circle and square with the same aperture; the circle has $\pi/4 \approx 78.5\%$ of the area of the square.

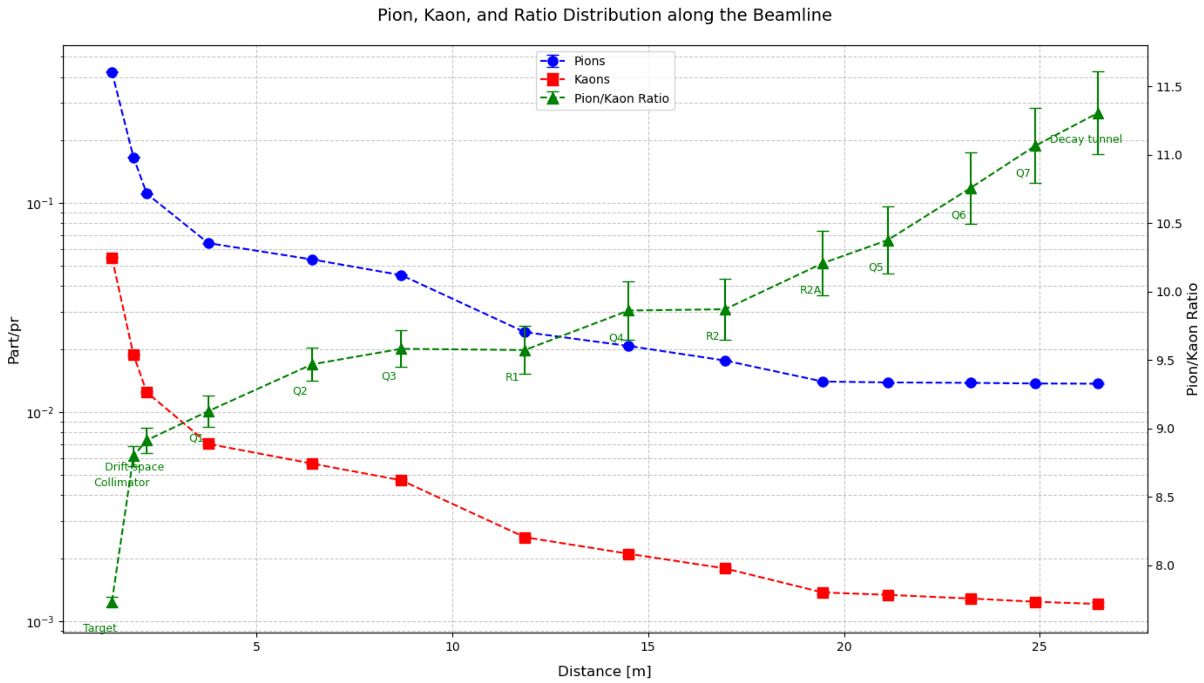

Figure 3.7: Yields of π^+ and K^+ per primary proton and their ratio along the beamline. Triangles indicate the π/K ratio at various beamline positions, labelled according to the component where the meson flux is measured.

3.4 Transfer Line and Static Focusing System

The proton extraction scheme places a significant constraint on the design of the nuSCOPE neutrino beamline, which adopts a static focusing approach using dipole and quadrupole magnets, rather than relying on a magnetic horn [64]. Magnetic horns are challenging to operate with extraction times longer than a few milliseconds, due to the Joule heating experienced by their conductors, and have not been considered anymore for nuSCOPE given the good performance of the ENUBET static focusing system [45]. In addition, since nuSCOPE is conceived as a narrow-band beam, the use of static focusing elements is a natural choice: achieving precise momentum selection of secondaries would require dipole and quadrupole magnets even in the presence of a horn and fast extraction.

The first complete optimization took place in 2023, which demonstrates that an entirely static beamline design could satisfy the requirements of precision neutrino beams [64, 71], especially in terms of PoTs and neutrino interaction at the detector. One key outcome of this study was the inclusion of a 5 cm-thick tungsten filter ($\sim 14.3X_0$, $0.5\lambda_0$), placed immediately downstream of the target to reduce the positron background produced by the interaction of protons in the graphite.

The 2025 optimization campaign built upon the original ENUBET beamline layout and led to a notable improvement in the transmission of both K^+ and π^+. The transfer line was redesigned, and the previous 5 cm tungsten absorber for positron suppression was replaced by a thinner 1.2 cm lead plate positioned after the central quadrupole.

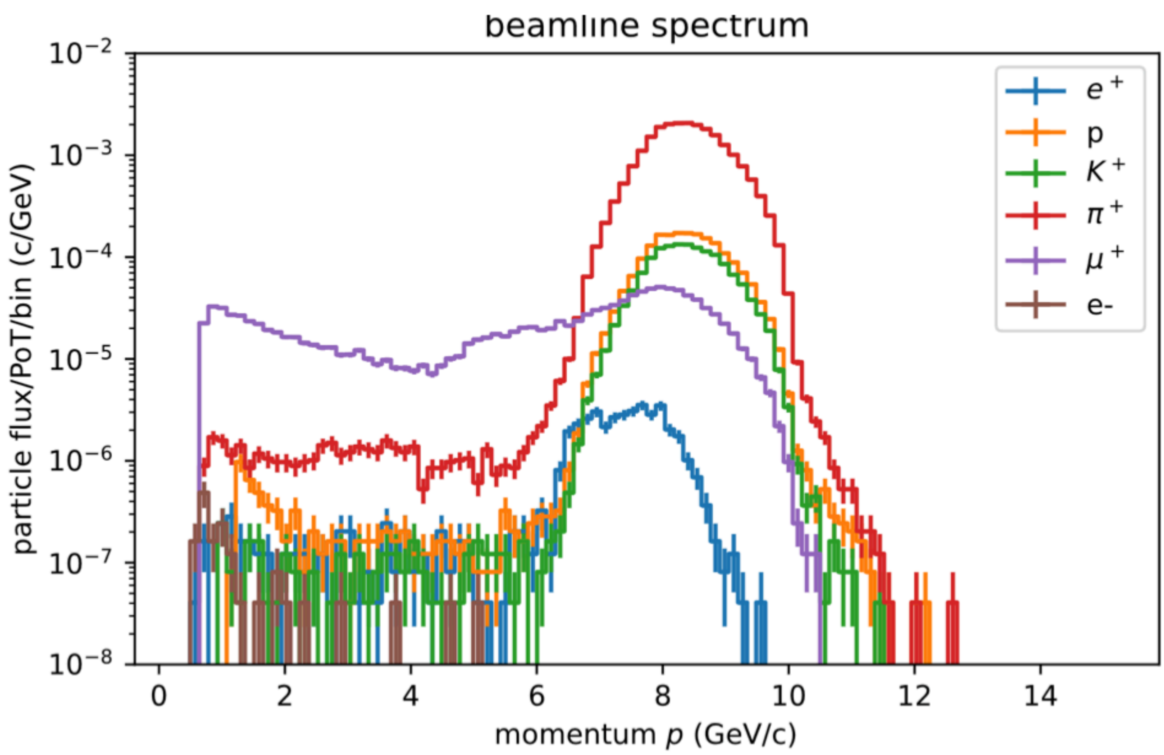

Figure 3.8: Beamline spectrum at the start of the decay tunnel for the optimized nuSCOPE beamline. The positron transmission through the beamline is severely reduced due to the addition of a lead plate followed by two bending magnets. Figure taken from [88].

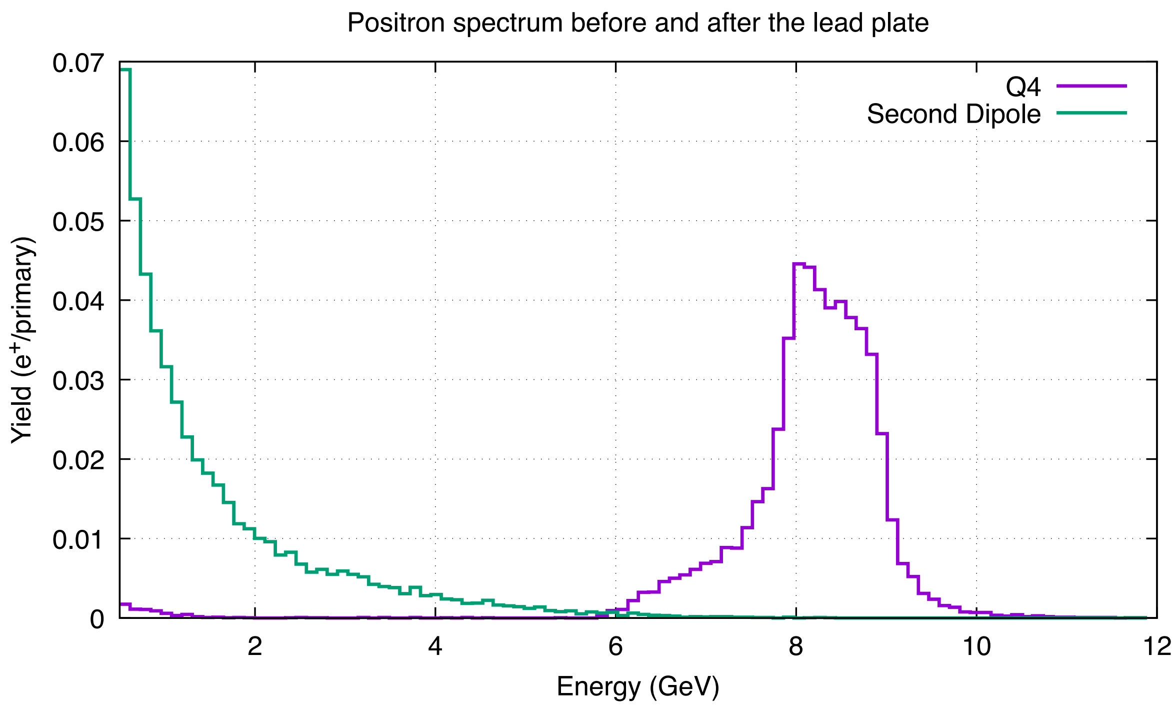

Figure 3.9: Positron spectrum before the lead plate (purple) and after it, at the second dipole (green).

The introduction of silicon pixel trackers posed the challenge of mitigating the large number of positrons produced in the graphite target. Without an appropriate countermeasure, the total particle flux at the monitors would exceed 100 MHz/mm^2 for spill intensities of a few 10^{12} PoT, thereby compromising momentum and position measurements on a particle-by-particle basis and significantly degrading the tagging performance of nuSCOPE. To address this issue, the lead plate was introduced as a dedicated positron filter.

Figure 3.8 shows the particle spectra at the entrance of the decay tunnel for the updated nuSCOPE beamline, while Figure 3.9 depicts the positron spectra before and after the lead plate.

3.4.1 Dipoles

A fundamental component of a narrow-band beamline is the dipole magnet, which is utilised to deflect particles along the horizontal plane in order to select the momentum of secondaries. nuSCOPE current dipole configuration employs three magnets[3], the dimensions and magnetic fields of which have undergone multiple optimization iterations. Fundamental parameters, such as dipole length and magnetic field strength, were selected following the optimization process, while other parameters, including the dimensions of the front section, are derived from an existing dipole model currently in the CERN database [102]. In the following table are presented the different parameters of the dipoles in the nuSCOPE beamline.

Dipole	**Length (cm)**	**Aperture (cm)**	**B field (T)**	**Tilting angle**
First (R1)	250	12.3×3.8	1.799	9.10°
Second (R2A)	100	12.3×3.8	1.528	3.09°
Third (R2)	150	12.3×3.8	1.527	4.63°

Table 3.2: Parameters of the dipoles in the nuSCOPE beamline.

3.4.2 Quadrupoles

The second magnetic component of a beamline, such as the nuSCOPE, comprises various quadrupoles, which are utilised to shape the beam profile through focusing and defocusing. Specifically, there are seven quadrupoles, which are organised into three distinct sections. The first three quadrupoles are positioned immediately after the target and before the first dipole. The fourth quadrupole is situated between the larger dipole and the two smaller

[3] The first two dipoles of Fig. 3.2 have been merged into one equivalent single dipole to further reduce beamline length.

ones, while the final three quadrupoles are positioned after the dipoles and immediately in front of the decay tunnel.

The fundamental parameters, such as aperture, length, and magnetic field strength, were optimised in a way analogous to that employed for the dipoles. The frontal section was derived from existing quadrupole models, with the PXMQNEFTWP [103] model being utilised for the majority of the components, with the exception of the second quadrupole, which is of a larger size than the others and was modelled on a separate magnet, the PXMQNFBTWC [104].

Quadrupole	Length (cm)	Aperture (cm)	Magnetic gradient (T/cm)
First (Q1)	122	7.283	-0.151
Second (Q2)	201	10.5	0.099
Third (Q3)	161.8	9.247	-0.070
Fourth (Q4)	120	5	0.149
Fifth (Q5)	100.5	10.144	0.121
Sixth (Q6)	145.9	10.484	-0.088
Seventh (Q7)	100.3	10.36	0.049

Table 3.3: Parameters of the seven quadrupoles in the nuSCOPE beamline.

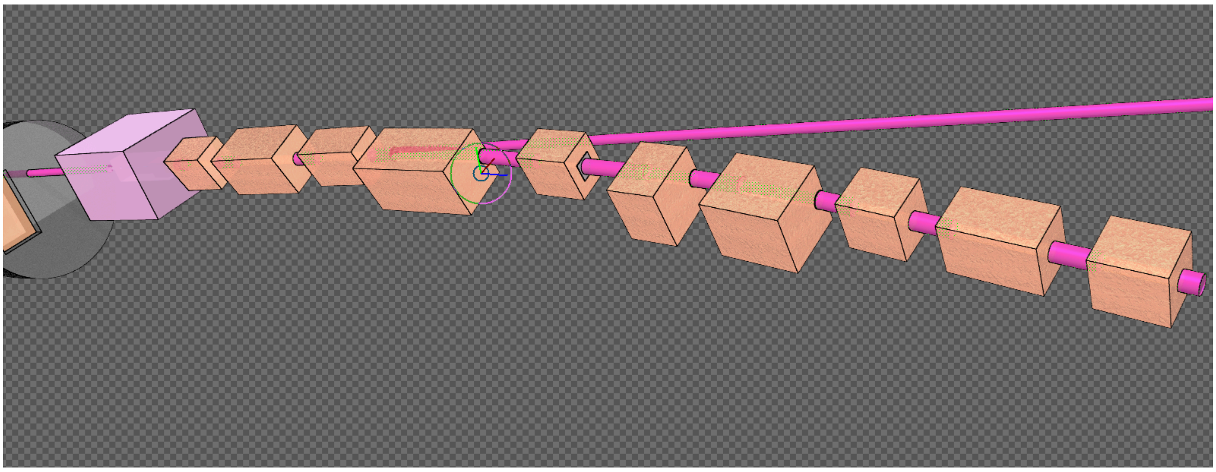

Figure 3.10: 3D rendering of the nuSCOPE static transfer line. In pink, the target station is shown, while the brown regions represent the iron magnets. The dipoles can be distinguished from the quadrupoles because the beam pipe (in magenta) passes through them on the side, whereas for the quadrupoles it passes through the center.

3.5 Proton Dump

In a narrow-band neutrino beamline, the primary proton dump serves a critical role in absorbing non-interacting primary protons and residual hadrons that emerge from the target station but are not selected by the magnetic system. The primary beam dump is positioned 35 meters downstream of the last quadrupole in the beamline. Its design is inspired by the XTAX dump from the NA62 experiment [105], reflecting our intention to reuse and adapt this existing technology. The dump is modular, consisting of eight blocks with dimensions of 80 cm in width, 120 cm in height, and 40 cm in depth. These blocks are composed of different metals arranged in the following sequence: Al-Cu-Cu-Fe-Cu-Cu-Fe-Fe. The entire structure is enclosed within an iron casing with a thickness of 20 cm, providing additional shielding and mechanical stability. In Figure 3.11 is shown a 3D rendering of the primary proton dump.

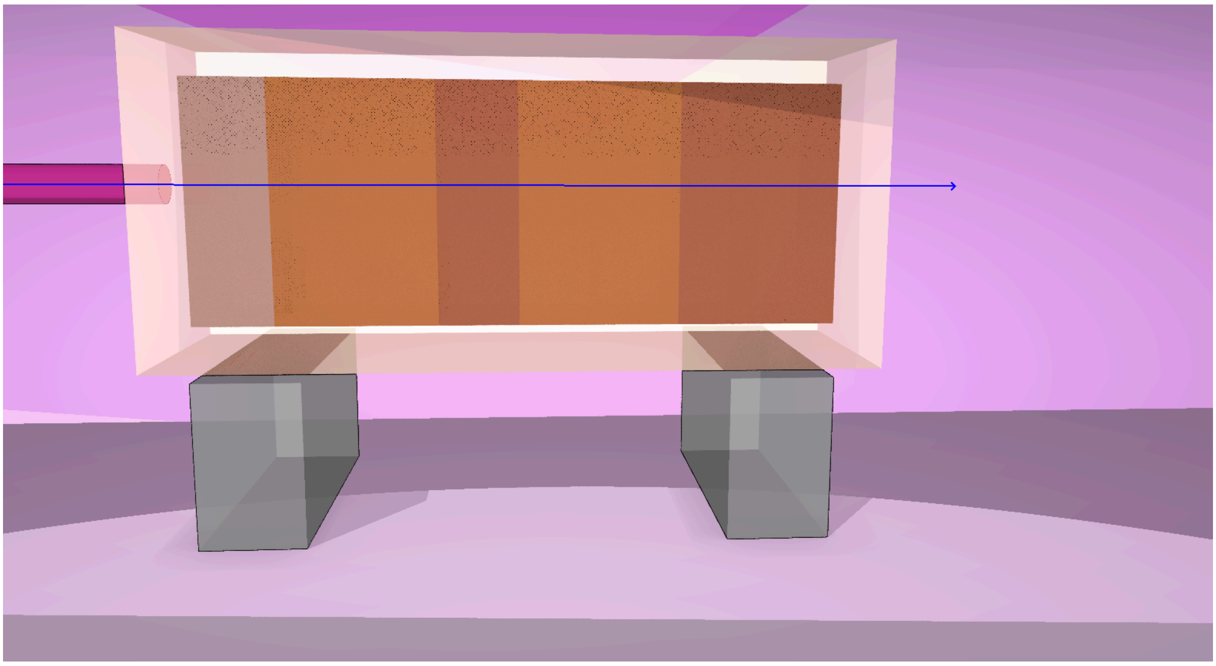

Figure 3.11: 3D rendering of the side view of the dump in the FLUKA model. The primary proton beam, entering from the left, is shown in blue. The iron enclosure is rendered semi-transparent to reveal the internal structure of the dump: the initial aluminium block (light grey), followed by copper (light brown) and iron blocks (dark brown). The entire assembly rests on two concrete supporting blocks.

The choice of materials and their arrangement within the dump is critical to its performance. The sequence is designed to exploit the unique absorption properties of each metal, optimizing the energy dissipation and containment of the beam particles. The first layer, made of aluminium, a low-density ($\rho = 2.7$ g/cm^3) metal, serves a specific purpose: it spreads the incoming beam, ensuring that high-energy particles are distributed more evenly across the subsequent, higher-density absorber layers. This spreading effect reduces localized heating and improves the efficiency of energy absorption in the downstream materials.

Copper and iron layers follow the aluminium, providing a balance between thermal conductivity and high-density absorption properties. Copper, with its excellent thermal conductivity, aids in dissipating the heat generated by the beam, while iron, with its higher density, effectively absorbs and contains the residual energy. By alternating between these materials, the modular design ensures both efficient energy management and mechanical integrity under the intense conditions produced by the beam.

The modular nature of the dump design not only facilitates its construction and maintenance but also allows for potential upgrades or modifications in the future. This approach provides flexibility to adapt the dump to evolving experimental requirements, ensuring its long-term suitability for high-intensity beam operations.

3.6 FLUKA Model Development

The majority of the simulation work carried out in this thesis was performed using the FLUKA Monte Carlo code. This section describes the development of the FLUKA model, focusing on the elements specifically implemented for this thesis and not covered by prior ENUBET or nuSCOPE studies.

FLUKA is a general-purpose Monte Carlo code designed for the simulation of particle interactions and transport of hadrons, leptons, and photons from the keV range (down to thermal energies for neutrons) up to cosmic ray energies, in arbitrary materials. It has been built with the aim of including the best physics models in terms of completeness and precision, through a microscopic approach where each step has sound physics bases. Reliability is pursued by comparing with particle production data at the single interaction level. Results in complex problems, as well as scaling laws and properties, come out naturally from the underlying physics models, and the basic conservation laws are fulfilled a priori. Moreover, the microscopic approach preserves correlations within interactions and among the particle shower components, and it provides predictions where no experimental data is available. FLUKA has been validated against extensive experimental data and is equipped with advanced variance reduction techniques to improve computational efficiency. Transport in magnetic fields is also performed [89].

The nuSCOPE FLUKA model was initially derived from the existing model of the HiRadMat (High-Radiation to Materials) beamline at CERN [106]. HiRadMat is a facility providing high-intensity pulsed beams for testing materials and accelerator components under extreme conditions. It consists of three main underground areas connected to the SPS-to-LHC transfer lines:

- **TNC**: the target and cool-down area;
- **TJ7**: a shielded bunker with direct line-of-sight to the HiRadMat target area;

- **TT61**: a shielded auxiliary tunnel adjacent to TNC.

While all three zones were present in the original FLUKA geometry, their dimensions were reviewed and validated using the latest civil engineering data provided by CERN's SCE department. Special attention was given to the TT61 tunnel, which was selected as the implementation site for the nuSCOPE beamline (see Sec. 2.3.4). TT61 is presently underutilized, housing only a few magnets for their radioactive cooling and the electronics shielding of HiRadMat structure occupying roughly 2×30 m^2 at the tunnel entrance.

The TT61 tunnel connects the TCC6 cavern to the basement of Building 804 and comprises two segments with different inclinations: the first 34 m section slopes upward at 3.56°, while the second section, reaching Building 804, inclines at 4.86°. Horizontally, TT61 diverges from the TNC line by about 2.3°. The tunnel has a maximum width of 450 cm and a height of 330 cm. Despite some technical limitations in defining complex geometries in FLUKA, the implemented tunnel profile deviates by no more than 5 cm from the real structure, primarily near the upper corners.

The nuSCOPE beamline is placed approximately 105 m downstream of the TCC6-TT61 door, within a service alcove. This alcove had to be enlarged in the simulation to host the target station and its shielding while maintaining personnel access. A preliminary enlargement to 28 m in length was adopted, though the final geometry will require a detailed excavation and integration study by CERN's SCE group as part of the nuSCOPE technical proposal.

Downstream of the beamline, the decay tunnel, hadron dump, and neutrino detector are hosted in a newly excavated tunnel, inclined at 16.8° to match the beamline trajectory while remaining parallel to the surface. Since the beamline rests on the TT61 tunnel, which is inclined vertically, to correctly enter the new tunnel, it must tilt downwards. In the model, all beamline elements are inclined by 16.3° relative to their own axes to achieve the desired geometry. The vertical and horizontal offsets between the TT61 and TNC lines naturally avoid intersections between them.

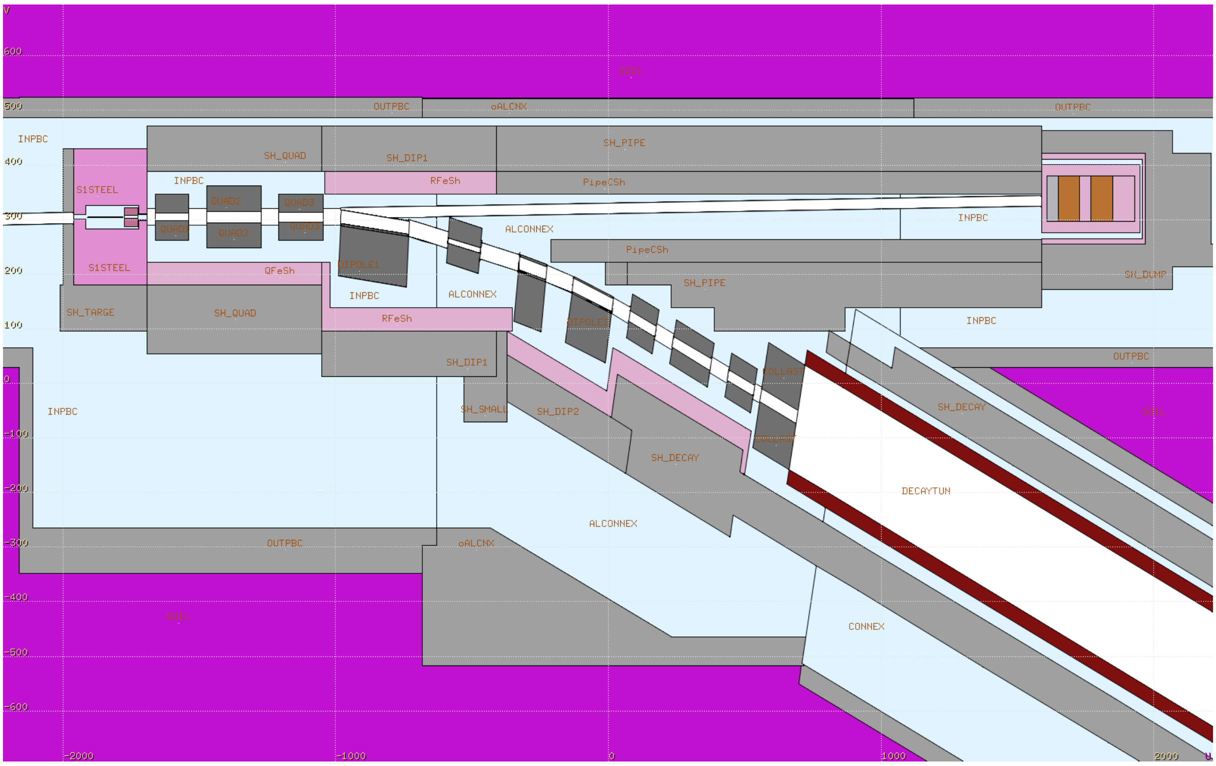

Figure 3.12: Top view of the complete nuSCOPE beamline implemented in FLUKA. On the left, the target is enclosed in a high-strength low-alloy (HSLA) steel shielding structure and is followed by magnetic focusing and momentum-selection elements, dipole magnets (dark gray) and collimators, embedded in a hut composed of cast iron (pink) and concrete (gray). The selected charged secondaries, mostly π^+ and K^+, traverse air-filled and vacuum regions before entering the decay tunnel (right, in dark red), where they decay to produce neutrinos. At the tunnel's downstream end lies the hadron dump, with the same material colouring convention used in Fig. 3.11.

Chapter 4

Temperature effects on the beamline

This chapter investigates the thermal effects on the magnetic elements and the target induced by the particle flux along the beamline, focusing on components exposed to significant energy deposition. The analysis combines FLUKA simulations with simple calculations of adiabatic temperature increase to estimate temperature profiles and assess potential risks to beamline integrity. Special attention is given to critical regions such as the hadron dump, collimators, and shielding. The last section provides a very preliminary and basic assessment of the thermal stresses endured by the target.

4.1 Normalization of FLUKA results

FLUKA does not directly compute temperature changes; instead, it provides the energy deposited in each material. To assess thermal effects, this energy deposition must be translated into an equivalent temperature increase using appropriate material parameters such as specific heat capacity and density. This approach ensures that the simulation output can be used to estimate the thermal response of the system under study. It must be noted here that this approach is "simplistic", in the terms that it only calculates the prompt, adiabatic temperature increase and does not take into account neither the cumulative effect from subsequent pulses, nor the cooling of the material via radiation, convection or conduction. These calculations are to provide a "first order" estimate of the melting (or not) of the material under the effect of one beam pulse.

4.1.1 Energy-Temperature Conversion

The change in internal energy of a material is given by the relation:

$$\Delta E = mc\Delta T \tag{4.1}$$

where ΔE is the energy increase, m is the mass of the material, c is the specific heat capacity, and ΔT is the temperature change. As mentioned, FLUKA provides the energy density $\frac{\Delta E}{\Delta V}$, i.e., the energy deposited per unit volume. Substituting into equation 4.1 and introducing the density $\rho = \frac{m}{\Delta V}$, the equation can be rewritten as:

$$\frac{\Delta E}{\Delta V} = \rho c \Delta T \tag{4.2}$$

Introducing the shorthand $U = \frac{\Delta E}{\Delta V}$ to denote the energy density as provided by FLUKA, the temperature increase can be expressed as:

$$\Delta T = \frac{U}{\rho c} \tag{4.3}$$

This expression relates the FLUKA-scored energy density to the temperature increase through the material constants ρ and c.

For instance, for graphite a density of $\rho = 2.0$ g/cm^3 and heat specific capacity $c = 0.709\ \mathrm{J} \cdot \mathrm{g}^{-1} \cdot \mathrm{K}^{-1}$ is assumed, leading to a product $\rho c = 1.418\ \mathrm{J} \cdot \mathrm{K}^{-1} \cdot \mathrm{cm}^{-3}$. Since FLUKA provides energy in GeV, we convert units using the factor:

$$1\ \mathrm{J} = 6.2415 \cdot 10^9\ \mathrm{GeV} \tag{4.4}$$

which yields the following normalization constant:

$$(\rho c)^{-1} = \frac{1}{1.418\ \frac{\mathrm{J}}{\mathrm{K} \cdot \mathrm{cm}^3} \times 6.2415 \cdot 10^9\ \mathrm{GeV/J}} = 1.13 \cdot 10^{-10}\ \frac{\mathrm{K} \cdot \mathrm{cm}^3}{\mathrm{GeV}} \tag{4.5}$$

Assuming a beam intensity of $N = 10^{13}$ protons on target per spill, we define a temperature normalisation factor τ as:

$$\tau = N \cdot (\rho c)^{-1} = 10^{13} \times 1.135 \cdot 10^{-10}\ \frac{\mathrm{K} \cdot \mathrm{cm}^3}{\mathrm{GeV}} = 1135\ \frac{\mathrm{K} \cdot \mathrm{cm}^3}{\mathrm{GeV}} \tag{4.6}$$

This factor allows direct conversion from deposited energy density to temperature increase in graphite.

For other materials in the beamline, the same calculations applies, using the appropriate material constants. The resulting τ values are summarized in Table 4.1.

Material	**Norm. Factor τ (K · cm^3/GeV)**	**Component**
Graphite	1135	Target
CuCrZr	473.8	Collimator
Electrical steel	417.2	Magnets
Iron	452.2	Dump
Aluminium	661.4	Dump
Copper	465.8	Dump

Table 4.1: Temperature conversion factors τ for materials in the beamline. Graphite, copper, iron, and aluminium values are taken from [107]; the CuCrZr constants are based on [108]; electrical steel properties are from [109].

4.1.2 Energy-Thermal Stress Normalization

The assessment of thermal stresses in beamline components is fundamental to ensure their mechanical stability and long-term performance under high-intensity beam conditions. When a material absorbs energy from the beam, it undergoes a temperature rise, which induces thermal expansion and consequently generates internal stresses. If these stresses are not adequately addressed, they can result in plastic deformation, cracking, or even structural failure. A proper understanding of such effects is thus vital for the mechanical design and safety of the beamline. Since FLUKA is not a finite element method (FEM) code, it cannot directly compute thermal stresses. The approach adopted in this section is therefore based on simplified analytical models, which rely on significant assumptions. It does not aim to deliver a complete structural analysis; such a study is foreseen in a future work by the nuSCOPE collaboration.

This analysis focuses solely on the target, as the temperature increases in the downstream beamline elements are negligible in comparison with the energy deposited in the target.

Assuming a stationary cylindrical model for the target and a fully thermoelastic regime, the Von Mises stress can be expressed [99] as:

$$\sigma_{\mathrm{VM}} = \sqrt{\frac{(\sigma_z - \sigma_\theta)^2 + (\sigma_\theta - \sigma_r)^2 + (\sigma_r - \sigma_z)^2}{2}} \tag{4.7}$$

where σ_r, σ_θ, and σ_z are the radial, tangential, and axial stress components[1], respectively.

In general, the stress components are not independent. However, as shown in [110], under the assumptions of cylindrical symmetry and isotropy, the radial and tangential stresses can be approximated as:

$$\sigma_r = \sigma_\theta = \frac{\sigma_z}{2} \tag{4.8}$$

[1]The beam direction in FLUKA is conventionally defined as the z axis.

Substituting into Eq. 4.7, the Von Mises stress simplifies to:

$$\begin{aligned}\sigma_{\mathrm{VM}} &= \sqrt{\frac{1}{2}\left[\left(\sigma_z - \frac{\sigma_z}{2}\right)^2 + \left(\frac{\sigma_z}{2} - \frac{\sigma_z}{2}\right)^2 + \left(\frac{\sigma_z}{2} - \sigma_z\right)^2\right]} \\ &= \sqrt{\frac{1}{2}\left[\left(\frac{\sigma_z}{2}\right)^2 + 0 + \left(-\frac{\sigma_z}{2}\right)^2\right]} \\ &= \sqrt{\frac{1}{2} \cdot 2 \cdot \left(\frac{\sigma_z}{2}\right)^2} = \frac{\sigma_z}{2}\end{aligned} \tag{4.9}$$

The axial stress σ_z in a constrained cylinder subjected to uniform heating is given by:

$$\sigma_z = \frac{\alpha E \Delta T}{1 - \nu} \tag{4.10}$$

where:

- $\alpha = 4.1 \cdot 10^{-6}\ \mathrm{K}^{-1}$ is the coefficient of thermal expansion of graphite;
- $E = 12.5 \cdot 10^3$ MPa is the Young's modulus of graphite;
- $\nu = 0.19$ is the Poisson's ratio[2];
- ΔT is the temperature increase.

Combining these relations, the Von Mises stress becomes:

$$\sigma_{\mathrm{VM}} = \frac{\alpha E \Delta T}{2(1 - \nu)} = \frac{4.1 \cdot 10^{-6}\ \mathrm{K}^{-1} \times 12.5 \cdot 10^3\ \mathrm{MPa}}{2(1 - 0.19)} \cdot \Delta T = 3.1635 \cdot 10^{-2}\ \mathrm{MPa/K} \cdot \Delta T \tag{4.11}$$

For convenience, we define $k \equiv 3.1635 \cdot 10^{-2}$ MPa/K. From the previous section, the temperature rise can be written as $\Delta T = \tau \cdot U$, where τ is the normalization factor derived from FLUKA and U the local energy density.

Therefore, the final expression for the Von Mises stress is:

$$\sigma_{\mathrm{VM}} = k \cdot \tau \cdot U = 35.2\ \mathrm{MPa} \cdot U \tag{4.12}$$

The σ_{VM} has been calculated for the target material and compared with the yield strength. The results and conclusions are discussed in Sec. 4.2.

[2] The Poisson's ratio measures the strain response in directions perpendicular to the effective loading direction and it is a propriety of the material. In the present case, the loading is induced by the beam, and the Poisson's ratio characterizes how the material deforms transversely with respect to that beam-induced strain.

4.2 Temperature Increase Studies

4.2.1 Target

The production target (Fig. 4.1), being the first element encountered by the primary proton beam in the beamline, is subject to the highest energy deposition. As a direct consequence, it also experiences the most significant temperature increase among all components.

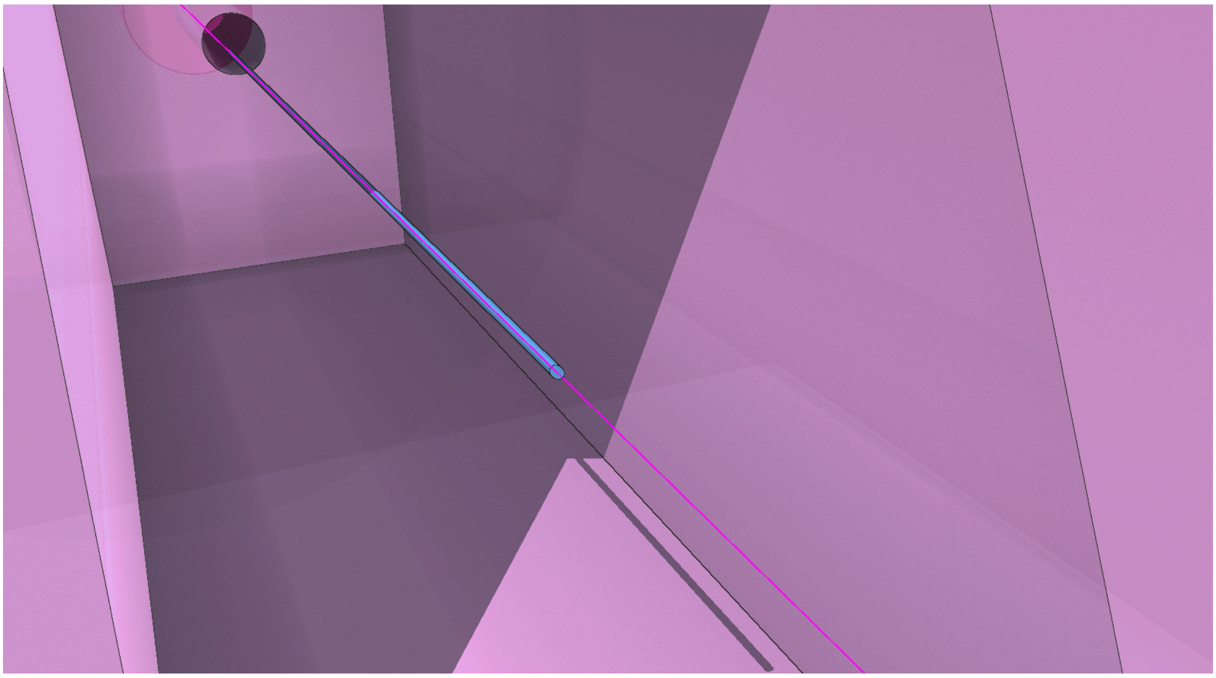

Figure 4.1: 3D rendering of the target complex. The target is a 130 cm-long graphite cylinder with a radius of 3 mm, as described in Section 3.2.

Figure 4.2 presents the spatial distribution of the temperature increase ΔT within the target, projected on a central zx plane. This plane has been selected as the incoming proton beam lies on it, and it is therefore expected to exhibit the highest thermal load. The plot reveals both the temperature gradient along the target volume and and the position where the temperature increase exceeds several hundreds of degrees (in red). The simulation employs a voxel size of $0.2 \times 0.2 \times 4.33$ mm^3, which ensures adequate spatial resolution for capturing fine thermal structures.

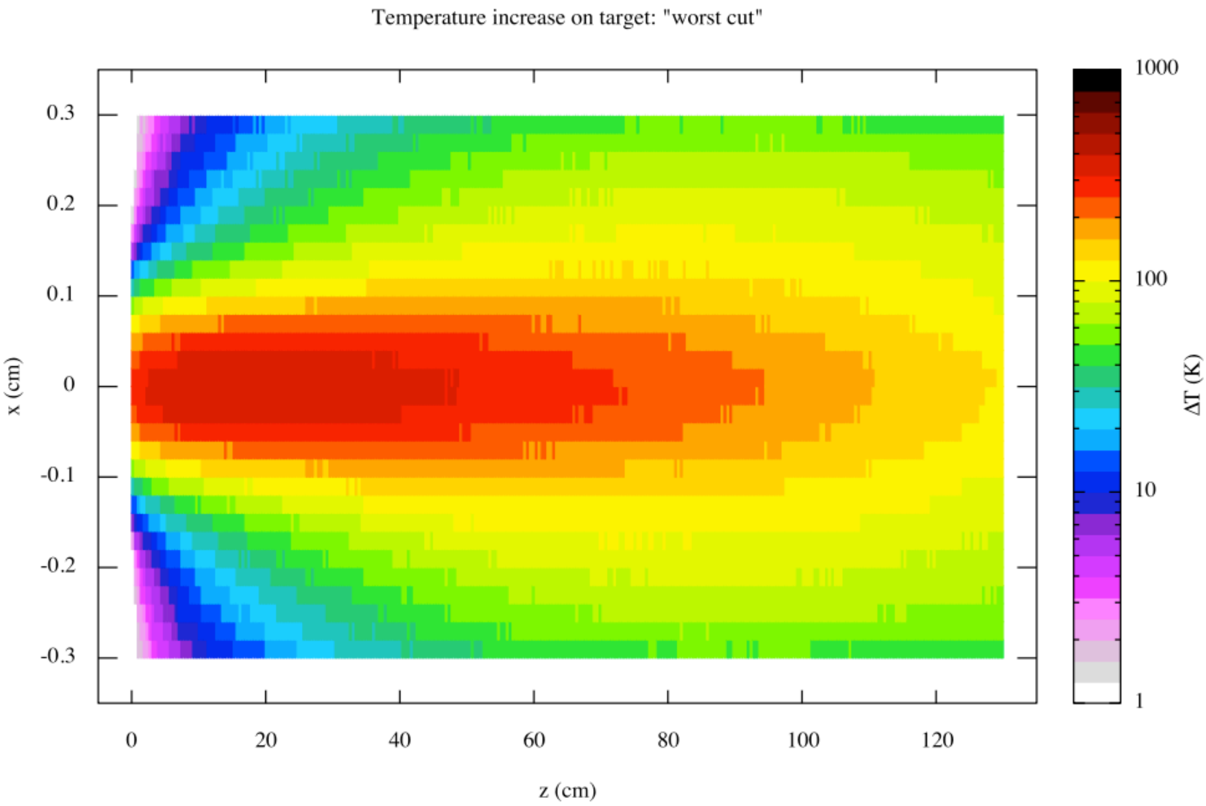

Figure 4.2: Top view of the temperature increase on the target. The figure shows a two-dimensional projection averaged along the y axis. In particular, it displays the central y slice, which presents the highest temperature increase and thus represents a worst-case scenario for thermal analysis.

In Figure 4.3, the distribution of the maximum temperature increase along the longitudinal axis of the is shown. For each longitudinal bin, the figure reports the maximum value of ΔT recorded across the transverse (x, y) directions. Based on the simulated data, the location corresponding to the highest energy deposition, and consequently the peak temperature increase, is found at a depth of 16.5 cm. This position lies at the transverse centre of the target.

The absolute value of the maximum temperature increase in this central region reaches $\Delta T = (402.5 \pm 6.0)$ K per pulse. From the same simulation, the average energy loss per primary proton within the target has been estimated to be (2.483 ± 0.007) GeV, out of the initial 400 GeV provided by the SPS proton beam. This value translates to a total energy deposited in the target during a single spill of 10^{13} PoT equal to (3978 ± 11) J. Correspondingly, this implies a total power dissipation in the target of (828.7 ± 2.2) W for a proton spill of 4.8 s.

The statistical uncertainty on the energy deposition within the target is generally below 1% across nearly the entire volume. An exception is observed in the outer radial regions of the first few longitudinal slices, where fewer primary protons interact due to the still well-collimated beam. However, even in those regions, the statistical error amounts to less than 5%.

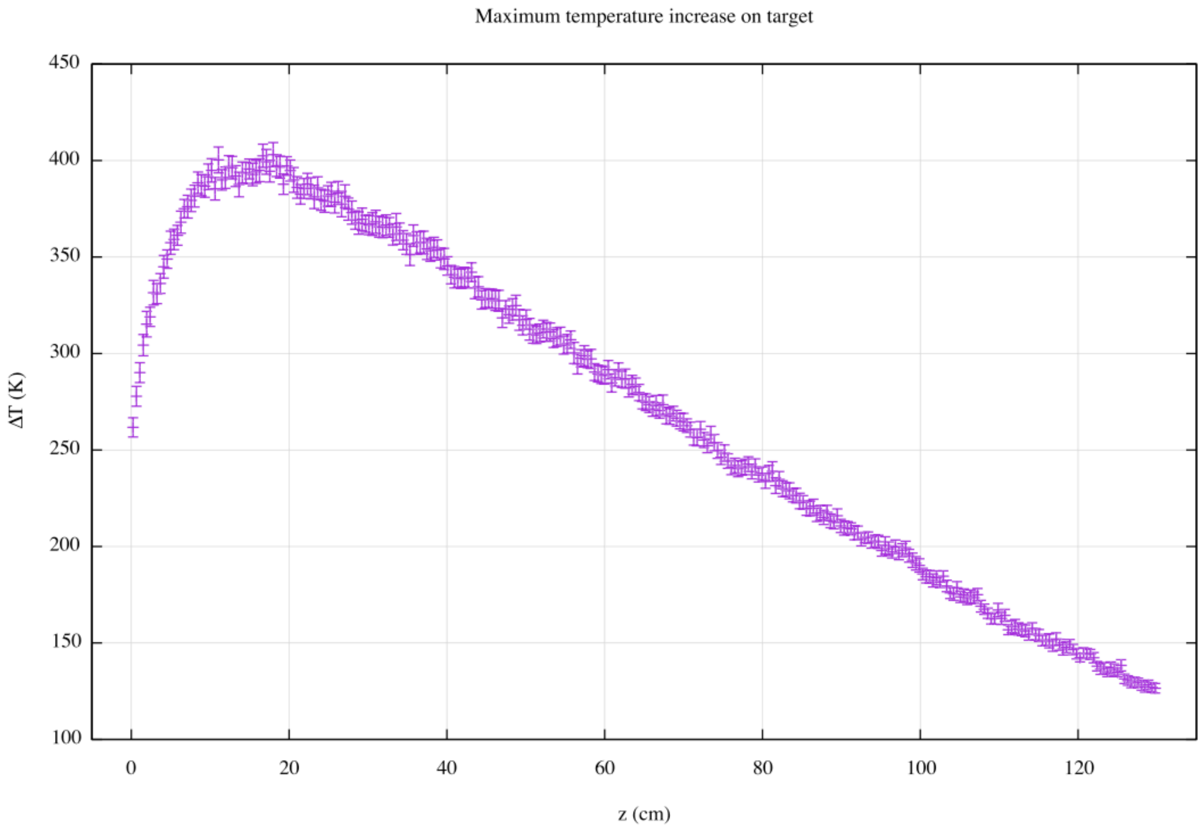

Figure 4.3: Maximum temperature increase along the length of the target. For each longitudinal bin, the maximum ΔT across the transverse plane (x and y directions) is reported.

The temperature increase in the target is particularly pronounced in the first half of the target, reaching values exceeding 400 K. Nonetheless, graphite is well suited to withstand such thermal loads due to its exceptionally high sublimation point[3], which is greater than 4000 K. While this suggests that the structural integrity of the target is not immediately at risk, it is important to consider secondary effects that could arise over time. In particular, when heated to temperatures around 400 °C in the presence of air, graphite begins to slowly oxidize [111]. This surface-level oxidation can gradually lead to erosion, potentially degrading the mechanical properties of the material. If left unchecked over extended periods of operation, this process could result in cracking or structural failure of the target. At this stage, such degradation does not appear to pose a critical risk. The most intense heating is localized deep within the target core, while the surface is subjected to a more moderate temperature increase of approximately 250 K. This is below the threshold typically required to trigger the oxidation process. Additionally, the target is allowed to cool between consecutive spills, and to a lesser extent, even during a single spill due to the relatively slow extraction of protons from the SPS. This cooling

[3] At atmospheric pressure, carbon transitions directly from the solid to the gaseous phase, without passing through the liquid state. In order to obtain liquid carbon, temperatures of at least 4600 K are required, together with a pressure of approximately 10 MPa.

interval further mitigates the risk of thermal-induced damage.

Nevertheless, the long-term implications of repeated thermal cycling and localized heating require careful assessment with the use of FEM tools, and a proper understanding of the steady-state temperature increase with the repetition rate as will be defined by the supercycle composition that will serve potentially this beamline. These future studies remain out of the scope of the present thesis.

4.2.2 Collimator

The collimator (Fig. 4.4) is the second element in the beamline and plays a key role in shaping and constraining the proton beam, impacting the background that will reach the nuSCOPE detectors.

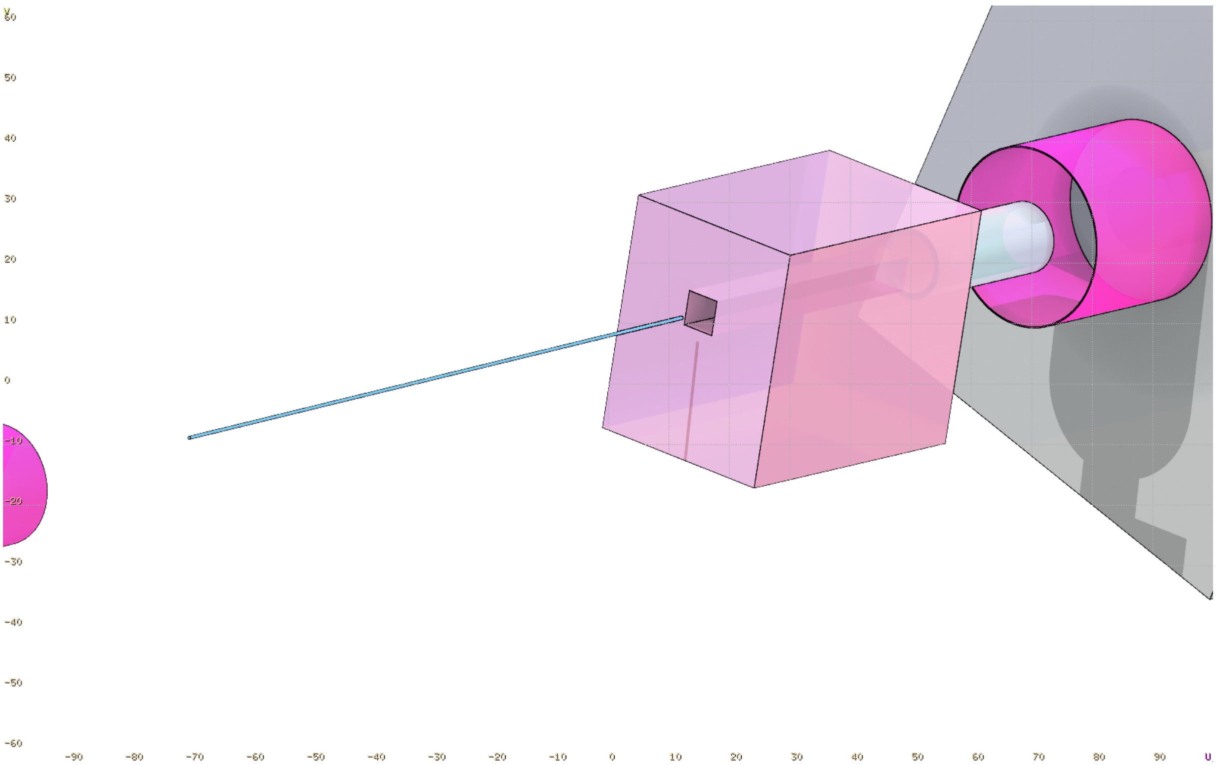

Figure 4.4: 3D rendering of the collimator (pink) and the target (blue); in magenta is depicted the beam pipe while the first quadrupole is shown in gray. The collimator is made of a copper alloy (CuCrZr) and it is 50 cm long, with a cross-section of 31×40.9 cm^2. The collimator has a 30×30 mm^2 square aperture, as discussed in Sec. 3.3.

Detailed FLUKA simulations have been performed to understand the effect of the beam on this collimator. The studies have shown that the energy deposition within the collimator remains relatively low, leading to a modest maximum temperature rise of $\Delta T = (16.11 \pm 0.29)$ K per spill. This limited increase is primarily due to the collimator's robust material properties. Figure 4.5 shows the spatial distribution of the average temperature rise. The simulation employs a relatively coarse voxel size of $1.65 \times 2.045 \times 2.5$ mm^3, which remains adequate to resolve the temperature profile over such a large component.

The statistical error is lower than 2% in any part of the collimator.

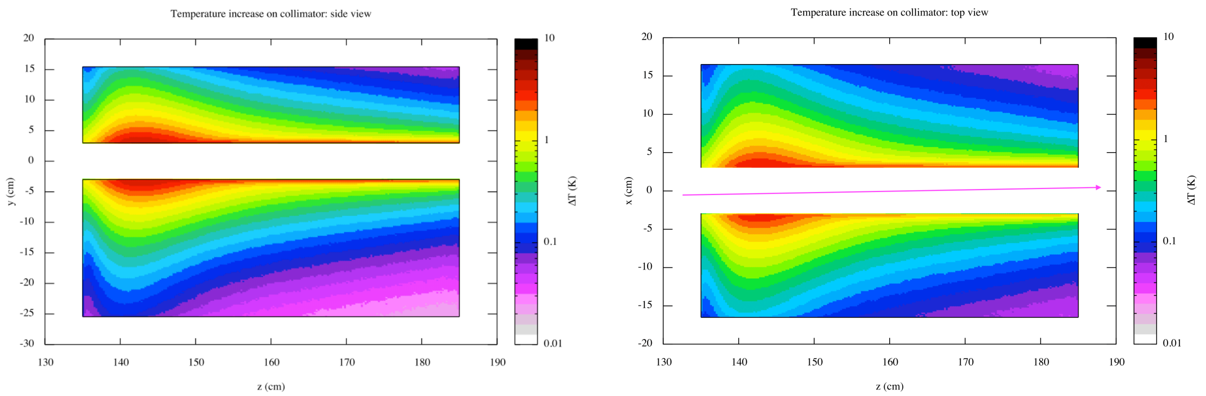

(a) Side view of the average temperature increase on the collimator.

(b) Top view of the average temperature increase on the collimator. In magenta is depicted the trajectory of the primary protons that have not interacted in the target.

Figure 4.5: Side and top views of the average temperature increase on the collimator. The results are normalized to 10^{13} protons per spill impinging on the graphite target.

As shown in Fig. 4.5, the highest temperature rise occurs on the walls of the collimator bore. The slight asymmetry observed between the right and left sides is a consequence of the slight tilt applied to the primary proton beam, introduced to suppress the wide-band background. To better highlight this behaviour, Fig. 4.6 presents a side view of the temperature increase in a vertical cut through the inner left wall, along with its longitudinal profile.

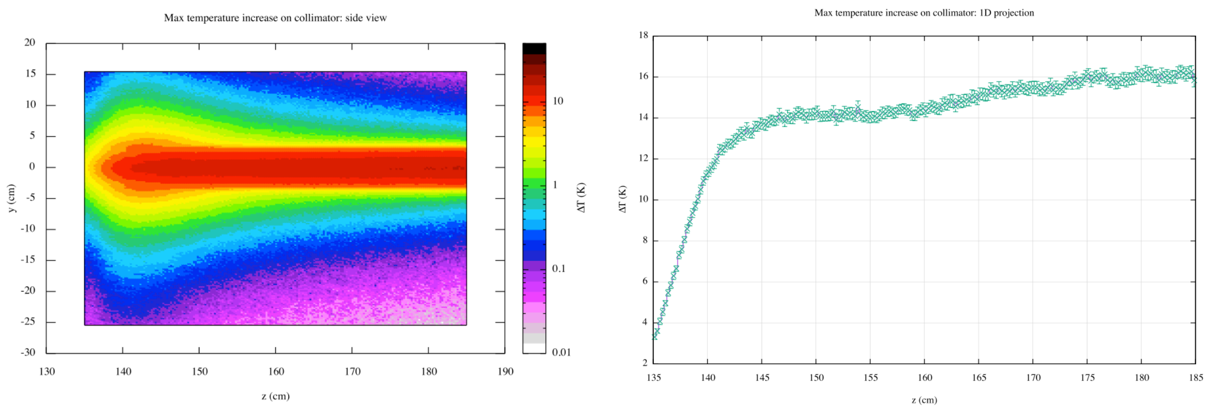

(a) Side view of the temperature increase, showing a vertical cut through the inner left wall.

(b) Longitudinal distribution of the temperature increase along the inner left wall.

Figure 4.6: Maximum temperature increase on the collimator. The peak ΔT is observed along the inner left wall, due to scraping by primary protons that did not interact in the target being closer to this wall of the device than to the right one.

From Fig. 4.6b, it is evident that the deposited energy rapidly increases as the beam begins to enter the collimator, reaching a plateau after approximately 15 cm. Beyond this point, the temperature gradually increases as a larger fraction of primary protons begin interacting with the inner walls of the device. The maximum temperature is reached near the downstream end of the collimator, at a depth of about 48.5 cm.

The total energy deposited in the collimator is (81.01 ± 0.12) GeV/PoT, corresponding to (129.8 ± 0.2) kJ per spill. Consequently, the total power dissipated during a single 4.8 s spill is (27.04 ± 0.04) kW.

The FLUKA calculations show that the nuSCOPE collimator undergoes only a modest temperature increase, on the order of a few degrees, and therefore does not require active cooling. This substantially simplifies operation and reduces overall costs. Furthermore, implementing water cooling would introduce significant radiological concerns.

This configuration differs from the NA62 collimator, which served as the design reference for nuSCOPE. In NA62, the collimator requires active cooling because it handles particles with a much higher energy of 75 GeV [101]. As a result, it features a significantly smaller aperture and absorbs a larger fraction of the beam energy.

4.2.3 First Quadrupole Triplet

The first quadrupole, located downstream of the collimator, experiences a total energy deposition of (20.12 ± 0.05) GeV per proton, leading to a peak temperature increase of $\Delta T = (2.48 \pm 0.05)$ K per spill, located 115 cm deep in the magnet. In the second quadrupole, the deposited energy amounts to (25.30 ± 0.08) GeV/PoT, resulting in a maximum ΔT of (1.53 ± 0.05) K, positioned near the end of Q2, precisely at 198 cm. Finally, the last quadrupole shows a peak temperature increase of (5.93 ± 0.10) K, occurring 10 cm deep in the magnet, with a total energy deposition of (55.66 ± 0.14) GeV per proton.

As shown in Figure 4.7, the hottest regions of the magnets tend to appear towards their downstream end, especially along the inner left side. This behaviour can be attributed to the beam beginning to scrape against the internal walls of the magnets, similarly to what was observed in the collimator. However, in this case, the presence of magnetic fields adds complexity. In particular, the third quadrupole displays a hotspot in its upstream section. Even with this effect, the temperature increase on all three quadrupoles remains negligible, especially compared to the Joule heating in the magnets, which is already compensated by a water cooling circuit.

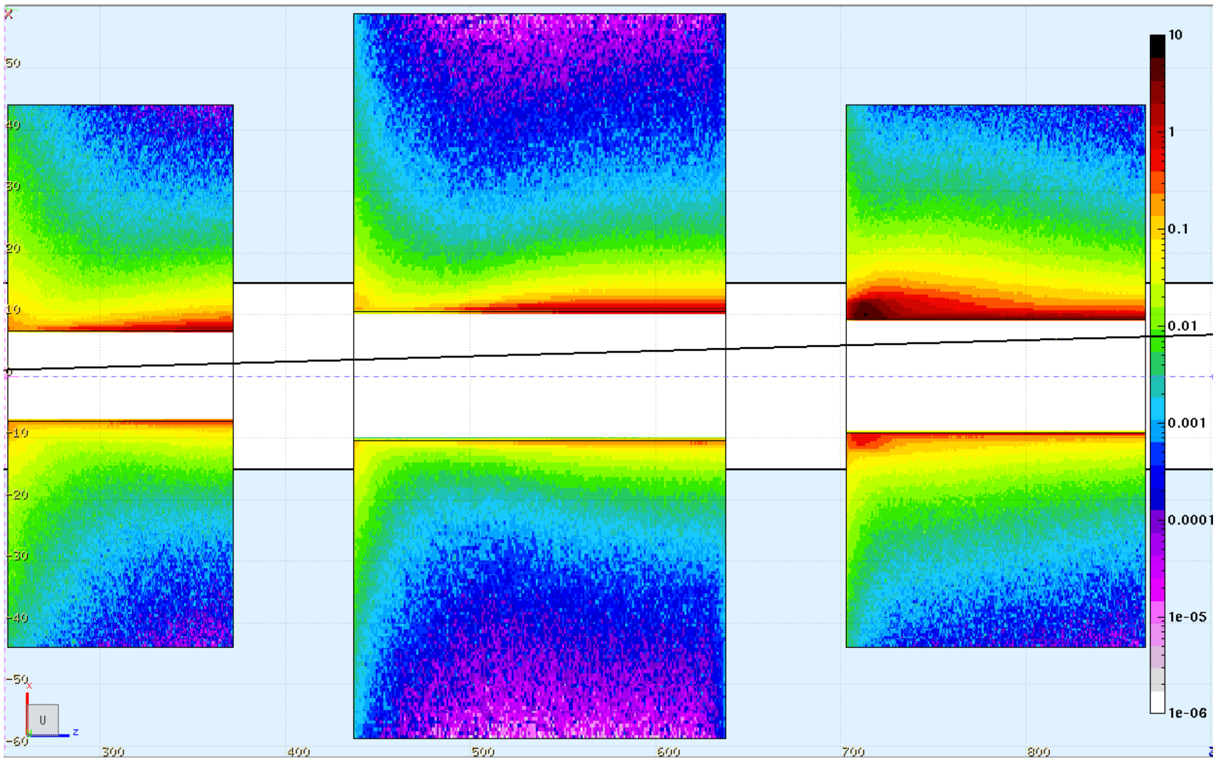

Figure 4.7: Top view of the temperature increase on the first quadrupole triplet. The black line represents the residual primary proton beam. The statistical error amounts to 1-5%.

4.2.4 Primary Hadron Dump

The dump (see Sec. 3.5), located at the end of the beamline, is responsible for absorbing the majority of the residual beam energy. The total energy deposition is (69.024 ± 0.250) GeV per proton, corresponding to a total absorbed power of (27.6 ± 0.1) kW, assuming a 4.8 seconds spill. Its modular structure, composed of alternating layers of aluminium, copper, and iron, is designed to optimize both energy absorption and thermal management. The maximum recorded temperature increase is $\Delta T = (12.12 \pm 0.25)$ K per spill, occurring in the first iron absorber block, approximately 65 cm from the front face of the dump.

Figure 4.8 shows the energy density distribution in the central zy plane. Although aluminium has a lower density than the other materials, its presence helps to spread the energy deposition more uniformly across the structure. Due to the differences in density and specific heat capacity among the materials, a uniform normalization cannot be computed and therefore only the energy density (and not the temperature increase) was evaluated in the dump.

As the energy deposition on the dump is entirely governed by the primary beam, it is strongly localised in the upstream region, particularly within the initial layers. The current configuration, based on an alternating sequence of aluminium, copper, and iron, proves effective in distributing the energy. The aluminium layer, which intercepts the beam first, plays a crucial role in diffusing the energy spatially. Beyond the central region, the number of interacting particles drops significantly, to the extent that some bins register negligible or even zero energy deposition. In those regions, when interactions do occur, the energy density reaches values on the order of $10^{-8} - 10^{-6}$ GeV/cm^3 per primary.

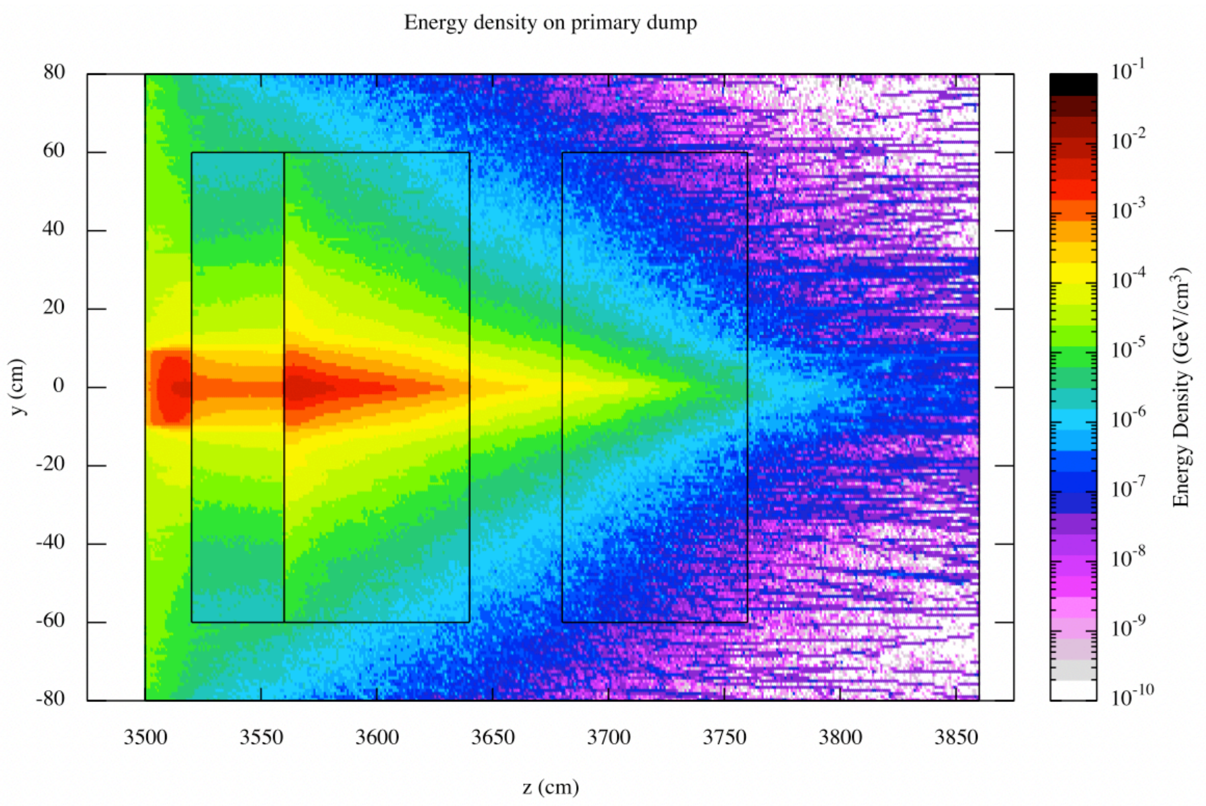

Figure 4.8: Side view of the energy density on the dump in the central cut. The energy deposition remains moderate, with localised peaks around 0.02 GeV/cm^3 per primary, well within the tolerances of the materials employed in the dump.

4.2.5 Energy Deposition in Downstream Components

Thermal effects on components located downstream of the first dipole are minimal. At this stage, the beam is already being shaped by the quadrupole magnets, resulting in a well-collimated secondary meson beam. Consequently, particle losses are significantly reduced, particularly after the momentum selection performed by the dipoles. Any energy deposition in these elements is therefore modest and generally confined to their frontal surfaces, where direct particle impacts occur.

A clear example of this behaviour (Fig. 4.9) is observed in the momentum-selecting dipoles. On average, each primary proton deposits (16.32 ± 0.05) GeV in this system, with approximately 99% of that energy absorbed by the first dipole alone. Similarly, the second quadrupole triplet receives less than 1 GeV per proton, while Q4 experiences a total deposited energy of (4.28 ± 0.03) GeV/PoT, primarily due to the fact that the left corner of this quadrupole is very close to the beam pipe.

The beam pipe, made of stainless steel with a 15 cm aperture and 2 mm wall thickness, runs continuously along the entire beamline. While the beam is designed to travel parallel to the pipe, some interactions with off-axis or scattered particles, particularly near the target, result in additional energy deposition. Over the full beamline, the beam pipe absorbs (13.90 ± 0.05) GeV/PoT.

The last major structure considered is the stainless-steel shielding surrounding the target. Although located in one of the most radiation-intensive regions of the beamline, it is not directly impacted by the primary beam. Instead, it is reached only by scattered particles, and the air gap between the beam and the shielding acts as an effective thermal insulator. As a result, the maximum temperature increase is limited to about $\Delta T \sim 0.10$ K, making thermal effects negligible. Nevertheless, due to its considerable size and position, the shielding absorbs a substantial amount of energy from secondary radiation, amounting to (40.24 ± 0.07) GeV per primary proton. This corresponds to a total absorbed power of (13.45 ± 0.02) kW, assuming a spill length of 4.8 s.

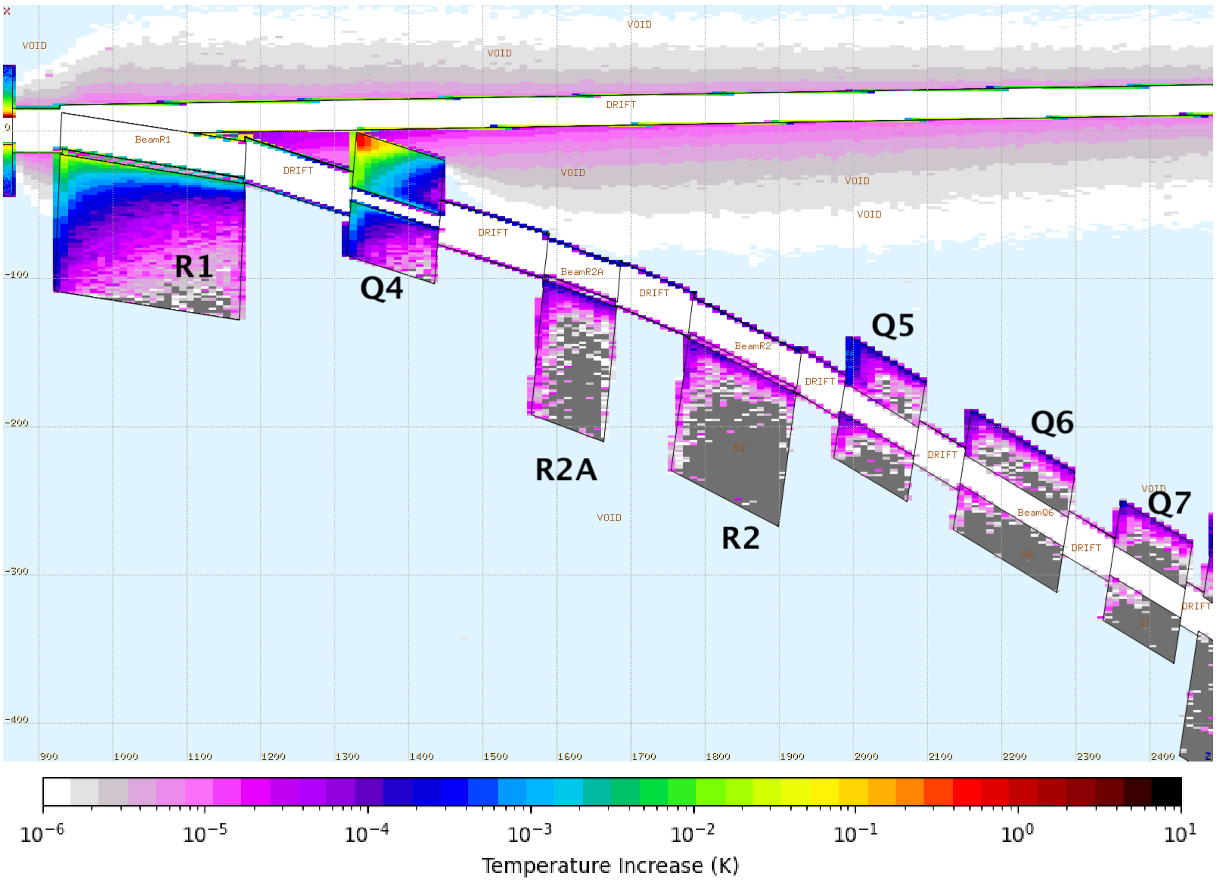

Figure 4.9: Temperature increase on downstream magnets. The secondary beam has already been shaped therefore the temperature increase on these components is negligible with the notable exception of the left corner of the fourth quadrupole (Q4) which, being close to the beam pipe, experience a modest temperature increase, on the $\mathcal{O}(1\text{ K})$.

In total, the combined energy deposition in all beamline components is 329 GeV per proton, representing approximately 82% of the primary beam energy.

4.3 Thermal Stresses on the Target

The evaluation of thermal stress within the target is essential to assess its structural integrity under the beam-induced heating. Figure 4.10 shows the stress distribution along the target's longitudinal axis, focusing on the central bin. This is the region where the approximation introduced in Sec. 4.1.2 is most applicable.

The results highlight a pronounced stress concentration near the beam entry point, where the temperature gradient is steepest. This outcome is expected due to the strongly non-uniform energy deposition, which induces sharp thermal gradients and, consequently, localized mechanical stress.

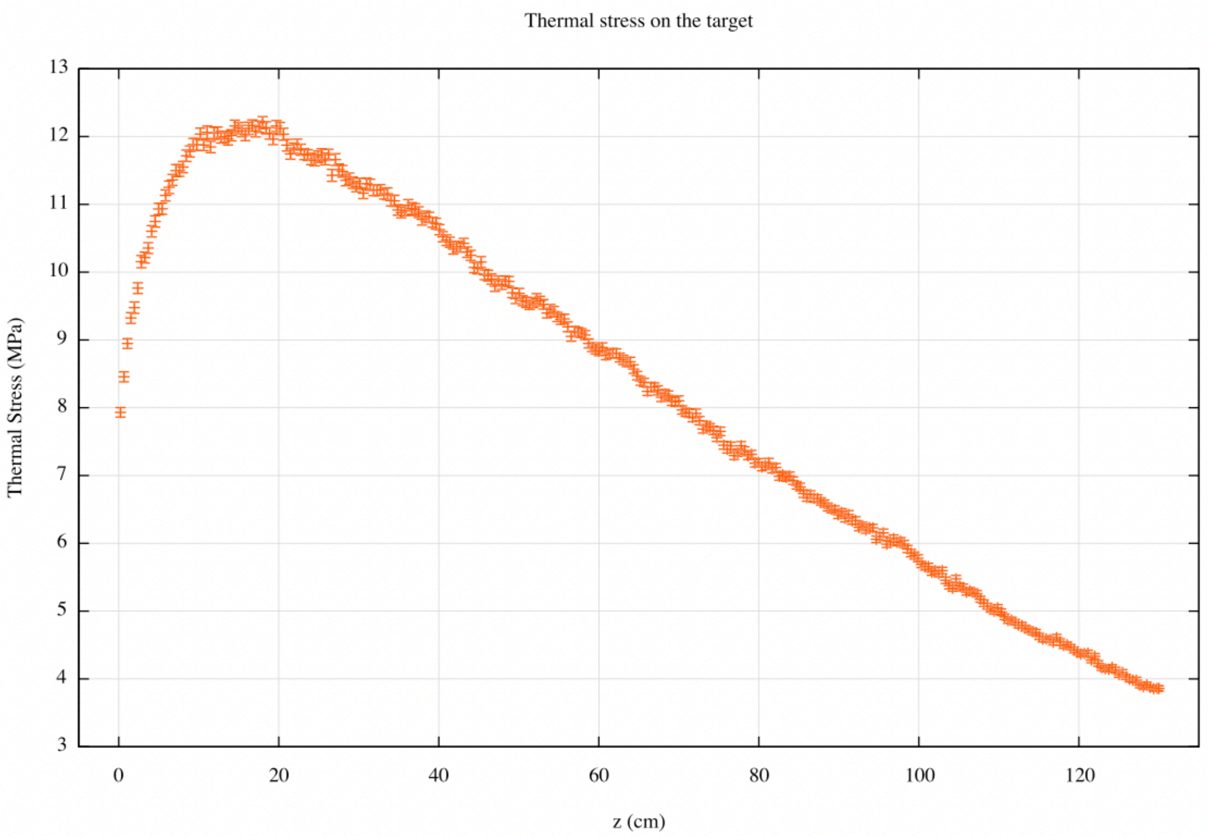

Figure 4.10: Thermal stress distribution in the centre of the target.

The maximum thermal stress is observed at a depth of 17.8 cm, reaching a value of (12.21 ± 0.09) MPa. Figure 4.11 shows the transverse section of the target at this depth. Similarly to what was observed for the temperature distribution, the stress spreads radially outward from the beam axis. Notably, even though the stress is significant near the centre, it drops by nearly two orders of magnitude within 3 mm from the axis.

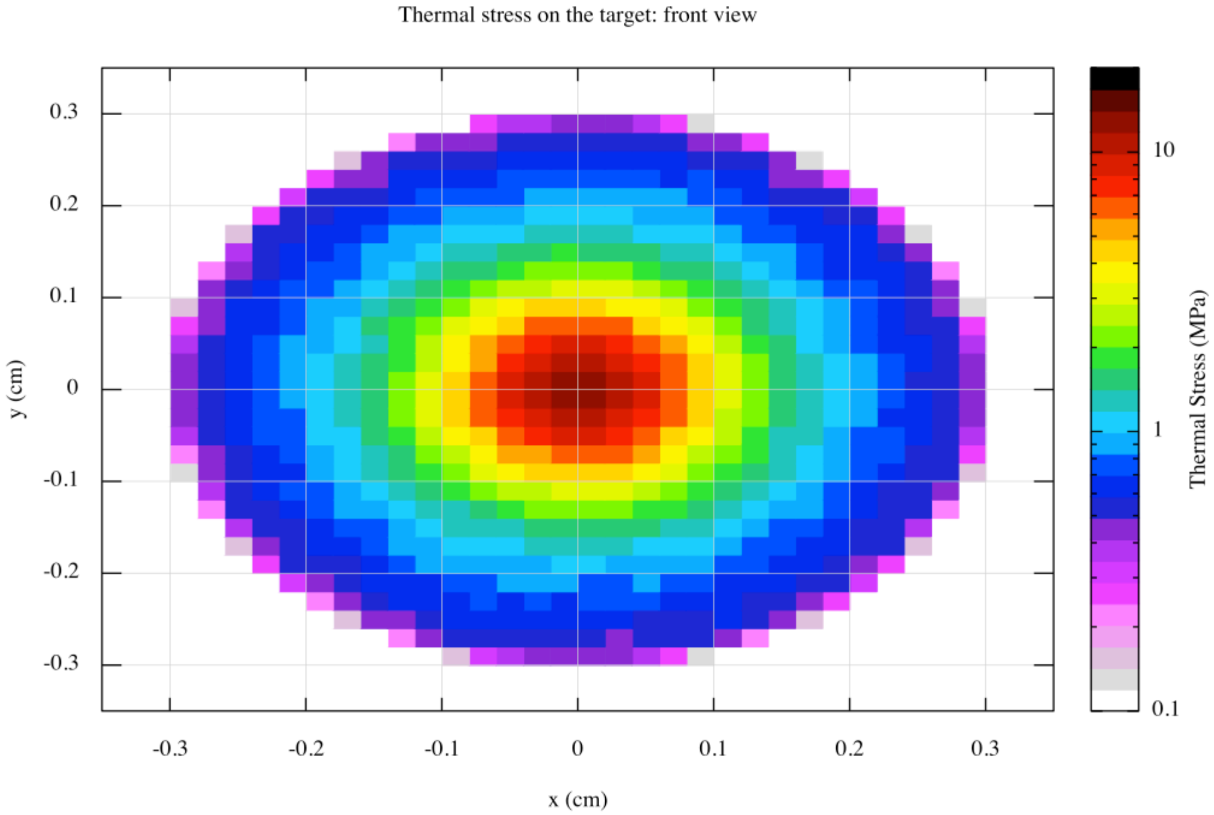

Figure 4.11: Thermal stress distribution in the hottest slice, located 17.8 cm deep in the target.

The relatively modest temperature increase in most components of the beamline allows for a simplification of the thermal stress calculation. Since the temperature remains within a range where material properties do not vary significantly, quantities such as thermal conductivity, specific heat, and Young's modulus can be treated as constant. This assumption enables faster simulations without compromising the accuracy of the results, as the materials remain within their linear thermo-mechanical regimes.

The peak thermal stress of about 12.2 MPa is well below the failure thresholds of graphite. Unlike metals, graphite does not exhibit a distinct yield point under tensile loading due to its brittle nature, it fails abruptly once its tensile strength is surpassed. Under compressive stress, however, graphite behaves quite differently, remaining elastic up to approximately 50 MPa (Fig. 4.12). This value is significantly higher than the peak thermal stress observed in the target.

The wide gap between the operational thermal stress and the compressive strength of graphite provides a comfortable safety margin. This confirms that the target will remain structurally sound during beam operation. Graphite's ability to withstand such thermal and mechanical loads is one of the key reasons behind its choice as the target material, ensuring both reliability and longevity under harsh irradiation conditions.

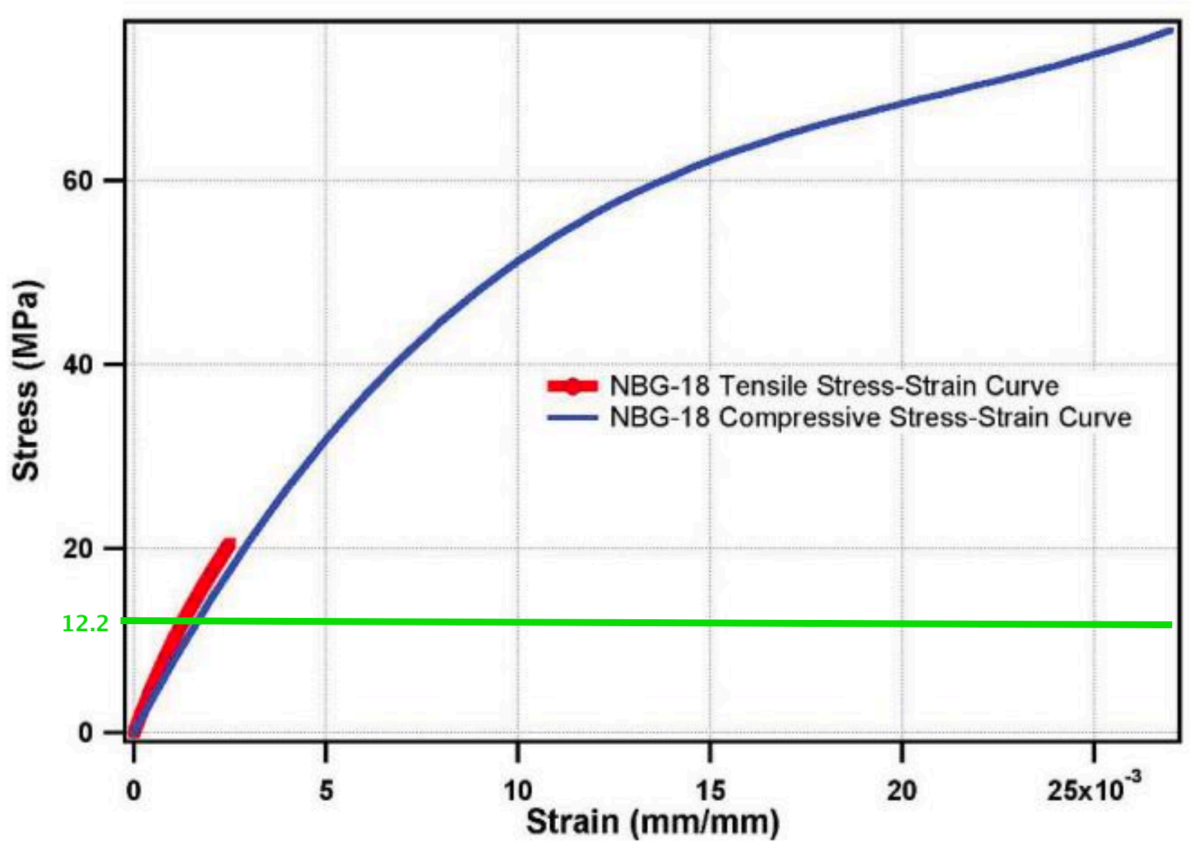

Figure 4.12: Stress–strain curve for nuclear-grade graphite. In green, the maximum thermal stress experienced by the target. Even in the case of tensile load, the target remains well within its elastic limit, with a safety margin of 80-90%. Figure adapted from [112].

Chapter 5

Radio-protection assessment of the beamline

This chapter presents the radioprotection assessment of the nuSCOPE beamline, with a focus on shielding design, dose deposition on critical components, and the characterization of particle fields relevant to safety and detector performance. The study evaluates both prompt and residual equivalent doses to ensure compliance with personnel safety requirements and to assess the survivability of radiation-sensitive electronics, such as the silicon pixel trackers. Detailed FLUKA simulations quantify energy losses across the beamline, identify hot spots, and assess their radiological impact. Special attention is given to the fluence and energy spectra of highly penetrating particles, muons and neutrons, at strategic locations, including the primary proton dump, decay tunnel, and hadron dump, to validate shielding adequacy and maintain a low-background environment for the neutrino detector. Results confirm that the designed shielding effectively reduces radiation to acceptable levels, while highlighting localized areas where minor improvements could further optimize protection.

5.1 Shielding Design

The radioprotection analysis of the entire beamline is a fundamental step in the development of a facility such as nuSCOPE. In particular, the estimation of both prompt and residual equivalent doses is crucial for evaluating the biological risk to personnel during operations and determining which areas can be accessed during beam time. Furthermore, the readout electronics, especially the silicon tracker, has a maximum radiation tolerance beyond which it may suffer irreversible damage. It is therefore important to assess whether the flux of secondary particles exceeds this threshold.

A key aspect of this study is the distinction between the *absorbed dose*, measured in grays (Gy), and the *equivalent dose* ($H^*(10)$), measured in Sievert (Sv). While the absorbed dose quantifies the energy deposited per unit mass, the equivalent dose accounts for the biological effect of different radiation types by applying a radiation weighting factor. This distinction is central to radioprotection, as various particles, such as photons, neutrons, and charged hadrons, interact differently with biological tissue. The gray thus represents a purely physical quantity, while the sievert provides a biologically relevant metric for assessing radiation risks and defining safety thresholds.

A central element of any radioprotection strategy is the shielding design. As the name implies, shielding protects biological and electronic systems from harmful radiation. The optimisation of shielding is a complex process, strongly dependent on the specifics of the experimental setup. However, some general design principles exist. In high-energy physics facilities, a layered, "onion-like" approach is typically adopted.

The first layer generally consists of a dense and inexpensive material with a short nuclear interaction length. A common choice is cast iron, composed of roughly 95% iron by mass, with a nuclear interaction length of 16.77 cm [11]. This layer serves to slow down high-energy, deeply penetrating hadrons by initiating hadronic showers and producing lower-energy secondaries. In the nuSCOPE design, hadronic shielding is applied only in the hottest regions of the beamline, namely around the transfer line and the beam pipe transporting the residual primary protons to the dump. Importantly, shielding is only installed on the right side, where the experimental cavern allows personnel access. On the left side, the beamline runs close to the cavern wall, which inherently provides shielding via the surrounding ground. Where present, the cast iron shielding reaches a thickness of 40 cm.

The second shielding layer is intended to stop most of the secondary particles generated in the cast iron. For this purpose, concrete is typically used due to its low cost and suitability for building large structures. Being significantly less dense than cast iron, concrete requires a greater thickness to achieve the same attenuation. In designing the virtual shielding in the FLUKA simulation, standard CERN concrete blocks were used wherever possible to reduce costs through material reuse. On the side of the transfer line, concrete shielding reaches up to 120 cm, while the top and bottom sections reach 80 cm.

The entire beamline is enclosed in a composite sarcophagus of iron and concrete, which, at the most shielded locations, corresponds to 5.2 nuclear interaction lengths (λ_0) and 33.15 radiation lengths (X_0). This level of shielding ensures that even components directly hit by the primary beam, which may become highly radioactive, are isolated to the extent that only a minimal fraction of high-energy secondaries escape the enclosed region.

The exact spatial configuration of the shielding used in the FLUKA simulation of the nuSCOPE beamline is shown in Figure 3.12.

5.2 Prompt Dose Rate

The first Radiation Protection (RP) study presented in this thesis concerns the estimation of the prompt dose rate. The simulation was carried out assuming the standard nuSCOPE beamline configuration: a 400 GeV proton beam, slowly extracted from the SPS accelerator, impinges on a 130 cm-long graphite target.

Since FLUKA provides dose results in an unconventional unit (pSv/PoT), the simulation output must be properly normalized to yield a more interpretable quantity. The assumed irradiation scenario corresponds to a total of $2 \cdot 10^{18}$ Protons on Target (PoT) delivered over a calendar year. However, the CERN accelerator complex does not operate year-round: physics runs are interrupted during the winter months to allow for maintenance and minor upgrades, a period referred to as the Year-End Technical Stop (YETS) [77]. As a consequence, all facilities relying on the SPS, including nuSCOPE, are assumed to operate for approximately 200 days per year.

The final results are expressed in terms of dose rate, in µSv/h. The normalization factor N is therefore:

$$N = \frac{2 \cdot 10^{18}\ \text{PoT/year}}{200\ \text{d} \times 24\ \text{h} \times 60\ \text{min} \times 60\ \text{s}} \times 3600 \times 10^{-6} = 4.14 \cdot 10^{8}\ \text{PoT/h} \tag{5.1}$$

Figure 5.1 shows the prompt dose rate in the transfer line, projected onto the plane containing the beam axis. The red contour highlights the 100 mSv/h threshold, corresponding to the boundary of prohibited areas at CERN. The shielding appears to be effective: the tunnel remains accessible during operation, at least in emergency situations. In the vicinity of the target station, the dose rate reaches approximately $\mathcal{O}(50\ \mu\text{Sv/h})$, which is relatively high, but comparable to values observed in similar facilities. At the entrance of the decay tunnel, the dose rate is on the order of $\mathcal{O}(5\ \mu\text{Sv/h})$.

It is important to emphasize that these areas are not expected to be accessible during routine beamline operation and should be properly isolated from any accessible zones. A possible location for a separation door could be the beginning of the decay tunnel, allowing access under controlled or supervised conditions. A formal classification of the access conditions must be performed by the CERN Radiation Protection group (HSE-RP) and falls outside the scope of this study.

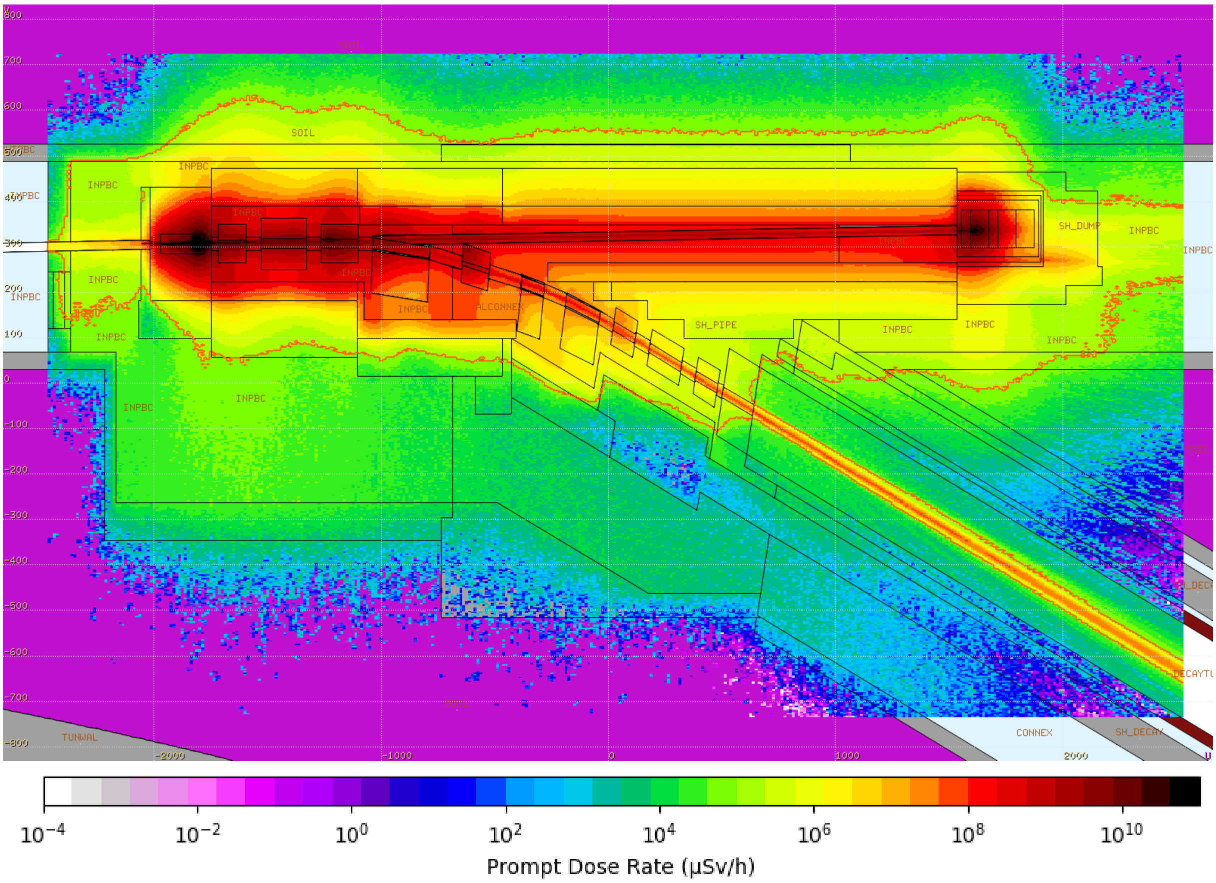

Figure 5.1: Top view of the prompt dose rate on the transfer line on the beam axis plane. The red contour represents the 100 mSv/h dose level, marking the limit for prohibited areas at CERN. The statistical uncertainty is low in high-dose regions inside the shielding ($\sim 1\%$), increasing with distance from the beamline. In the tunnel, behind the shielding, it fluctuates between 10–30%.

Figure 5.2 shows the prompt dose rate in the decay tunnel and at the neutrino detector location. Here, the 100 mSv/h contour is marked in green. The focusing system appears effective at confining the beam before it enters the decay tunnel: only a small number of stray particles – mostly leptons, which nuSCOPE aims to monitor – reach the tunnel walls. The hadron dump is very effective in reducing the dose behind it, that will eventually reach the neutrino detector, therefore reducing the background signal expected in it. The prompt dose rate registered in the neutrino detector is $\mathcal{O}\left(10^{-8}\ \mu\text{Sv/h}\right)$, which is a completely negligible value.

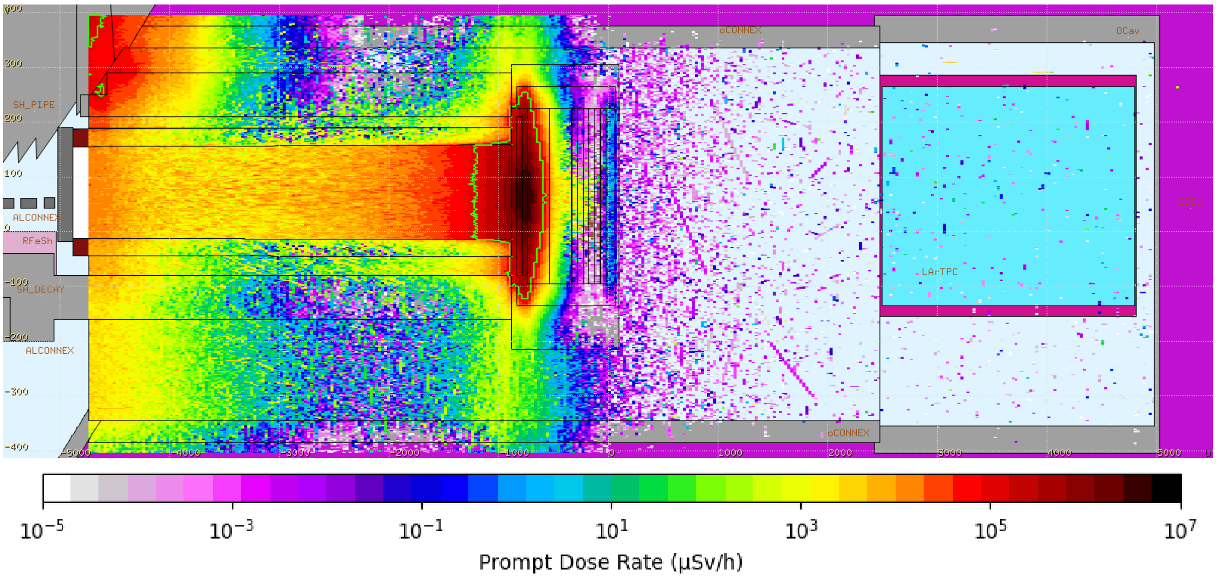

Figure 5.2: Top view of the prompt dose rate on the decay tunnel and neutrino detector on the beam axis plane. The green contour represent the 100 mSv/h dose level, marking the limit for prohibited areas at CERN. The statistical uncertainty in this case is higher since fewer particles reach this region; for the hottest regions (i.e. the front face of the hadron dump) the error is $\mathcal{O}(1\%)$ and it is less than 40% for the entire length of the decay tunnel.

5.3 Residual Dose Rate

5.3.1 Dose on the Beamline - Overview

Following the study on prompt dose rate, the residual dose has been studied. The irradiation profile is the same as the last study with the facility running for 5 years for 200 days a year; thus, the beam intensity is equal to $1.157 \cdot 10^{11}$ p/s. Since the study focuses on calculating the equivalent dose, which by its very nature is a significant quantity on sufficiently large time scales, the temporal microstructure of the beam is of no interest and can be neglected.

In order to cover a large time interval, several cooling time has been chosen to measure the residual dose on the beamline, namely: one hour, four hours, one day, one week, one month, six months, one year and three years. In the next set of plots, one can see an overview of the equivalent dose (figure 5.3) from one hour up to six months.

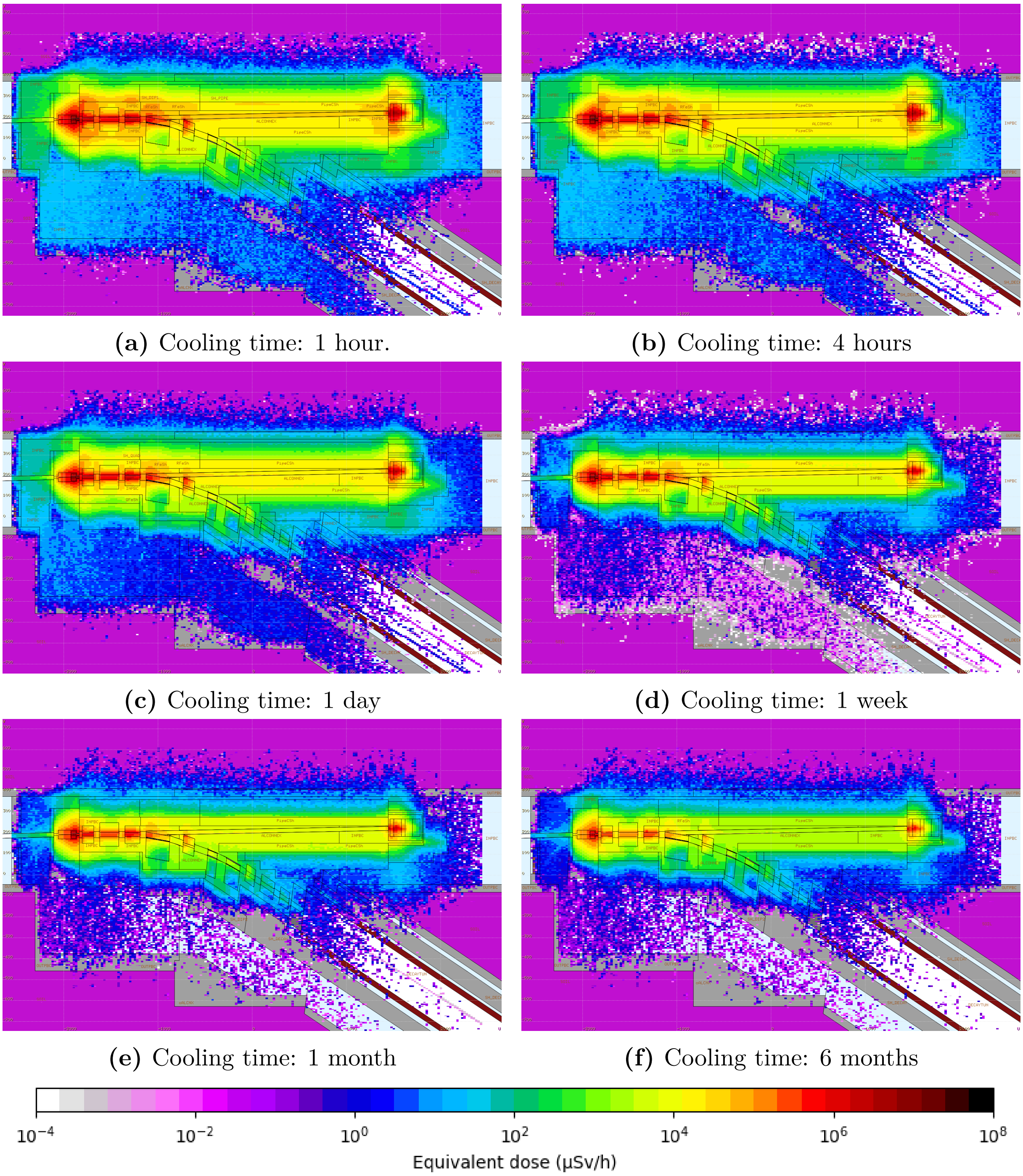

(a) Cooling time: 1 hour.

(b) Cooling time: 4 hours

(c) Cooling time: 1 day

(d) Cooling time: 1 week

(e) Cooling time: 1 month

(f) Cooling time: 6 months

Figure 5.3: Equivalent dose scored at different times in the nuSCOPE beamline. As one can imagine, the hottest point in the whole beamline is the target; other hot spots are the dump, the first three quadrupoles and the junction between the primary beam pipe and the secondary one. The statistical error increase as the beamline cools down since more and more radioactive nuclei have decayed. In the regions inside the shielding, the error fluctuates between 0.5-5%, while behind the shielding rises up to 50%.

5.3.2 Equivalent Dose Rate at Key Locations Along the Beamline

This section presents an analysis of the time evolution of the ambient dose equivalent rate, $H^*(10)$, at selected strategic points along the beamline. The aim is to evaluate how radiation levels vary over time in areas expected to be critical for operational safety and maintenance planning. Seven key locations were identified for this study:

1. inside the target station, 10 cm to the left, between the target and the collimator;
2. in front of the first quadrupole, 10 cm to the right and 50 cm above the beam axis;
3. 5 cm to the left of the beam pipe transporting primary protons to the dump, at a distance of 5 m from the dump;
4. 20 cm behind the shielding of the primary dump, inside the TT61 tunnel;
5. 1 m behind the target station shielding, in the alcove of TT61;
6. 1 m behind the beamline shielding, just beyond the tracker plane in Q4;
7. At the entrance of the decay tunnel.

These locations offer valuable information both on the radiation environment close to the target and at more distant points along the beamline, where access may be required after beam operations.

To contextualize the results, the measured dose rates are compared with CERN's radiological area classification thresholds. The main limits are:

- **Red Area**: 100 mSv/h – access strictly prohibited due to severe radiation hazards;
- **Orange Area**: 2 mSv/h – restricted access under controlled conditions;
- **Simple Controlled Area**: 50 µSv/h;
- **Supervised Area**: 15 µSv/h – no dosimeter required;
- **Non-Designated Area**: 2.5 µSv/h – no radiological classification required, provided the area is not continuously occupied.

By analysing how long the dose rate remains above these thresholds, it is possible to estimate when the areas become accessible for different types of interventions, supporting the planning of maintenance activities and radiological protection strategies.

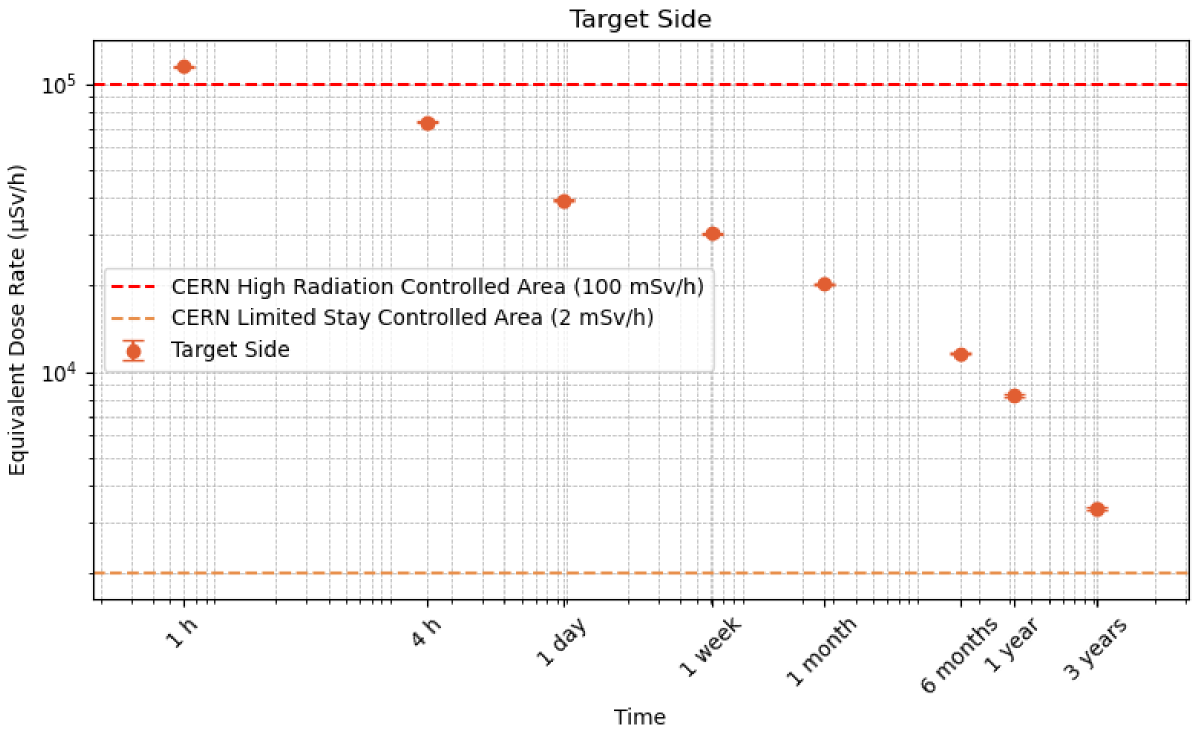

Figure 5.4: Time evolution of the equivalent dose rate near the target.

Figure 5.4 shows the dose rate evolution near the target. As expected, the radiation levels remain significant even after a substantial cooling period. However, despite the high energy deposition from the 400 GeV primary protons in a small volume, the area becomes technically accessible for emergency interventions after just a few hours.

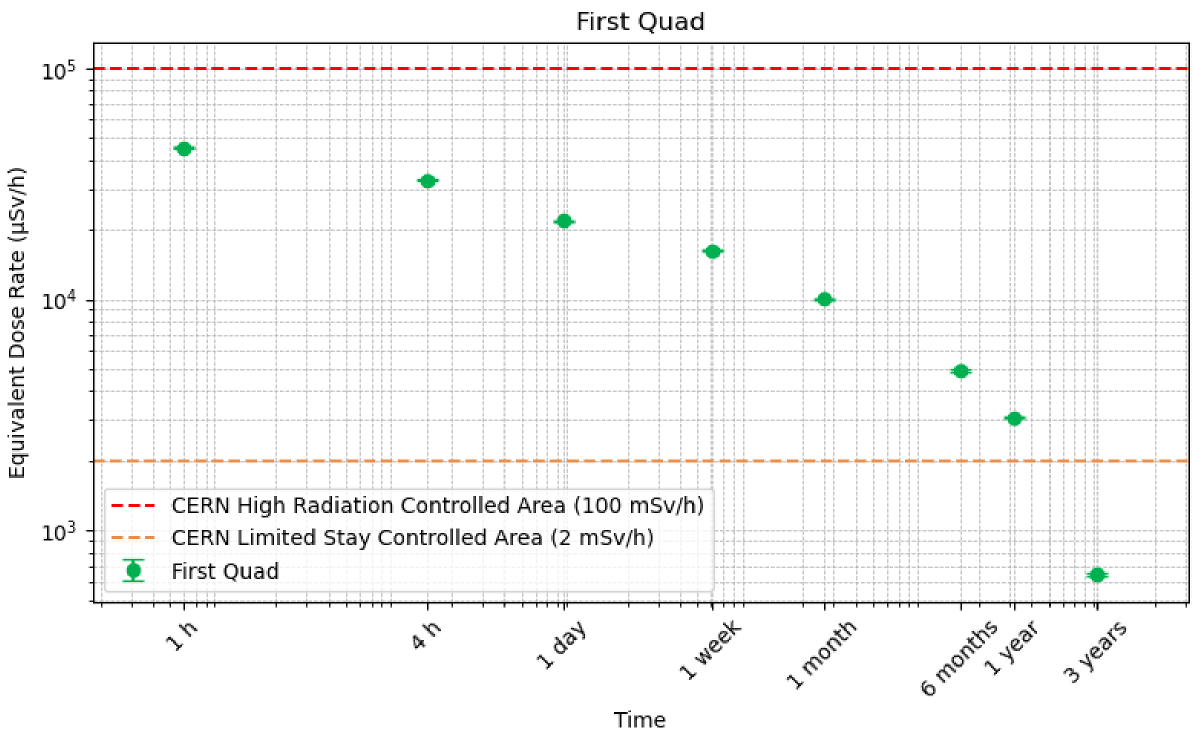

Figure 5.5: Time evolution of the equivalent dose in front of the first quadrupole.

A similar trend is observed in front of the first quadrupole magnet (Fig. 5.5), although with lower dose rates. This is due to the shielding provided by the collimator and the absence of direct beam interaction with the magnet itself.

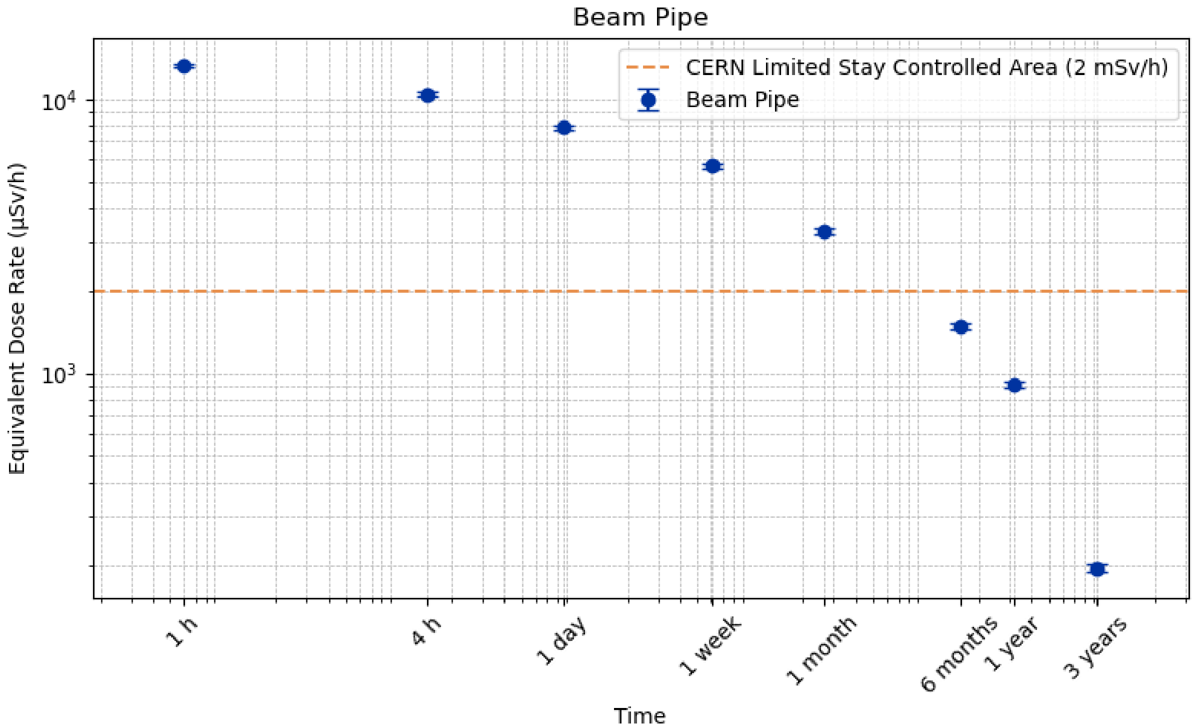

Figure 5.6: Time evolution of the $H^*(10)$ dose near the beam pipe.

Another area of interest is the vicinity of the beam pipe transporting protons to the dump, shown in Fig. 5.6. This location is particularly relevant for future dismantling operations. After nuSCOPE ceases operation, the recovery of valuable shielding components could be considered. However, the radiation level remains above 200 mSv/h even after three years of cooling. This would result in a category B worker reaching the annual limit of 6 mSv in approximately 30 h. A longer cool-down period would therefore be required for safe intervention, but a precise estimation lies outside the scope of this study.

Figure 5.7 presents the dose evolution behind the shielding of the primary proton dump. Already after one hour of cooling, radiation levels are moderate, and after one week they fall below the Simple Controlled Area limit of 50 µSv/h.

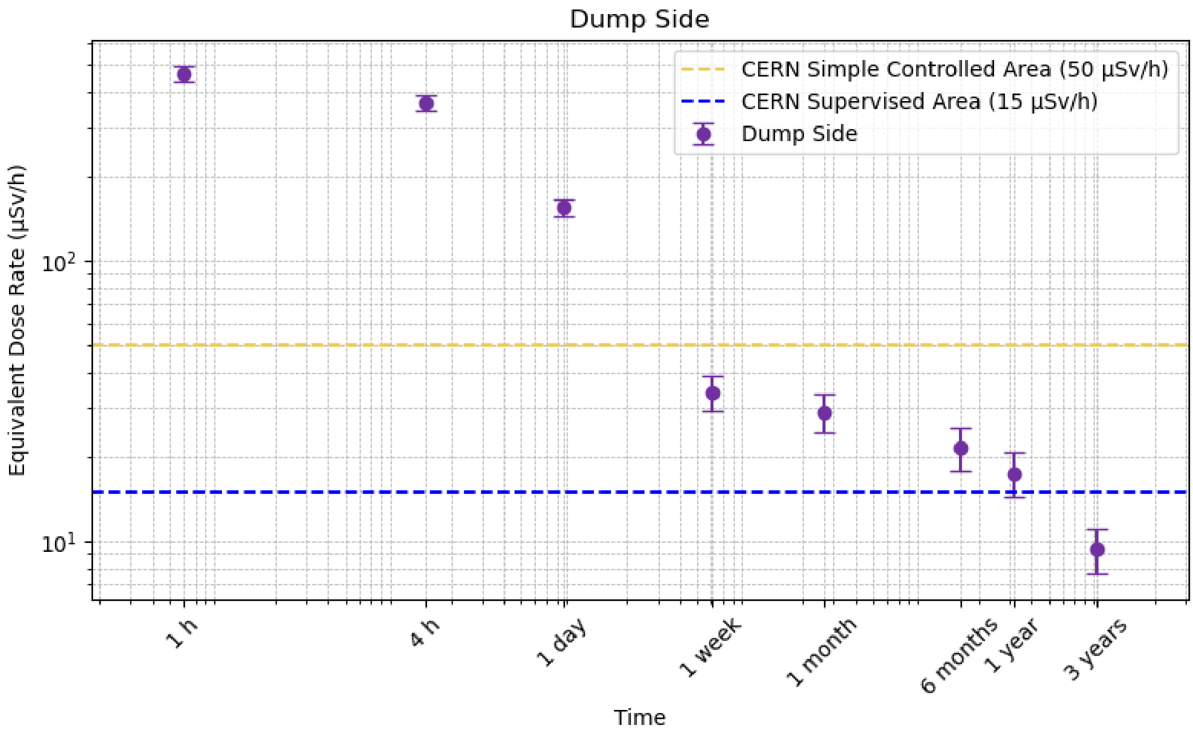

Figure 5.7: Time evolution of the equivalent dose rate near the primary proton dump.

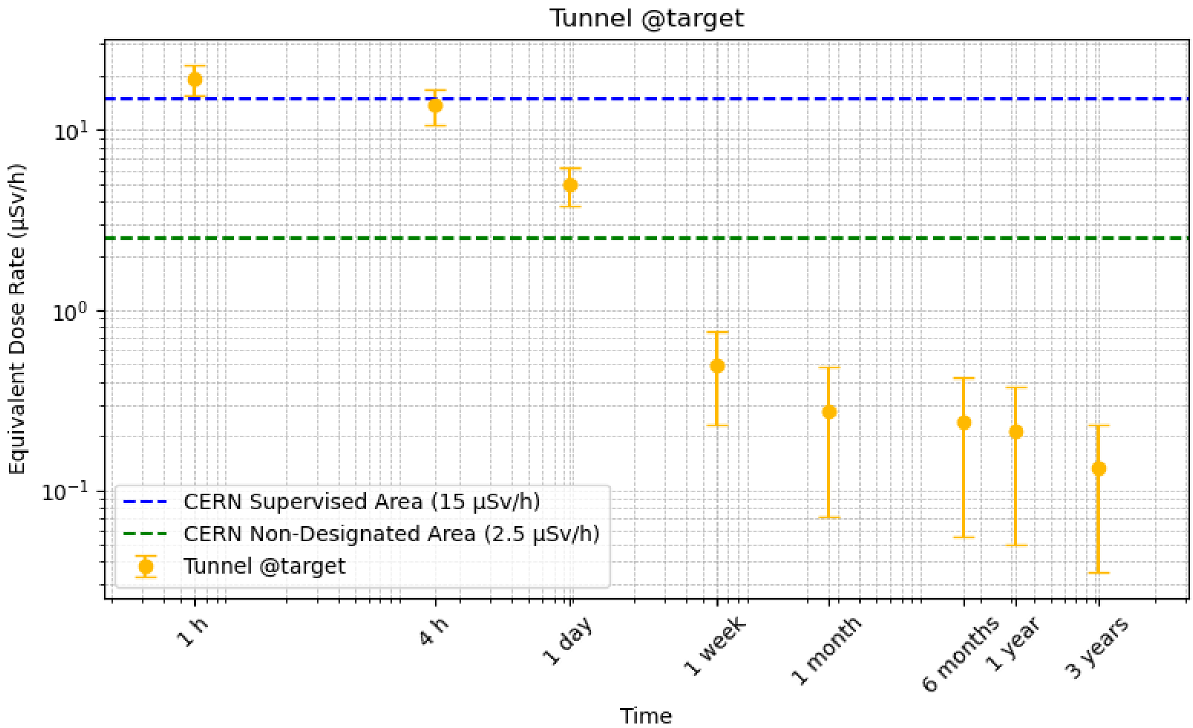

Figure 5.8: Time evolution of the equivalent dose in the tunnel at the target station.

Other selected areas are located within the tunnel near the beamline. Among them, the highest radiation levels are observed in the alcove behind the target station shielding (Fig. 5.8). Even in this case, the dose rate is consistently low, and below the 2.5 µSv/h threshold for Non-Designated Areas just after a week of cooling.

A notable downside of such low radiation environments is the slow convergence of Monte Carlo simulations. For cooling times exceeding one week, the statistical uncertainties become particularly relevant, as visible in Fig. 5.9. A dedicated simulation with at least ten times higher statistics would be needed for a robust analysis, but this would require several months of CPU time and falls beyond the time constraints of this work.

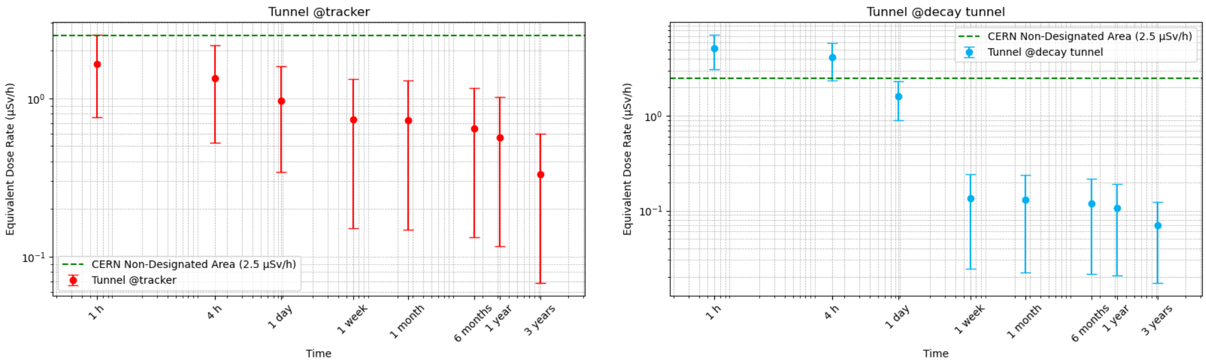

(a) $H^*(10)$ in the tunnel near the tracker. **(b)** $H^*(10)$ at the entrance of the decay tunnel.

Figure 5.9: Time evolution of the equivalent dose rate in the tunnel near (a) the pixel tracker at Q4 and (b) the beginning of the decay tunnel. The large statistical uncertainties are due to the very low radiation levels, which hinder simulation convergence.

5.4 Doses on trackers

One of the most important detectors in the nuSCOPE beamline is the silicon pixel tracker system, which is pivotal for the implementation of the tagging technique. In particular, the first tracker plane is the most exposed to radiation, and it is therefore important to evaluate the radiation field it can withstand during the entire operational period of the experiment. Two quantities have been studied for the first tracker: the dose per spill in Gray and the 1 MeV neutron silicon equivalent fluence.

5.4.1 Dose in Gray

This study has been performed assuming a spill intensity of 10^{13} PoT. FLUKA scores doses in an unusual unit, GeV/(g · PoT); to convert these values to Gy, the results must be multiplied by $1.6022 \cdot 10^{-7}$ and by the number of primary protons expected on target.

Figure 5.10 shows the total dose on the pixel tracker. The peak dose occurs at the centre of the tracker plane, with a value of (22.80 ± 0.63) Gy, which should be tolerable by the pixel detector [76].

From the figure, the contour of the circular beampipe can be clearly distinguished. On the right side, the background dose is higher due to the proximity of the primary beampipe, which is highly radioactive and, at this point in the beamline, not yet shielded. In the future, it may be necessary to extend the shielding to fully isolate the tracker from the primary beampipe.

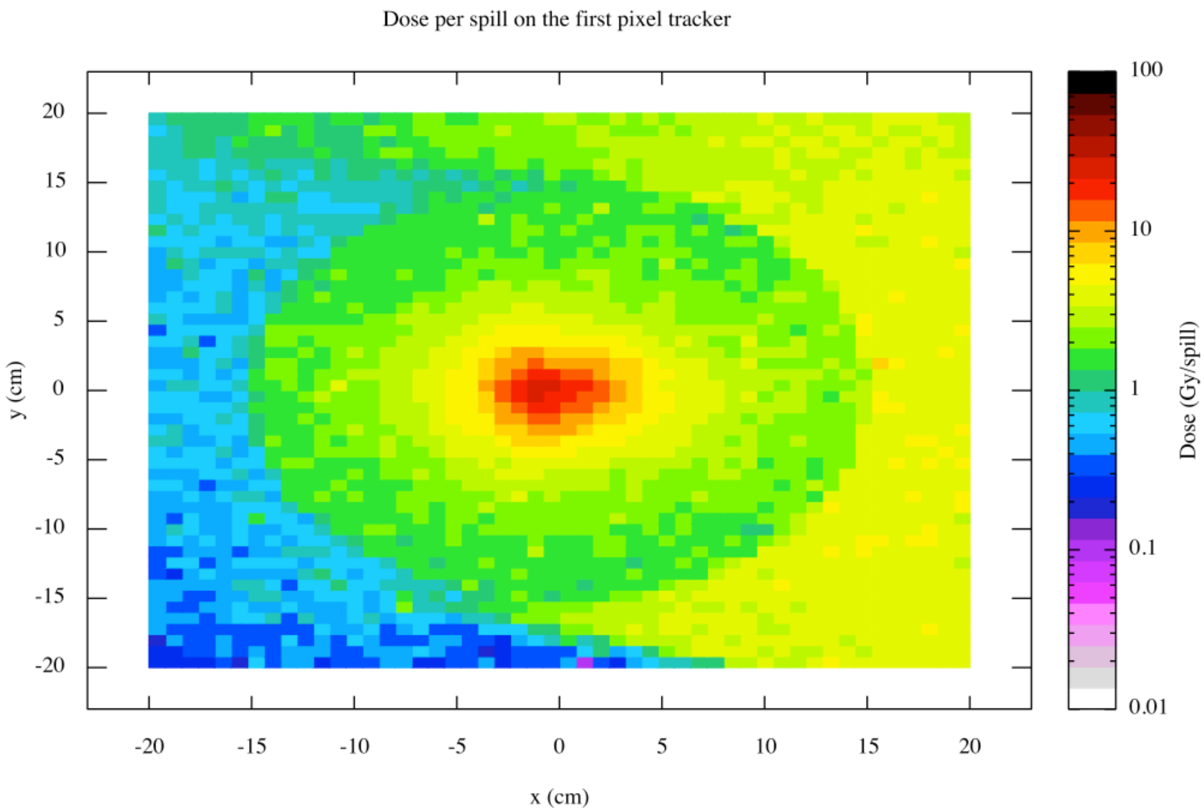

Figure 5.10: Dose per spill deposited in the first silicon tracker, assuming a spill intensity of 10^{13} PoT.

5.4.2 1 MeV Neutron Equivalent Fluence

Fast neutrons, as well as other particle species, can damage silicon detectors mainly by displacing atoms from their lattice sites into interstitial positions, producing vacancy–interstitial pairs, the so-called *Frenkel pairs*.

Neutrons with sufficiently high energy can cause *primary displacements*, i.e. the direct removal of an atom from its lattice site. The displaced atom can, in turn, produce secondary displacements, leading to a cascade effect [113].

The displacement damage induced by neutrons is described by the damage function $D(E)$, which accounts for both the cross-section for displacing silicon atoms and the energy released in creating displacements:

$$D(E) = \sum_k \sigma_k(E) \int f_k(E, E_R) P(E_R) \mathrm{d}E_R \tag{5.2}$$

where E is the incident neutron energy, $\sigma_k(E)$ is the cross-section of the k-th reaction, $f_k(E, E_R)$ is the probability that a recoil energy E_R is produced, and $P(E_R)$ is the partition function, i.e. the fraction of recoil energy deposited in displacements.

Using the damage function $D(E)$, the energy density E_{dis}, the energy per cm^3 deposited through atomic displacements, is given by:

$$E_{\text{dis}} = N \int_{E_{\text{min}}} D(E)\phi(E)\text{d}E \tag{5.3}$$

where N is the atomic density of bulk silicon, E_{min} is the lowest neutron kinetic energy capable of producing a displacement, and $\phi(E)$ is the neutron spectral fluence.

In radiation protection contexts, it is often useful to normalise displacement damage from different particle types to the effect caused by a 1 MeV neutron, via a hardness parameter $\kappa(E)$. This leads to the 1 MeV neutron equivalent fluence:

$$\Phi_{\text{eq.}}^{1\text{ MeV}} = \kappa \int_{E_{\text{min}}} \phi(E)\text{d}E = \int_{E_{\text{min}}} \frac{D(E)}{D(1\text{ MeV})}\phi(E)\text{d}E \tag{5.4}$$

This quantity provides a standardised measure of displacement damage for different energies and particle species.

Since displacement damage accumulates over time, every detector has a maximum total fluence it can withstand. The following results are therefore normalised to $1.4 \cdot 10^{19}$ PoT, corresponding to the total number of protons on target expected during the five-year nuSCOPE data-taking period.

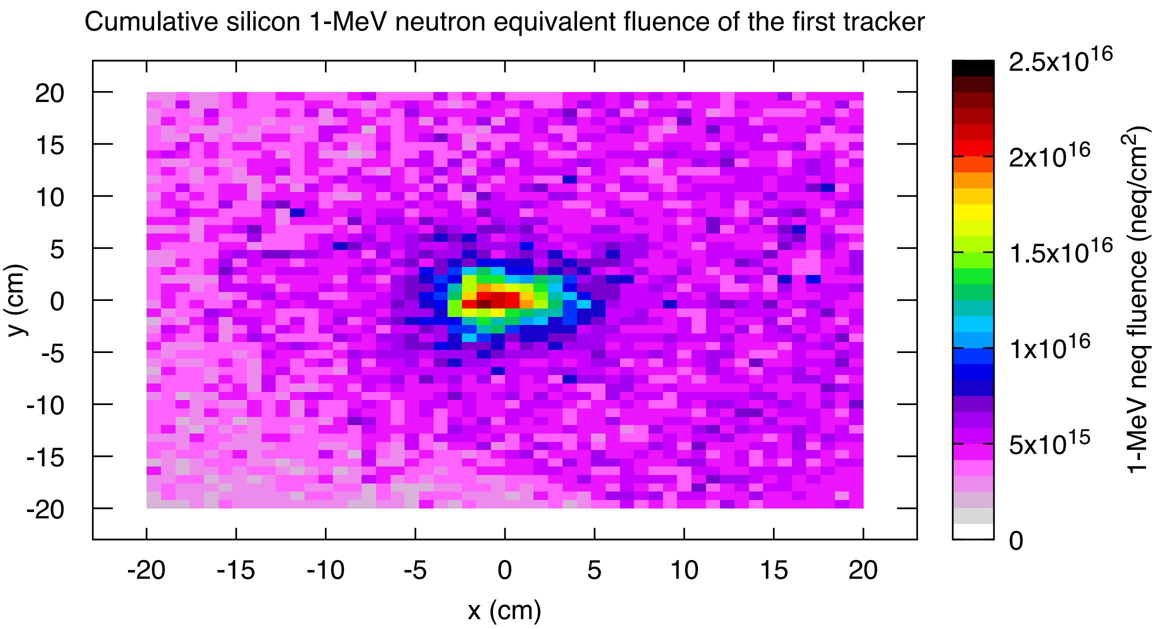

Figure 5.11: Cumulative silicon 1 MeV neutron equivalent fluence on the first tracker, normalised to the total proton-on-target budget expected during the five-year nuSCOPE operation.

Figure 5.11 shows the 1 MeV neutron equivalent fluence on the first tracker. The hotspot is, once again, located at the centre of the tracker plane, where the beam is most collimated and therefore most intense. The peak neutron fluence is on the order of $2 \cdot 10^{16}$ $n_{\mathrm{eq}}/\mathrm{cm}^2$, which lies within the operational limits of the LHCb VELO upgrade technology that the nuSCOPE collaboration plans to adopt [114].

5.5 Penetrating Particle Fluence

In the context of radioprotection, beyond the simple evaluation of the absorbed dose, it is essential to determine which particles are responsible for the radiation field. In particular, it is crucial to study the most penetrating particles, as they are the most challenging to shield against. In a high-energy physics experiment, there are two dominant contributions to the penetrating component of the radiation field: muons and neutrons.

5.5.1 Muons

Muons are charged leptons and, at relativistic energies, behave as minimum ionizing particles (MIPs), meaning they lose the smallest possible amount of energy per unit path length in matter. A MIP loses approximately 2 $\mathrm{MeV}/(\mathrm{g} \cdot \mathrm{cm}^2)$, so stopping a high-energy muon typically requires several meters of shielding material, depending on its density and composition.

5.5.1.1 Primary Proton Dump

The location in the beamline where the most energetic muons are found is directly downstream of the primary proton dump. In this region, high-energy muons originate from two main processes: interactions between primary protons and the target, producing muons outside the momentum bite of the transfer line, and secondary interactions of the primary beam within the dump itself.

Figure 5.12 shows the energy spectrum of muons emerging from the iron cover of the dump, integrated over the solid angle. The spectrum exhibits a peak around 100 MeV; a muon of this energy is stopped by approximately 25 cm of concrete[1]. Downstream of the dump, an additional 240 cm of concrete shielding is present, which suppresses the low-energy part of the spectrum below 1 GeV. As a result, only muons in the high-energy tail of the spectrum survive into the tunnel. These surviving muons have already lost part of their energy in the shielding and are therefore partially slowed down. The muon yield at the primary dump amounts to $(2.548 \pm 0.010) \cdot 10^{-2}$ μ/PoT.

[1] The minimum ionization in concrete is 3.935 MeV/cm [11], hence a MIP with 100 MeV will be stopped by $\frac{100\ \mathrm{MeV}}{3.935\ \mathrm{MeV/cm}} = 25.4$ cm of concrete.

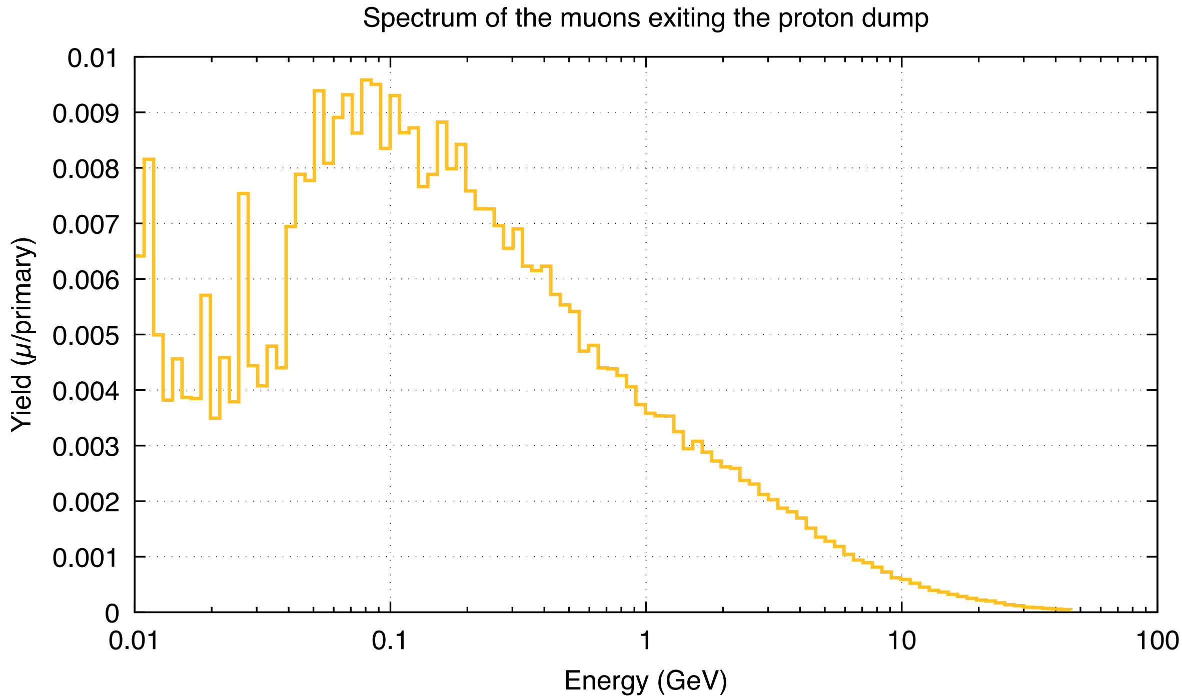

Figure 5.12: Energy spectrum of muons emerging from the primary proton dump.

Figure 5.13 presents the simulated muon fluence per primary proton in the TT61 tunnel. The dump reduces the muon fluence by at least two orders of magnitude. A significant fraction of the remaining muons interact with the tunnel walls due to deflections induced by multiple scattering in the shielding, combined with the fact that the primary beam pipe follows the small tilt of the target. Nevertheless, a small number of muons reach the basement of Building 804 at the end of the TT61 tunnel, indicating that further shielding may be required to reduce this residual flux.

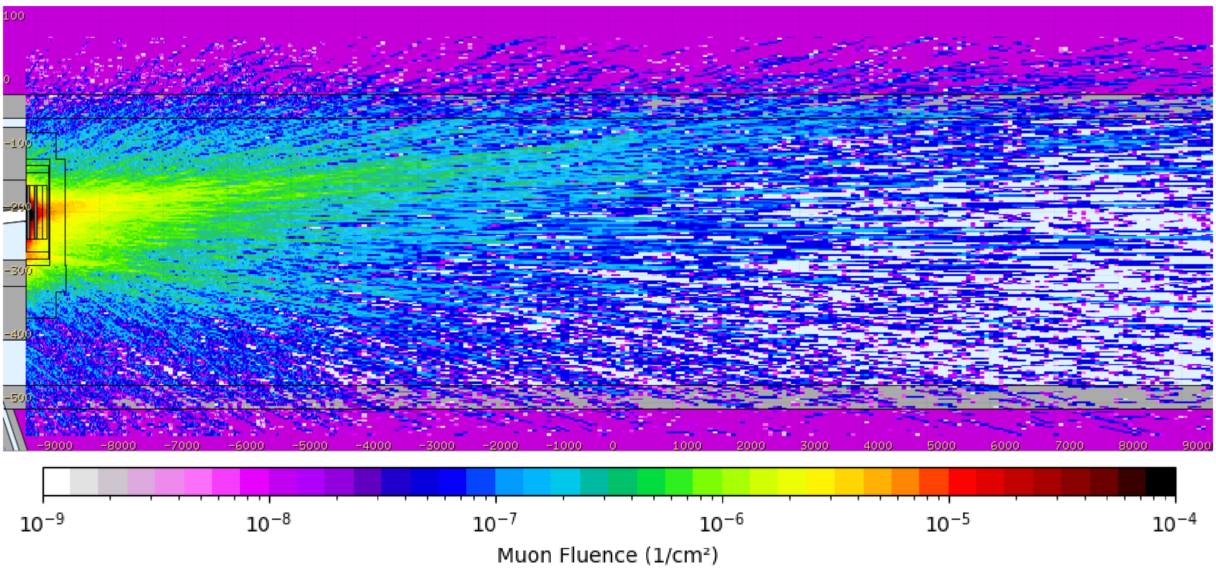

Figure 5.13: Muon fluence in the TT61 tunnel downstream of the primary proton dump.

5.5.1.2 Decay Tunnel and Hadron Dump

Besides the primary proton dump, another critical location for muon studies is the exit of the decay tunnel, particularly downstream of the hadron dump. This analysis serves two purposes: firstly, to characterise the energy spectrum and fluence of the muons that will be intercepted by the instrumented dump, and secondly, to validate the dump's design dimensions. Ensuring complete absorption of all muons emerging from the decay tunnel is essential, as the neutrino detector must operate in an environment with minimal background to reliably identify genuine neutrino interactions. Any residual beamline muons reaching the detector would compromise the effectiveness of the tagging technique.

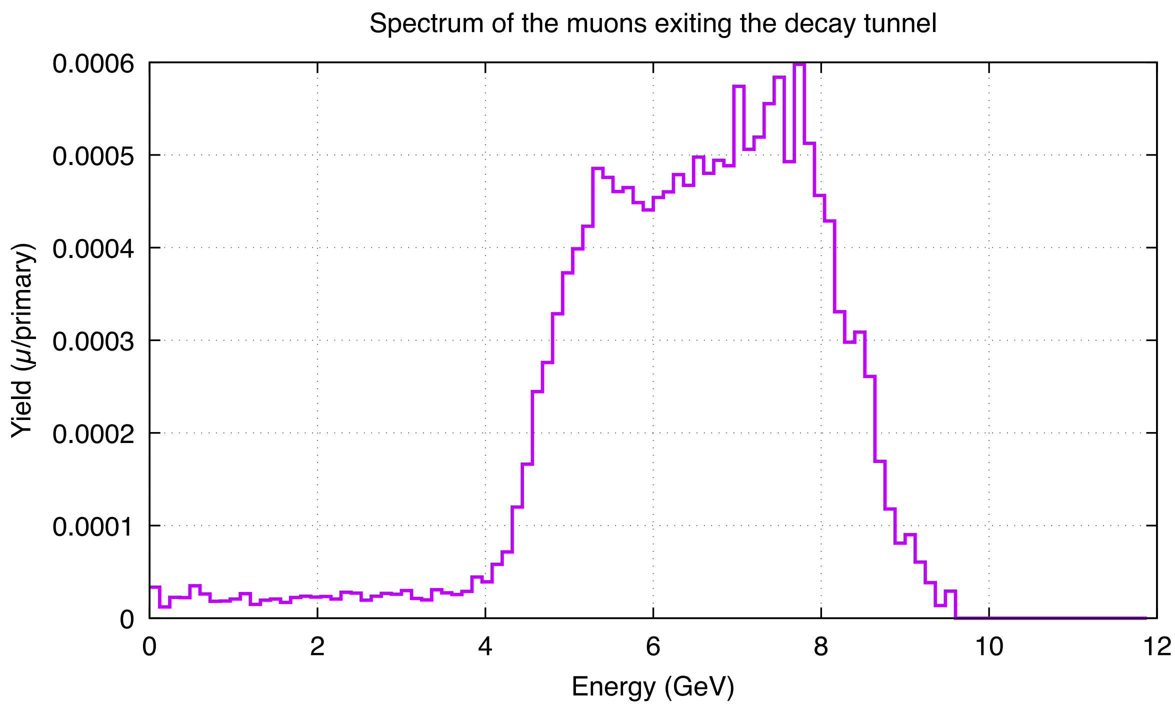

Figure 5.14: Energy spectrum of the muons emerging from the decay tunnel.

Figure 5.14 shows the muon energy spectrum at the decay tunnel exit. Compared to the broader and less structured spectrum observed at the proton dump (Fig.5.12), the muon spectrum at the decay tunnel exit exhibits a sharper and more pronounced peak. This is a direct consequence of the momentum selection applied by the beamline's magnetic elements, which effectively narrows the energy spread of the transmitted muons. Muons in this location originate either directly from primary proton interactions in the target and get transported and momentum selected by the transfer line or from in-flight decays of pions and kaons. Consequently, the maximum muon momentum at the tunnel exit corresponds to 8.5 GeV, with an additional 10% momentum bite, a feature clearly visible in the spectrum. The total number of muons registered at the end of the decay tunnel is equal to $(2.031 \pm 0.022) \cdot 10^{-3}$ μ/PoT.

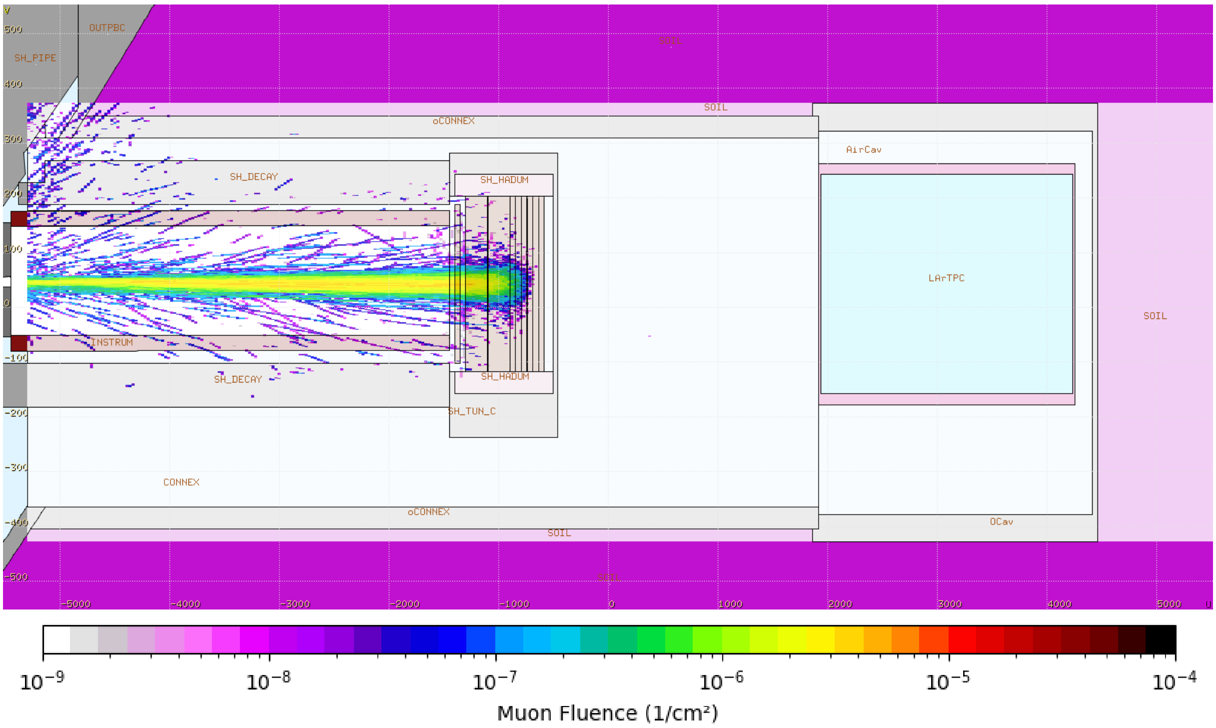

Figure 5.15: Muon fluence in the decay tunnel and neutrino detector.

As shown in Fig. 5.15, the muon beam remains well collimated along the entire 40-m instrumented tunnel. Deviations from the beam axis are rare and mostly due to muons produced in kaon three-body decays, in particular the $K_{\mu 3}$ decay mode, which has a branching ratio of 3.3%. The focussed muon beam is then absorbed in the instrumented hadron dump. The results clearly show that most muons are stopped within the first two absorber blocks and that the dump's dimensions are adequate, as no muons are detected downstream. The total material budget of the nuSCOPE dump amounts to 7.5 m of iron. Considering that a minimum ionizing particle, such as a muon, loses on average 1.14 GeV/m when traversing iron [11], the dump is in principle capable of fully absorbing MIPs with energies up to about 8.5 GeV. This guarantees that the neutrino detector operates in a background-free environment for optimal performance.

5.5.2 Neutrons

Neutrons are neutral hadrons composed of one up quark and two down quarks. Owing to their lack of electric charge, they do not lose energy via the Bethe–Bloch mechanism, as they cannot interact electromagnetically with the atomic electrons that constitute matter. Instead, neutrons lose energy exclusively through direct interactions with nuclei, whose dimensions are several orders of magnitude smaller than those of atoms. As a result, their typical mean free path in matter is on the order of a few centimetres.

5.5.2.1 Beamline

The first evaluation of neutron fluence was carried out considering the entire beamline. Figure 5.16 shows the results normalized per primary proton. The spatial distribution follows the same trend observed for the dose map (Fig. 5.1): regions inside the shielding exhibit high radiation levels, while the shielding itself effectively reduces the neutron fluence in the tunnel to values of the order of 10^{-7} n/(cm^2 · PoT).

A noticeable feature is the neutron leakage observed on the right side of the primary proton dump. This occurs because the dump is not perfectly sealed by the surrounding concrete shielding, allowing neutrons to escape through a small gap. Nevertheless, the downstream concrete layer at the end of the dump is thick enough to fully absorb this leakage. While not a critical safety concern, this issue will be addressed in future beamline design iterations.

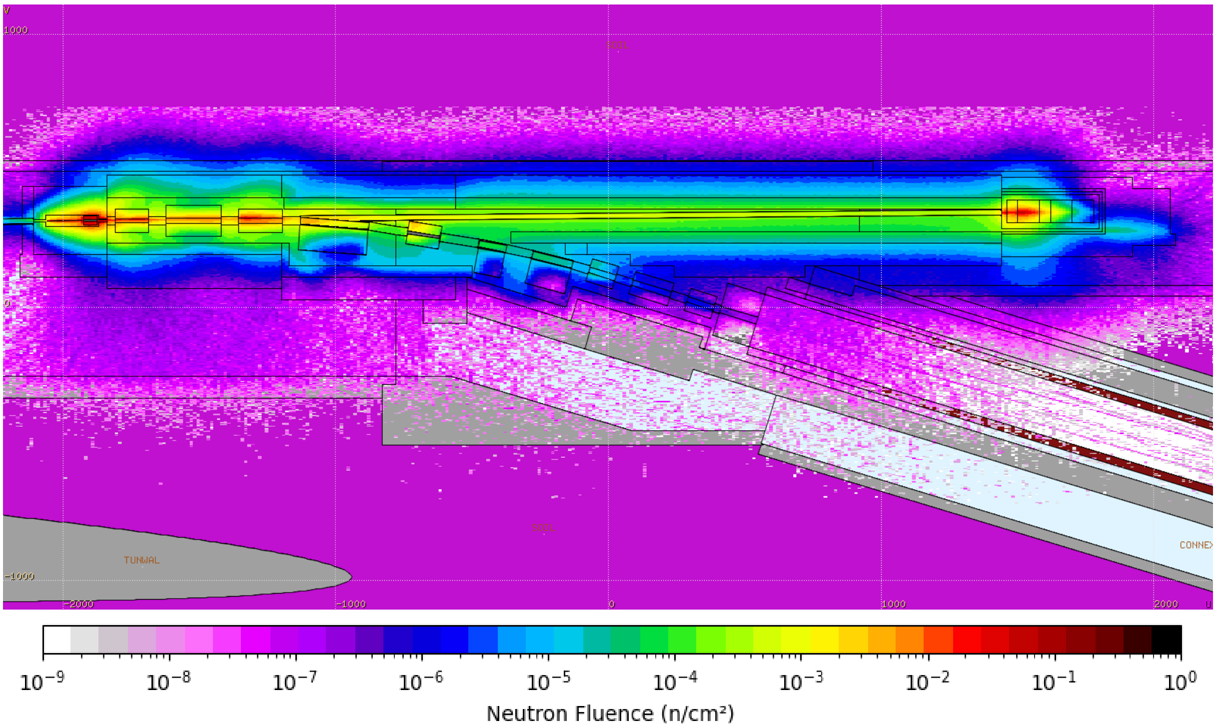

Figure 5.16: Neutron fluence in the nuSCOPE beamline.

Figure 5.17 presents the 1 MeV neutron equivalent fluence integrated over the expected 5-year proton budget for nuSCOPE. The distribution is broadly similar to that of Fig. 5.16, with one significant difference: the presence of the secondary meson beam. Since the 1 MeV neutron equivalent fluence accounts for contributions from all particle types, the beampipe transporting the secondary beam also appears as a hotspot, unlike in the pure neutron fluence map. In Fig. 5.16, very few neutrons reach the second bend, as their neutrality prevents deflection by the magnetic fields.

The neutron energy spectrum at the exit of the primary dump is shown in Fig. 5.18. It approximately follows the v_n^{-1} cross-section scaling law for neutrons [115], with several resonance features in the range $1 - 1000$ keV. The high yield of thermal neutrons arises from moderation processes: high-energy neutrons, which have small absorption cross-sections, predominantly lose energy through multiple elastic scatterings until they reach thermal energies, where the absorption cross-section becomes large enough for efficient capture. The total neutron yield from the primary beam dump is (99.83 ± 0.25) n/PoT.

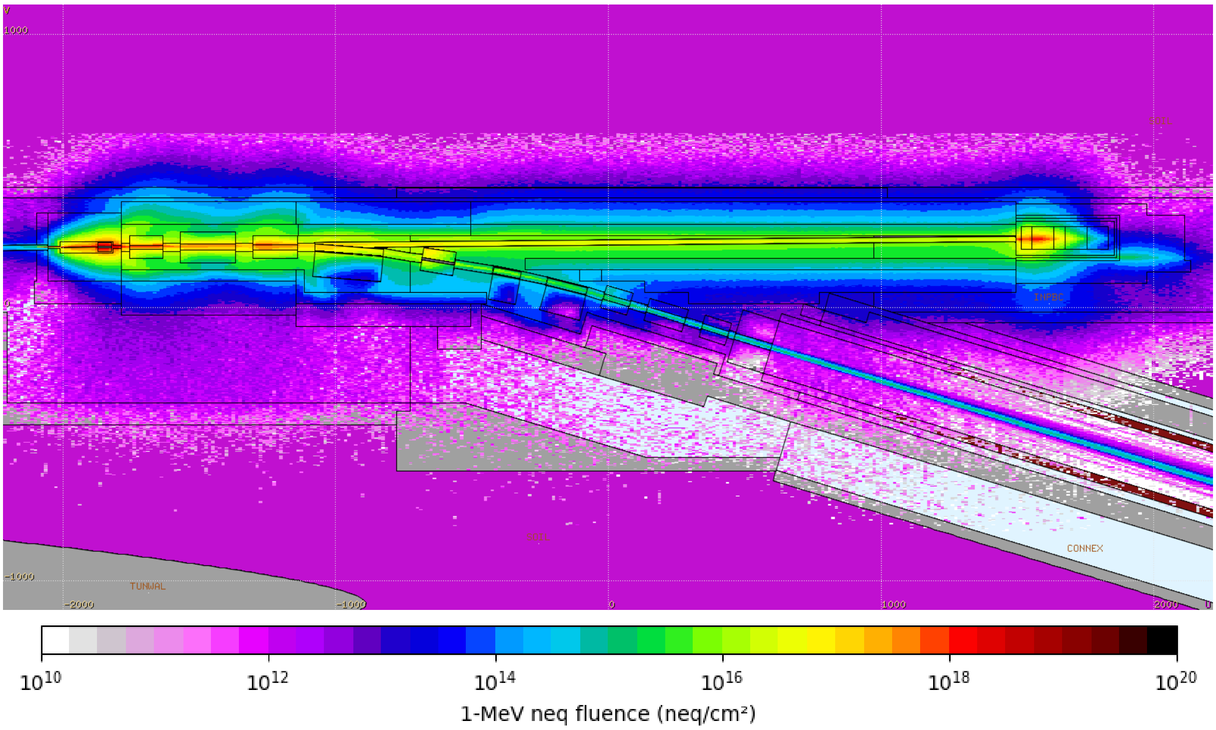

Figure 5.17: 1 MeV neutron equivalent fluence in the nuSCOPE beamline, assuming a total proton budget of $1.4 \cdot 10^{19}$ PoT.

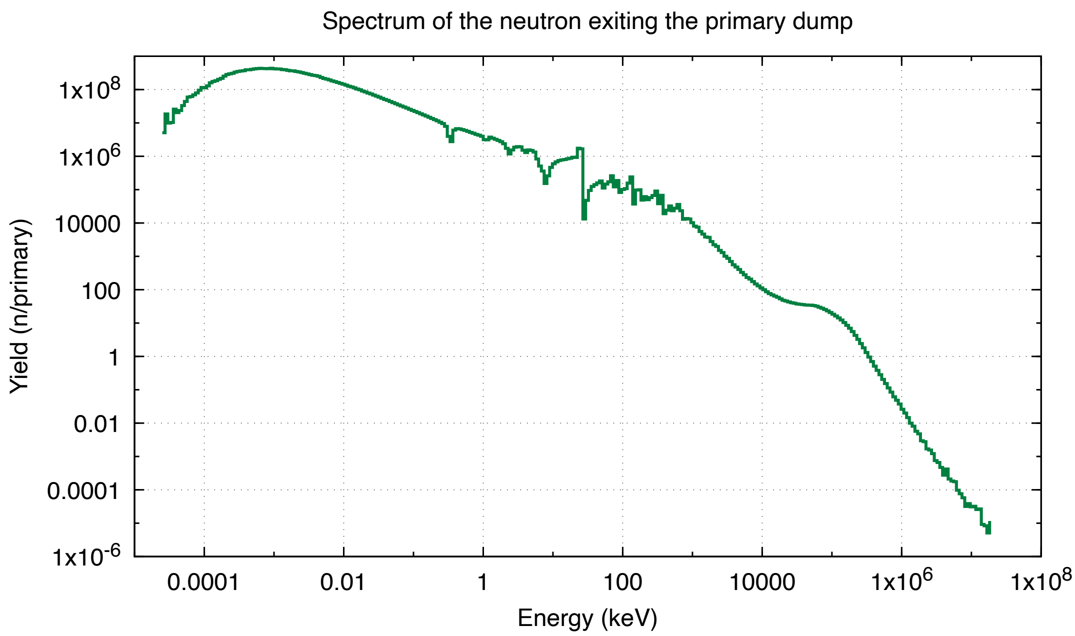

Figure 5.18: Energy spectrum of neutrons emerging from the primary dump iron cover.

5.5.2.2 Decay Tunnel

Another key location for assessing neutron fluence, both to evaluate potential exposure risks for facility personnel and to determine the shielding requirements, is the decay tunnel. Figure 5.19 shows the neutron fluence per primary proton in this region. Only a small number of neutrons are present in the decay tunnel, as their neutrality prevents them from being focused by the transfer line. The majority of the neutrons is produced when the secondary beam is absorbed in the hadron dump, originating from nuclear interactions between pions, kaons, muons, and the nuclei of the absorber material. These newly generated neutrons are, however, effectively contained within the dump, resulting in negligible external leakage.

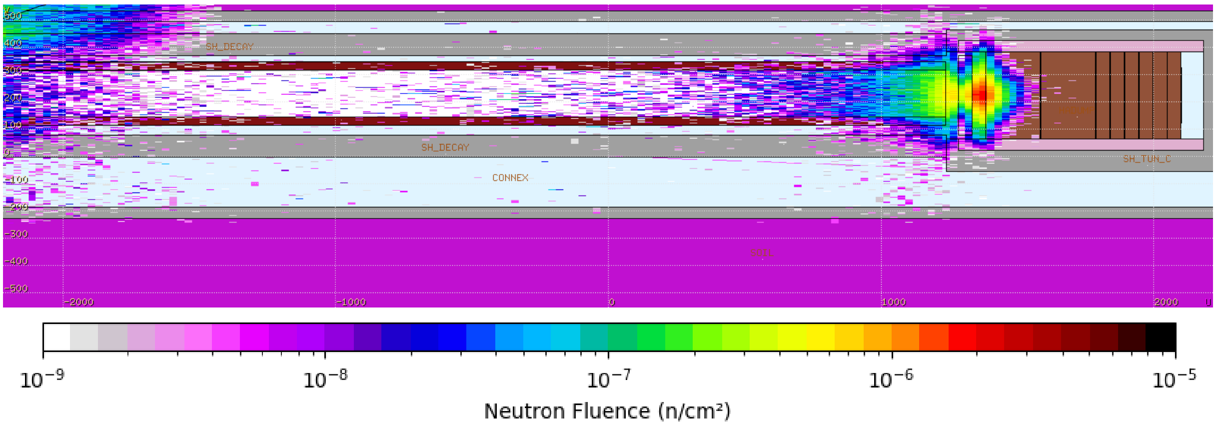

Figure 5.19: Neutron fluence in the decay tunnel. Since FLUKA does not distinguish between prompt and secondary particles when scoring fluence, the plot reports the total neutron contribution. The dominant component arises from secondary production, mainly generated by the interactions of the meson beam with the hadron dump.

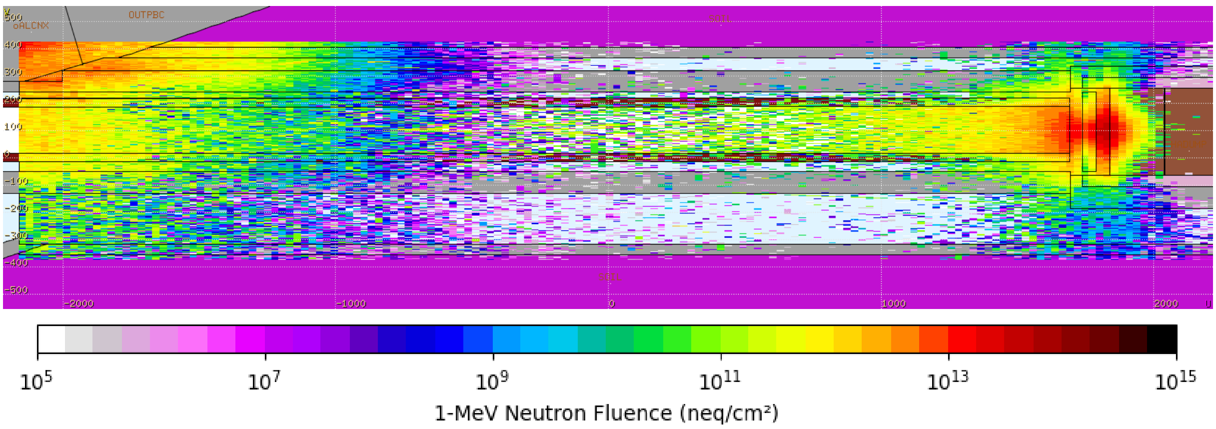

Figure 5.20: 1 MeV neutron equivalent fluence in the decay tunnel, assuming a total proton budget of $1.4 \cdot 10^{19}$ PoT.

The 1 MeV neutron equivalent fluence in the decay tunnel is shown in Fig. 5.20. Compared to Fig. 5.19, a slightly higher event rate is observed because the equivalent fluence accounts for all particle species, including contributions from the secondary meson beam.

5.6 Air Activation

The following section summarizes the radiological assessments for air activation, which were carried out by the CERN HSE-RP-AS group. The reader is referred to the complete report prepared by the CERN radiation-protection experts [116].

Another important aspect of radioprotection is air activation. When high-energy particles interact with the air, stable nuclei can become radioactive through various processes such as neutron capture, (p, n), (n, p), or (n, α) reactions, as well as nuclear fission and spallation. Air activation therefore represents a potential risk both for personnel and for the environment, and must be carefully quantified and minimized.

The production of radionuclides in the air and the resulting activities were evaluated for the TT61 tunnel and the decay tunnel volumes. The highest levels of air activation are expected in regions with the largest particle fluences, namely the target station, the dump, and the section in between. Among the wide range of isotopes produced, only those with half-lives long enough to represent a radiological concern were considered. Specifically, the following isotopes were studied: ^{41}Ar, ^{13}N, ^{15}O, ^{11}C, ^{14}C, ^{3}H, ^{7}Be, ^{32}P, ^{33}P, and ^{35}S. Production yields were determined by scoring the fluence spectra of neutrons, protons, pions, and photons in the relevant volumes and folding them with the corresponding production cross-sections using *ActiWiz*. ActiWiz is a CERN-developed tool for assessing the radiological hazards of materials exposed to proton accelerator environments. It allows users to define the chemical composition of materials and to estimate activation levels via a risk-assessment model based on extensive FLUKA Monte Carlo simulations [117].

The calculated total and specific activities were compared with the CA guidance values for airborne activity defined by Swiss legislation. A value of 1 CA for a given radioisotope corresponds to exposure to airborne activity for 40 hours per week over 50 weeks per year, resulting in a cumulative effective dose of 20 mSv [118]. At CERN, a limit of 0.1 CA is applied for airborne activity in Supervised Radiation Areas.

A FLUKA Monte Carlo simulation was performed assuming 200 days of irradiation with a proton beam intensity of $1.157 \cdot 10^{11}$ p/s, corresponding to a total annual proton budget of $2 \cdot 10^{18}$ PoT. Without any cooling time, the air activation level in the TT61 tunnel (volume: 775 m^3) exceeds the Swiss legal limit by a factor of 32. The total activity (A) amounts to 1.63 GBq, with a specific activity (A_s) of 2.11 MBq/m^3, dominated by short-lived radionuclides such as ^{15}O (2 min), ^{13}N (10 min), and ^{11}C (20.4 min), as summarized in Table 5.1.

Region of interest	**Volume (m^3)**	***A* (Bq)**	**A_s (Bq/m^3)**	**A_s (CA)**	**Inhalation dose rate (µSv/h)**
TT61	775	$1.63 \cdot 10^9$	$2.11 \cdot 10^6$	32	52.8
Decay tunnel	1240	$1.87 \cdot 10^6$	1500	0.0235	0.0385

Table 5.1: Air activation parameters for different zones of the nuSCOPE facility, namely the main TT61 tunnel and the decay tunnel. No cooling was assumed and no air flush to the experiment zones.

After one hour of cooling, the total specific activity is reduced to 12.7 CA, corresponding to 0.814 MBq/m^3; in parallel, the total activity decreases to 0.631 GBq (see Table 5.2). This confirms that the majority of the prompt activity originates from short-lived isotopes, which decay rapidly within the first hour.

Region of interest	**Volume (m^3)**	***A* (Bq)**	**A_s (Bq/m^3)**	**A_s (CA)**	**Inhalation dose rate (µSv/h)**
TT61	775	$0.631 \cdot 10^9$	$8.14 \cdot 10^5$	12.7	51.5
Decay tunnel	1240	$0.733 \cdot 10^6$	591	$9.8 \cdot 10^{-3}$	0.0385

Table 5.2: Air activation parameters for different zones of the facility, namely the main TT61 tunnel and the decay tunnel. One hour cooling has been assumed with no air flush to the experiment zones.

To minimize personnel exposure, activated air must be flushed before access to the facility. A cool-down time of one hour before venting further reduces the environmental impact. Assuming a ventilation rate of 10 000 m^3/h, access to TT61 could be permitted after about 15 minutes, at which point inhalation dose rates fall below 1 µSv/h. This corresponds to 0.1 CA, i.e. the CERN threshold for airborne activity concentration in Radiation Areas without contamination risk. Higher ventilation rates would proportionally shorten the venting time, enabling faster interventions in case of faults or incidents.

In contrast, no air flush is required before accessing the decay tunnel, provided that air exchange with TT61 is effectively prevented. In this case, total specific activities remain below 0.1 CA and inhalation dose rates are consistently below 1 µSv/h.

Table 5.3 summarizes the relative contributions of different isotopes to the total activity after one hour of cooling. The dominant contributors are ^{7}Be (42%) and ^{41}Ar (39%), with smaller contributions from other radionuclides.

Radionuclide	**Half life**	**Total A (Bq)**	**A (CA)**	**Contribution to Activity**
^{7}Be	53.3 d	$2.66 \cdot 10^8$	1.72	42%
^{41}Ar	110 min	$2.44 \cdot 10^8$	6.29	39%
^{11}C	20.4 min	$4.74 \cdot 10^7$	0.875	8%
^{3}H	12.32 y	$3.37 \cdot 10^7$	0.218	5%
^{14}C	5700 y	$1.13 \cdot 10^7$	1.46	2%
^{13}N	10 min	$4.66 \cdot 10^6$	0.08	1%
^{32}P	14.3 d	$2.39 \cdot 10^6$	1.03	$< 1\%$
^{33}P	25.6 d	$2.08 \cdot 10^6$	0.448	$< 1\%$
^{35}S	87.3 d	$2.61 \cdot 10^6$	0.421	$< 1\%$
Sum	–	$6.31 \cdot 10^8$	12.7	$\sim 100\%$

Table 5.3: Radionuclides created in the TT61 tunnel with their activities and percentage contributions to the total activity. One hour cooling has been assumed with no air flush to the experiment zones.

Conclusions

Chapter 4 presented a comprehensive thermal analysis of the nuSCOPE beamline components, while Chapter 5 detailed the radiological assessment and detector studies. Taken together, these experimental results validate the design's robustness under operational conditions and demonstrate that the system meets its key performance and safety requirements without exceeding material or safety limits.

In the thermal studies of Chapter 4, the graphite production target was confirmed to experience the highest energy deposition and temperature rise. The FLUKA-based simulations showed a peak temperature increase of approximately $\Delta T \sim 400$ K per pulse at about 16.5 cm into the target's length. Despite this significant localized heating, the target's material properties provide a comfortable margin: the corresponding peak thermal stress (on the order of 12 MPa) remains well below graphite's failure threshold (tens of MPa, with ~ 50 MPa compressive strength). This indicates that the target will remain structurally sound during beam operation, fully justifying the choice of graphite for its ability to withstand intense pulsed heating without permanent damage. Moreover, the target's surface temperature rise is more moderate, which, combined with cooling between spills, helps avoid deleterious effects such as oxidation or thermal shock. In short, the target is expected to operate reliably at the SPS beam intensity, with no immediate risk of thermal failure or excessive erosion.

Downstream beamline elements were found to undergo substantially smaller thermal loads. The copper collimator, which shapes the beam after the target, sees a maximum temperature rise of only $\mathcal{O}(10\text{ K})$. Such a modest increase can be safely managed by passive cooling. Indeed, the simulations revealed that the hottest spot in the collimator is confined to the inner left wall of its bore (where a slight beam tilt causes primary protons to scrape it), yet even this peak ΔT remains low enough that active water cooling is unnecessary. Likewise, the first quadrupole magnets in the beamline undergo negligible temperature rises (on the order of a few kelvins at most) that are easily handled by their existing cooling systems for electromagnetic coils. The primary hadron beam dump, which absorbs the residual 400 GeV protons at the end of the beamline, was shown to experience a maximum temperature increase of only about 12 K in its core. This is achieved by its layered structure of aluminium, copper, and iron, which spreads out the energy deposition and keeps the thermal load within safe limits. Other structures, such as the beam pipe and shielding blocks, were found to have even smaller temperature increases (often below 1 K), confirming that thermal effects beyond the initial beamline section are practically negligible. Significantly, the simulations indicate that roughly 82% of the primary proton beam's energy is deposited and contained within the beamline elements (target, collimator, magnets, dumps, etc.), demonstrating that the system effectively captures the beam's energy as heat in the intended areas. All these findings attest that from a thermal standpoint the beamline can operate continuously at full beam intensity without damaging components or requiring design changes.

Chapter 5 focused on the radiological performance of the beamline and the implications for both safety and detector operation. The radioprotection studies confirmed that the shielding around the beamline is effective in reducing radiation to acceptable levels for personnel and equipment. Simulations of the prompt dose rate under nominal running conditions showed that, outside the shielding, radiation levels stay within regulatory limits. In the vicinity of the target station, the prompt dose was estimated at 50 µSv/h, which is relatively high in absolute terms but still comparable to similar neutrino facilities and remains below the CERN-imposed access threshold. Along the beam transfer line and at the entrance of the decay tunnel, the prompt dose drops to the $\mathcal{O}(1-10\ \mu\text{Sv/h})$ range, illustrating how the combination of iron and concrete shielding provides a safe environment even relatively close to the beam. These results imply that, in emergency or controlled-access situations, the tunnel could be approached without excessive hazard.

The study did identify a few localized spots where additional shielding or design tweaks could further optimize protection. For instance, it was noted that the first section of the primary beam pipe passes near the first tracker plane; as a consequence, a relatively high dose was found on one side of the tracker due to radiation streaming directly from this unshielded beam pipe. Results suggest that extending the shielding or adding a small shadowing wall in this region would reduce the background on the tracker and improve the overall radiation isolation of sensitive detectors. Similarly, a minor residual muon flux was observed to reach the end of the TT61 tunnel from the primary dump area; the analysis indicates that adding a modest amount of additional shielding at the downstream end of the tunnel would completely absorb these last muons, eliminating any potential external exposure.

Aside from these refinements, the radiological analysis demonstrates that the facility, as designed, already meets safety requirements: the calculated residual dose rates (after appropriate cooling periods following beam shutdown) decline to levels that permit maintenance access.

Crucially, the studies described in Chapter 5 also examined the radiation impact on the nuSCOPE detector systems, especially the silicon pixel trackers that enable the neutrino tagging technique. The first tracker, being closest to the beam, accumulates the highest dose and neutron fluence over the experiment's lifetime. The simulation of total ionizing dose over a 10^{13} PoT spill yielded a peak dose of about 23 Gy at the tracker's center. This level of dose is projected to be tolerable for the chosen pixel technology. Likewise, the integrated 1 MeV neutron equivalent fluence was found to be on the order of $2 \cdot 10^{16}$ $n_{\text{eq}}/\text{cm}^2$ at the hottest spot. This is a substantial irradiation, but it remains within the endurance limits of the detector design, comparable to what modern high-radiation silicon detectors can sustain. In summary, the analysis shows that the experiment's most radiation-sensitive elements (the silicon pixel trackers) are sufficiently protected to last through the planned exposure, with some safety margin. Any needed proactive measures can be implemented to further enhance this margin.

Moreover, the studies of penetrating particle fluence demonstrated that the beamline measures to mitigate secondary muons and neutrons are highly effective. The primary proton dump reduces the outgoing muon flux by at least two orders of magnitude. Only muons in the high-energy tail of the spectrum (< 1 GeV) can escape the dump shielding, and many of these are subsequently lost to the tunnel walls via multiple scattering. The simulated muon yield immediately downstream of the dump is on the order of 10^{-2} muons per proton on target, and this is greatly attenuated along the length of the tunnel.

By the end of the decay tunnel, the muon flux is further collimated and limited by the beam optics: the surviving muons have a narrow momentum distribution peaked around the nominal secondary beam momentum (8.5 GeV with a 10% momentum bite). Importantly, the instrumented hadron dump was shown to absorb these remnant muons completely within its first sections. The simulations confirmed that essentially no muons reach the region beyond the hadron dump; in other words, no observable muon flux reaches the neutrino detector itself. This outcome is a critical validation of the experimental design, as it guarantees that the neutrino detector will operate in a low-background environment.

Similarly, secondary neutrons produced by beam interactions are largely contained: those generated in the dumps or shielding are either absorbed in place or reduced to negligible flux by the time they could reach external or detector areas.

Finally, the air activation study highlights the importance of implementing adequate ventilation and cooling procedures in the TT61 tunnel, where short-lived radionuclides significantly raise the specific activity immediately after beam operation. While one hour of cooling already reduces activity levels by an order of magnitude, controlled air flushing is essential to ensure personnel safety and compliance with CERN and Swiss regulatory limits. These results confirm that with appropriate operational protocols, air activation does not represent a limiting factor for the safe operation of the nuSCOPE facility.

In conclusion, the simulation results from Chapters 4 and 5 demonstrate that the nuSCOPE beamline and detector system will perform as intended. Altogether, these findings validate the beamline and detector engineering: they show that the apparatus can deliver a beam for physics runs reliably, safely, and without adverse effects, therefore confirming the feasibility of the nuSCOPE neutrino program as a whole. The work presented in this thesis provides confidence that the beamline's key requirements are met and that the envisioned operation is both technically achievable and scientifically productive, with all principal risks mitigated by design.

Acknowledgements

The very first acknowledgment must go to my supervisor, Prof. Francesco Terranova, because after guiding me through my bachelor's thesis, he was the one who proposed the possibility of continuing with my master's thesis at CERN. That moment was truly decisive for my academic path and beyond. At CERN, the person who undoubtedly guided and supported me the most was Nikos, who taught me that "in life there are no problems, only challenges". We have three years of challenges ahead of us. I would also like to mention Marc who, especially at the beginning, helped me practically in solving countless problems, some trivial and some less so. Finally, special thanks to the CERN RP Section, especially Claudia and Elzbieta, for their great support in the final stages of data analysis and radiation protection calculations, as well as for completing the analysis of air activation in the tunnels.

Since this thesis stems from my experience at CERN, this seems the right time to thank all those people who made my first stay there so memorable. First of all, I would like to thank my flatmates, Alessandro, and first Federica and then Hugo, with whom I shared almost six months of my life. Even if we rarely managed to have dinner all together, I will always treasure the moments we shared. I also want to thank all my colleagues; starting with my office mate, Paraskevi, whom I endlessly bothered in every possible way and who still talks to me, and then Antonio, Marija, Mihailo, Naini, Dušan, Iasonas, Javier, Iliasse, Alex, Eva, Bea, and Jan. You are much more than colleagues – you are friends. I would like to conclude this CERN parenthesis by thanking the LHCb community who, through parties, drinks, and barbecues, welcomed me as if I were one of them.

Now it is time to thank my family; this part will be largely the same as the one of my bachelor's thesis, since, fortunately, we are all still here and still care deeply for each other. Starting with my mom and dad, who have supported me in every choice of my life and, even though their interests are completely different from mine, have always encouraged me to follow my passions without ever imposing anything. I also want to thank my uncle and aunt, Chiara and Francesco, who, as physicists, have helped me throughout my studies and passed on some of their passion for this field of science. Of course, a heartfelt thanks goes to my grandparents Roberto, Sergio, and Giorgio – and especially my grandmother Giovanna, who has been preparing me lavish meals since before I had teeth, and who patiently endures my endless polemical discussions. A huge thank you also goes to my brother Andrea, who, in twenty years of ups and downs, has always been one of the most important people in my life. The last family mention goes to Noes, whom I now consider like an adopted sister.

I also owe an enormous thank you to all my friends. Starting with the oldest ones and my high school friends: Andrea, Lisa, Rebecca, Francesca, and Alessandro, and especially Riccardo who, even if we see each other less and less often, still makes me laugh uncontrollably whenever I recall our countless adventures. Now it's the turn of "the goodfellas", Edoardo and Marco; I don't even know where to start thanking you, there are so many things I could say (and very few appropriate to write in a thesis...); I'll just tell you that I love you. In this context, I would also like to mention Rebecca who, even though we haven't known each other for long, shared several incredible (and at times tragicomic) moments with us this summer. I want to thank as well Cecilia, Benedetta, Rachele, and Sofia (+ Otto) for being the best friends I could ever wish for and for keeping me company during the early stages of writing this thesis. A special thank you also goes to Claudia for being my personal confidante in moments of emotional difficulty. And a mention goes to all the members of the Gossippers group who I haven't already mentioned: Beatrice, Gaia, Giulia, Paolo, Simone, and Sofia.

Now it is time to mention and thank all the people I have met during these five years of university. Naturally, I must begin with those with whom I shared most of my bachelor's studies and who later became some of my dearest friends: Giacomo, Pietro, Elena, Alessia, and Francesco. Once this whole graduation formality is done, how about a good game of briscola chiamata? I also want to thank Daniele, Giulio, Davide, and Marco for enriching my academic journey. Finally, I would like to end this long round of thanks with all the people I met during my master's degree, in particular Alberto, Riccardo, and Gloria.

This time, I won't conclude with a some stupid phrase like I did last time, but simply by saying that I am grateful to know you and to have you in my life. As excited as I am for the next chapter of my journey, one of the few things I will miss about home will be you.

I love you.

Ringraziamenti

Il primo ringraziamento deve andare obbligatoriamente al mio relatore, il prof. Francesco Terranova, perchè dopo avermi seguito durante il mio percorso di tesi triennale è venuto a propormi la possibilità di proseguire con la tesi magistrale al CERN; questo momento è stato fondamentale per la mia carriera universitaria e non solo. Al CERN la persona che in assoluto mi ha guidato e aiutato nel mio percorso è senza dubbio Nikos, il quale mi ha insegnato che "nella vita non esistono problemi, solo sfide". Abbiamo tre anni di sfide davanti a noi. Vorrei citare anche Marc che, soprattutto all'inizio, mi ha aiutato in maniera pratica a risolvere una miriade di problemi, più o meno stupidi. Infine, un ringraziamento speciale alla sezione RP del CERN, in particolare a Claudia ed Elzbieta, per il loro grande supporto nelle fasi finali dell'analisi dati e per i calcoli radioprotezionistici, nonché per aver portato a termine l'analisi sull'attivazione dell'aria nei tunnel.

Dato che questa tesi nasce dalla mia esperienza al CERN, mi sembra il momento di citare tutte quelle persone che hanno reso la mia prima esperienza memorabile. Innanzitutto vorrei ringraziare i miei coinquilini, Alessandro e, Federica prima e Hugo poi, con i quali ho condiviso quasi sei mesi della mia vita. Anche se raramente riuscivamo a cenare tutti insieme, ricorderò per sempre i momenti che abbiamo condiviso. Voglio anche ringraziare tutti i miei colleghi; in primis, la mia compagna di ufficio, Paraskevi, alla quale ho rotto le scatole in ogni modo possibile e ancora mi parla, passando poi da Antonio, Marija, Mihailo, Naini, Dušan, Iasonas, Javier, Iliasse, Alex, Eva, Bea and Jan. Siete ben più di semplici colleghi, siete amici. Vorrei terminare la parentesi CERN citando la comunità di LHCb che tra feste, drink e barbecue mi ha accolto come se ne facessi parte.

Ora è arrivato il momento di ringraziare la mia famiglia; questa sezione sarà in gran parte identica ai ringraziamenti della mia tesi triennale dato che, fortunamente, siamo ancora tutti qui e ci vogliamo ancora tutti bene. Partiamo dalla mamma e dal babbo, che mi hanno supportato in ogni scelta della mia vita e, per quanto i loro interessi siano diametralmente opposti ai miei, mi hanno sempre spronato a seguire le mie passioni senza mai impormi nulla. Ci tengo a ringraziare anche i miei zii, Chiara e Francesco, che, in quanto fisici, mi hanno aiutato durante tutto il mio percorso scolastico e trasmesso un po' della loro passione per questa branca della scienza. Ovviamente non può mancare un grazie sentito ai miei nonni Roberto, Sergio, Giorgio e soprattutto a mia nonna Giovanna, che mi prepara sontuosi pranzi da prima che mi spuntassero i dentini e che mi sopporta, nelle mie infinite discussioni polemiche. Un grande ringraziamento deve anche essere fatto a mio fratello Andrea che, in vent'anni di alti e bassi, è sempre stato una delle persone più importanti della mia vita. L'ultima menzione che ci tengo a fare adesso che parlo di famiglia è la Noes, che ormai considero come una sorella acquisita.

Un enorme ringraziamento va anche a tutti i miei amici. Parto da quelli di più lunga data e quelli del liceo, come Andrea, Lisa, Rebecca, Francesca e Alessandro e in particolare Riccardo: anche se ormai ci vediamo sempre più raramente, ogni volta che ripenso alle nostre mille avventure mi piego dalle risate. Ora è il momento dei "ragazzi", ovvero Edoardo e Marco; non so neanche da dove cominciare a ringraziarvi, ci sono tante di quelle cose che si potrebbero dire (e poche che sarebbe appropriato scrivere in una tesi di laurea...); mi limiterò a dirvi che vi voglio bene. In questo frangente, vorrei anche citare Rebecca con cui, anche se non ci conosciamo da molto, ho condiviso diversi incredibili (e anche tragicomici) momenti durante questa estate. Voglio ringraziare anche Cecilia, Benedetta, Rachele e Sofia (+ Otto) per essere le migliori amiche che potessi mai desiderare e per avermi tenuto hanno compagnia durante la prima stesura di questa tesi. Un grazie speciale va anche a Claudia per essere stata la mia confidente personale in momenti di difficoltà emotive. Una menzione va anche a tutti i componenti del gruppo dei Gossippers che non sono stati citati in precedenza, ovvero Beatrice, Gaia, Giulia, Paolo, Simone e Sofia.

Adesso è arrivato il momento di citare e ringraziare tutte le persone conosciute in questi cinque anni di università. Ovviamente è giusto iniziare dalle persone con le quali ho condiviso la maggior parte dei miei studi in triennale e che poi si sono rivelati alcuni tra i miei amici più cari, ossia Giacomo, Pietro, Elena, Alessia e Francesco. Appena finisco questa formalità della laurea ci facciamo una bella partita a briscola chiamata? Inoltre voglio anche ringraziare Daniele, Giulio, Davide e Marco per aver arricchito il mio percorso universitario. Vorrei terminare questo lungo giro di ringraziamenti con tutte quelle persone che ho conosciuto durante la laurea magistrale, in particolare Alberto, Riccardo e Gloria.

Questa volta non terminerò con una frase di circostanza come l'ultima volta ma semplicemente dicendo che sono grato di conoscervi e che facciate parte della mia vita. Per quanto io possa essere gasato per il prossimo capitolo della mia vita, una delle poche cose che rimpiangerò di casa sarete proprio voi.

Vi voglio bene.

List of Figures

Bibliography

[1] C. D. Ellis and W. A Wooster. 'The average energy of disintegration of radium E'. In: *Proc. Roy. Soc. Lond. A* 117.776 (1927), pp. 109–123. DOI: 10.1098/rspa.1927.0168.

[2] K. Zuber. *Neutrino Physics*. CRC Press, May 2020, p. 465. ISBN: 9781315195612. DOI: 10.1201/9781315195612.

[3] C. L. Cowan et al. 'Detection of the Free Neutrino: a Confirmation'. In: *Science* 124.3212 (1956), pp. 103–104. DOI: 10.1126/science.124.3212.103. eprint: https://www.science.org/doi/pdf/10.1126/science.124.3212.103. URL: https://www.science.org/doi/abs/10.1126/science.124.3212.103.

[4] R. Davis. 'Attempt to Detect the Antineutrinos from a Nuclear Reactor by the ^{37}Cl ($\bar{\nu}$, e^-) ^{37}Ar Reaction'. In: *Phys. Rev.* 97.3 (Feb. 1955), pp. 766–769. DOI: 10.1103/PhysRev.97.766. URL: https://link.aps.org/doi/10.1103/PhysRev.97.766.

[5] J.K. Bienlein et al. 'Spark chamber study of high-energy neutrino interactions'. In: *Physics Letters* 13.1 (1964), pp. 80–86. ISSN: 0031-9163. DOI: https://doi.org/10.1016/0031-9163(64)90316-6. URL: https://www.sciencedirect.com/science/article/pii/0031916364903166.

[6] B. Pontecorvo. 'Electron and Muon Neutrinos'. In: *Zh. Eksp. Teor. Fiz.* 37 (1959), pp. 1751–1757.

[7] G. Danby et al. 'Observation of High-Energy Neutrino Reactions and the Existence of Two Kinds of Neutrinos'. In: *Phys. Rev. Lett.* 9.1 (July 1962), pp. 36–44. DOI: 10.1103/PhysRevLett.9.36. URL: https://link.aps.org/doi/10.1103/PhysRevLett.9.36.

[8] B. Pontecorvo. 'Neutrino Experiments and the Problem of Conservation of Leptonic Charge'. In: *Zh. Eksp. Teor. Fiz.* 53 (1967), pp. 1717–1725.

[9] Z. Maki, M. Nakagawa, and S. Sakata. 'Remarks on the Unified Model of Elementary Particles'. In: *Progress of Theoretical Physics* 28.5 (Nov. 1962), pp. 870–880. ISSN: 0033-068X. DOI: 10.1143/PTP.28.870. eprint: https://academic.oup.com/ptp/article-pdf/28/5/870/5258750/28-5-870.pdf. URL: https://doi.org/10.1143/PTP.28.870.

[10] C. Giganti, S. Lavignac, and M. Zito. 'Neutrino oscillations: The rise of the PMNS paradigm'. In: *Progress in Particle and Nuclear Physics* 98 (Jan. 2018), pp. 1–54. ISSN: 0146-6410. DOI: 10.1016/j.ppnp.2017.10.001. URL: http://dx.doi.org/10.1016/j.ppnp.2017.10.001.

[11] S. Navas et al. 'Review of particle physics'. In: *Phys. Rev. D* 110.3 (2024), p. 030001. DOI: 10.1103/PhysRevD.110.030001.

[12] C. Jarlskog. 'Commutator of the Quark Mass Matrices in the Standard Electroweak Model and a Measure of Maximal CP Nonconservation'. In: *Phys. Rev. Lett.* 55.10 (Sept. 1985), pp. 1039–1042. DOI: 10.1103/PhysRevLett.55.1039. URL: https://link.aps.org/doi/10.1103/PhysRevLett.55.1039.

[13] J. A. Formaggio and G. P. Zeller. 'From eV to EeV: Neutrino cross sections across energy scales'. In: *Rev. Mod. Phys.* 84.3 (Sept. 2012), pp. 1307–1341. DOI: 10.1103/RevModPhys.84.1307. URL: https://link.aps.org/doi/10.1103/RevModPhys.84.1307.

[14] C. Giunti and C. W. Kim. *Fundamentals of Neutrino Physics and Astrophysics*. Oxford University Press, Mar. 2007. ISBN: 9780198508717. DOI: 10.1093/acprof:oso/9780198508717.001.0001. URL: https://doi.org/10.1093/acprof:oso/9780198508717.001.0001.

[15] Super-Kamiokande Collaboration. 'Solar neutrino measurements in Super-Kamiokande I'. In: *Phys. Rev. D* 73.11 (June 2006), p. 112001. DOI: 10.1103/PhysRevD.73.112001. URL: https://link.aps.org/doi/10.1103/PhysRevD.73.112001.

[16] R. P. Feynman. 'Very High-Energy Collisions of Hadrons'. In: *Phys. Rev. Lett.* 23.24 (Dec. 1969), pp. 1415–1417. DOI: 10.1103/PhysRevLett.23.1415. URL: https://link.aps.org/doi/10.1103/PhysRevLett.23.1415.

[17] C.H. Llewellyn Smith. 'Neutrino reactions at accelerator energies'. In: *Physics Reports* 3.5 (1972), pp. 261–379. ISSN: 0370-1573. DOI: https://doi.org/10.1016/0370-1573(72)90010-5. URL: https://www.sciencedirect.com/science/article/pii/0370157372900105.

[18] D. Casper. 'The nuance neutrino physics simulation, and the future'. In: *Nuclear Physics B - Proceedings Supplements* 112.1 (2002), pp. 161–170. ISSN: 0920-5632. DOI: https://doi.org/10.1016/S0920-5632(02)01756-5. URL: https://www.sciencedirect.com/science/article/pii/S0920563202017565.

[19] C. W. Walter. 'Why understanding neutrino interactions is important for oscillation physics'. In: *AIP Conference Proceedings* 967.1 (Dec. 2007), pp. 3–8. ISSN: 0094-243X. DOI: 10.1063/1.2834507. eprint: https://pubs.aip.org/aip/acp/article-pdf/967/1/3/11859991/3_1_online.pdf. URL: https://doi.org/10.1063/1.2834507.

[20] J. Strait et al. *Long-Baseline Neutrino Facility (LBNF) and Deep Underground Neutrino Experiment (DUNE) Conceptual Design Report Volume 3: Long-Baseline Neutrino Facility for DUNE June 24, 2015*. 2016. arXiv: 1601.05823. URL: https://arxiv.org/abs/1601.05823.

[21] F. Di Lodovico on behalf of the Hyper-Kamiokande Collaboration. 'The Hyper-Kamiokande Experiment'. In: *Journal of Physics: Conference Series* 888.1 (Sept. 2017), p. 012020. DOI: 10.1088/1742-6596/888/1/012020. URL: https://dx.doi.org/10.1088/1742-6596/888/1/012020.

[22] D. Rein and L. M. Sehgal. 'Coherent π^0 production in neutrino reactions'. In: *Nuclear Physics B* 223.1 (1983), pp. 29–44. ISSN: 0550-3213. DOI: https://doi.org/10.1016/0550-3213(83)90090-1. URL: https://www.sciencedirect.com/science/article/pii/0550321383900901.

[23] A. Branca et al. 'A New Generation of Neutrino Cross Section Experiments: Challenges and Opportunities'. In: *Symmetry* 13.9 (2021). DOI: 10.3390/sym13091625. arXiv: 2108.12212 [hep-ex]. URL: https://arxiv.org/abs/2108.12212.

[24] The Daya Bay Collaboration. 'Observation of Electron-Antineutrino Disappearance at Daya Bay'. In: *Physical Review Letters* 108.17 (Apr. 2012). ISSN: 1079-7114. DOI: 10.1103/physrevlett.108.171803. URL: http://dx.doi.org/10.1103/PhysRevLett.108.171803.

[25] F. Terranova. 'Future Long-Baseline Neutrino Experiments'. In: *Universe* 10.5 (2024). ISSN: 2218-1997. DOI: 10.3390/universe10050221. URL: https://www.mdpi.com/2218-1997/10/5/221.

[26] T. Katori and M. Martini. 'Neutrino–nucleus cross sections for oscillation experiments'. In: *Journal of Physics G: Nuclear and Particle Physics* 45.1 (Dec. 2017). DOI: 10.1088/1361-6471/aa8bf7. URL: https://dx.doi.org/10.1088/1361-6471/aa8bf7.

[27] K2K Collaboration. 'Measurement of neutrino oscillation by the K2K experiment'. In: *Physical Review D* 74.7 (Oct. 2006). ISSN: 1550-2368. DOI: 10.1103/physrevd.74.072003. URL: http://dx.doi.org/10.1103/PhysRevD.74.072003.

[28] K2K Collaboration. 'Search for Coherent Charged Pion Production in Neutrino-Carbon Interactions'. In: *Phys. Rev. Lett.* 95.25 (Dec. 2005), p. 252301. DOI: 10.1103/PhysRevLett.95.252301. URL: https://link.aps.org/doi/10.1103/PhysRevLett.95.252301.

[29] MiniBooNE Collaboration. 'The MiniBooNE detector'. In: *Nuclear Instruments and Methods in Physics Research Section A: Accelerators, Spectrometers, Detectors and Associated Equipment* 599.1 (Feb. 2009), pp. 28–46. ISSN: 0168-9002. DOI: 10.1016/j.nima.2008.10.028.

[30] LSND Collaboration. 'Evidence for neutrino oscillations from the observation of $\bar{\nu}_e$ appearance in a $\bar{\nu}_\mu$ beam'. In: *Phys. Rev. D* 64.11 (Nov. 2001), p. 112007. DOI: 10.1103/PhysRevD.64.112007. URL: https://link.aps.org/doi/10.1103/PhysRevD.64.112007.

[31] J. L. Alcaraz-Aunion et al. 'Measurement of the ν_μ-CCQE cross section in the SciBooNE experiment'. In: *AIP Conference Proceedings*. AIP, 2009, pp. 145–150. DOI: 10.1063/1.3274145. URL: http://dx.doi.org/10.1063/1.3274145.

[32] SciBooNE Collaboration. 'Improved measurement of neutral current coherent π^0 production on carbon in a few-GeV neutrino beam'. In: *Phys. Rev. D* 81.11 (June 2010), p. 111102. DOI: 10.1103/PhysRevD.81.111102. URL: https://link.aps.org/doi/10.1103/PhysRevD.81.111102.

[33] P. Adamson et al. 'The NuMI neutrino beam'. In: *Nuclear Instruments and Methods in Physics Research Section A: Accelerators, Spectrometers, Detectors and Associated Equipment* 806 (Jan. 2016), pp. 279–306. ISSN: 0168-9002. DOI: 10.1016/j.nima.2015.08.063. URL: http://dx.doi.org/10.1016/j.nima.2015.08.063.

[34] L. Aliaga et al. 'Design, calibration, and performance of the MINERvA detector'. In: *Nuclear Instruments and Methods in Physics Research Section A: Accelerators, Spectrometers, Detectors and Associated Equipment* 743 (Apr. 2014), pp. 130–159. ISSN: 0168-9002. DOI: 10.1016/j.nima.2013.12.053. URL: http://dx.doi.org/10.1016/j.nima.2013.12.053.

[35] F. Vannucci. 'The NOMAD Experiment at CERN'. In: *Adv. High Energy Phys.* 2014 (2014), p. 129694. DOI: 10.1155/2014/129694. URL: https://cds.cern.ch/record/1666456.

[36] OPERA Collaboration. 'Observation of a first ν_τ candidate event in the OPERA experiment in the CNGS beam'. In: *Physics Letters B* 691.3 (July 2010), pp. 138–145. ISSN: 0370-2693. DOI: 10.1016/j.physletb.2010.06.022. URL: http://dx.doi.org/10.1016/j.physletb.2010.06.022.

[37] CHORUS Collaboration. 'Charged-particle multiplicities in charged-current neutrino and anti-neutrino–nucleus interactions'. In: *The European Physical Journal C* 51.4 (Aug. 2007). ISSN: 1434-6052. DOI: 10.1140/epjc/s10052-007-0366-8. URL: http://dx.doi.org/10.1140/epjc/s10052-007-0366-8.

[38] The T2K Collaboration. 'The T2K experiment'. In: *Nuclear Instruments and Methods in Physics Research Section A: Accelerators, Spectrometers, Detectors and Associated Equipment* 659.1 (Dec. 2011), pp. 106–135. ISSN: 0168-9002. DOI: 10.1016/j.nima.2011.06.067. URL: http://dx.doi.org/10.1016/j.nima.2011.06.067.

[39] The NOvA Collaboration. 'Improved measurement of neutrino oscillation parameters by the NOνA experiment'. In: *Phys. Rev. D* 106.3 (Aug. 2022), p. 032004. DOI: 10.1103/PhysRevD.106.032004. URL: https://link.aps.org/doi/10.1103/PhysRevD.106.032004.

[40] X. Bu. *Measurement of Electron Neutrino Charged-Current Inclusive Cross Section in 1-3 GeV energy region with the NOνA Near Detector*. 2016. arXiv: 1601.01213 [hep-ex]. URL: https://arxiv.org/abs/1601.01213.

[41] S. E. Kopp. 'Accelerator neutrino beams'. In: *Physics Reports* 439.3 (2007), pp. 101–159. ISSN: 0370-1573. DOI: https://doi.org/10.1016/j.physrep.2006.11.004. URL: https://www.sciencedirect.com/science/article/pii/S0370157306004431.

[42] M. Schwartz. 'Feasibility of Using High-Energy Neutrinos to Study the Weak Interactions'. In: *Phys. Rev. Lett.* 4 (6 Mar. 1960), pp. 306–307. DOI: 10.1103/PhysRevLett.4.306. URL: https://link.aps.org/doi/10.1103/PhysRevLett.4.306.

[43] A. Longhin, L. Ludovici, and F. Terranova. 'A novel technique for the measurement of the electron neutrino cross section'. In: *The European Physical Journal C* 75.4 (Apr. 2015). ISSN: 1434-6052. DOI: 10.1140/epjc/s10052-015-3378-9. URL: http://dx.doi.org/10.1140/epjc/s10052-015-3378-9.

[44] M. Giesch et al. 'Status of magnetic horn and neutrino beam'. In: *Nuclear Instruments and Methods* 20 (1963), pp. 58–65. ISSN: 0029-554X. DOI: https://doi.org/10.1016/0029-554X(63)90391-4. URL: https://www.sciencedirect.com/science/article/pii/0029554X63903914.

[45] N. Charitonidis et al. 'Design and Diagnostics of High-Precision Accelerator Neutrino Beams'. In: *Applied Sciences* 11.4 (Feb. 2021), p. 1644. ISSN: 2076-3417. DOI: 10.3390/app11041644. URL: http://dx.doi.org/10.3390/app11041644.

[46] R. P. Feynman. 'The behavior of hadron collisions at extreme energies'. In: *Conf. Proc. C* 690905 (1969), pp. 237–258.

[47] S. van der Meer. *A directive device for charged particles and its use in an enhanced neutrino beam*. CERN Yellow Reports: Monographs. Geneva: CERN, 1961. DOI: 10.5170/CERN-1961-007. URL: https://cds.cern.ch/record/278088.

[48] P. Limon et al. 'A sign-selected dichromatic neutrino beam'. In: *Nuclear Instruments and Methods* 116.2 (1974), pp. 317–321. ISSN: 0029-554X. DOI: https://doi.org/10.1016/0029-554X(74)90618-1. URL: https://www.sciencedirect.com/science/article/pii/0029554X74906181.

[49] E. H. M. Heijne. 'Muon Flux Measurement with Silicon Detectors in the Cern Neutrino Beams'. PhD thesis. Amsterdam University, July 1983. DOI: 10.5170/CERN-1983-006.

[50] E889 Collaboration. *Long baseline neutrino oscillation experiment at the AGS. Physics design report*. Tech. rep. Brookhaven National Lab., Upton, NY (United States), Mar. 1995. DOI: 10.2172/52878. URL: https://www.osti.gov/biblio/52878.

[51] K. T. McDonald. *An Off-Axis Neutrino Beam*. 2001. arXiv: hep-ex/0111033 [hep-ex]. URL: https://arxiv.org/abs/hep-ex/0111033.

[52] Kamiokande Working Group. *A Long Baseline Neutrino Oscillation Experiment Using J-PARC Neutrino Beam and Hyper-Kamiokande*. 2015. arXiv: 1412.4673 [physics.ins-det]. URL: https://arxiv.org/abs/1412.4673.

[53] Y. Itow. 'Construction status and prospects of the Hyper-Kamiokande project'. In: *Proceedings of 37th International Cosmic Ray Conference*. Vol. 395. 2021, p. 1192. DOI: 10.22323/1.395.1192.

[54] Hyper-Kamiokande Proto-Collaboration. *Hyper-Kamiokande Design Report*. 2018. arXiv: 1805.04163 [physics.ins-det]. URL: https://arxiv.org/abs/1805.04163.

[55] Super-Kamiokande Collaboration. 'Atmospheric neutrino oscillation analysis with improved event reconstruction in Super-Kamiokande IV'. In: *Progress of Theoretical and Experimental Physics* 2019.5 (May 2019), 053F01. ISSN: 2050-3911. DOI: 10.1093/ptep/ptz015. eprint: https://academic.oup.com/ptep/article-pdf/2019/5/053F01/28638877/ptz015.pdf. URL: https://doi.org/10.1093/ptep/ptz015.

[56] C. Naseby and the Hyper-Kamiokande Collaboration. 'Improving Hyper-Kamiokande sensitivity to CP violation with high precision near detector electron neutrino cross-section measurements'. In: *Journal of Physics: Conference Series* 2156.1 (Dec. 2021), p. 012121. DOI: 10.1088/1742-6596/2156/1/012121. URL: https://dx.doi.org/10.1088/1742-6596/2156/1/012121.

[57] S. Bhadra et al. *Letter of Intent to Construct a nuPRISM Detector in the J-PARC Neutrino Beamline*. 2014. arXiv: 1412.3086 [physics.ins-det]. URL: https://arxiv.org/abs/1412.3086.

[58] DUNE Collaboration. 'Volume I. Introduction to DUNE'. In: *Journal of Instrumentation* 15.08 (Aug. 2020), T08008. DOI: 10.1088/1748-0221/15/08/T08008. URL: https://dx.doi.org/10.1088/1748-0221/15/08/T08008.

[59] A.A. Machado et al. 'The X-ARAPUCA: an improvement of the ARAPUCA device'. In: *Journal of Instrumentation* 13.04 (Apr. 2018), p. C04026. DOI: 10.1088/1748-0221/13/04/C04026. URL: https://dx.doi.org/10.1088/1748-0221/13/04/C04026.

[60] DUNE Collaboration. 'The DUNE Far Detector Vertical Drift Technology. Technical Design Report'. In: *Journal of Instrumentation* 19.08 (Aug. 2024), T08004. DOI: 10.1088/1748-0221/19/08/T08004. URL: https://dx.doi.org/10.1088/1748-0221/19/08/T08004.

[61] DUNE Collaboration. 'Deep Underground Neutrino Experiment (DUNE) Near Detector Conceptual Design Report'. In: *Instruments* 5.4 (2021). ISSN: 2410-390X. DOI: 10.3390/instruments5040031. URL: https://www.mdpi.com/2410-390X/5/4/31.

[62] G. Amelino-Camelia et al. 'Physics with the KLOE-2 experiment at the upgraded DAΦNE'. In: *The European Physical Journal C* 68.3 (Aug. 1, 2010), pp. 619–681. ISSN: 1434-6052. DOI: 10.1140/epjc/s10052-010-1351-1. URL: https://doi.org/10.1140/epjc/s10052-010-1351-1.

[63] DUNE Collaboration. 'Long-baseline neutrino oscillation physics potential of the DUNE experiment'. In: *The European Physical Journal C* 80.10 (Oct. 2020). ISSN: 1434-6052. DOI: 10.1140/epjc/s10052-020-08456-z. URL: http://dx.doi.org/10.1140/epjc/s10052-020-08456-z.

[64] F. Acerbi et al. 'Design and performance of the ENUBET monitored neutrino beam'. In: *The European Physical Journal C* 83.10 (Oct. 26, 2023), p. 964. ISSN: 1434-6052. DOI: 10.1140/epjc/s10052-023-12116-3. URL: https://doi.org/10.1140/epjc/s10052-023-12116-3.

[65] B. Pontecorvo. 'Tagging Direct Neutrinos. A First Step To Neutrino Tagging'. In: *Lett. Nuovo Cim.* 25 (1979), pp. 257–259. DOI: 10.1007/BF02813638.

[66] G. Bohm. 'Project of a tagged neutrino facility at Serpukhov'. In: *10. Warsaw symposium on elementary particle physics*. 1987, p. 287–292.

[67] M. Perrin-Terrin. 'Neutrino tagging: a new tool for accelerator based neutrino experiments'. In: *The European Physical Journal C* 82.5 (May 20, 2022), p. 465. ISSN: 1434-6052. DOI: 10.1140/epjc/s10052-022-10397-8. URL: https://doi.org/10.1140/epjc/s10052-022-10397-8.

[68] A. Baratto-Roldán et al. 'NuTag: a proof-of-concept study for a long-baseline neutrino beam'. In: *The European Physical Journal C* 84.10 (Oct. 8, 2024), p. 1024. ISSN: 1434-6052. DOI: 10.1140/epjc/s10052-024-13324-1. URL: https://doi.org/10.1140/epjc/s10052-024-13324-1.

[69] F. Terranova et al. 'The ENUBET neutrino cross section experiment and plans at CERN'. In: *Proceedings of 12th Neutrino Oscillation Workshop – PoS(NOW2024)*. Vol. 473. 2025, p. 063. DOI: 10.22323/1.473.0063.

[70] F. Acerbi et al. 'The ENUBET positron tagger prototype: construction and test-beam performance'. In: *Journal of Instrumentation* 15.08 (Aug. 2020), P08001. DOI: 10.1088/1748-0221/15/08/P08001. URL: https://dx.doi.org/10.1088/1748-0221/15/08/P08001.

[71] E. G. Parozzi. 'Design and optimization of a variable momentum secondary beam-line for NP06/ENUBET project'. PhD thesis. Milan Bicocca U, Università degli Studi di Milano-Bicocca, Italy, 2023, Milan Bicocca U., 2023. URL: https://cds.cern.ch/record/2882547.

[72] A. Longhin and F. Terranova. *The NP06/ENUBET SPSC annual report (2023)*. Tech. rep. co-spokesperson: Francesco Terranova (University Milano-Bicocca and INFN). Geneva: CERN, 2023. URL: https://cds.cern.ch/record/2856999.

[73] G. Aglieri Rinella et al. 'The NA62 GigaTracKer: a low mass high intensity beam 4D tracker with 65 ps time resolution on tracks'. In: *Journal of Instrumentation* 14.07 (July 2019), P07010. DOI: 10.1088/1748-0221/14/07/P07010. URL: https://dx.doi.org/10.1088/1748-0221/14/07/P07010.

[74] S. Cadeddu et al. 'Recent developments in the IGNITE project on front-end design in CMOS 28-nm technology'. In: *Journal of Instrumentation* 19.01 (Jan. 2024), p. C01040. DOI: 10.1088/1748-0221/19/01/C01040. URL: https://dx.doi.org/10.1088/1748-0221/19/01/C01040.

[75] *Physics Beyond Collider, Annual Workshop*. 2024. URL: https://indico.cern.ch/event/1369776/.

[76] F. Acerbi et al. *nuSCOPE: A short-baseline neutrino beam at CERN for high-precision cross-section measurements*. 2025. arXiv: 2503.21589 [hep-ex]. URL: https://arxiv.org/abs/2503.21589.

[77] CERN. *Updated schedule for CERN's accelerators*. Oct. 4, 2024. URL: https://home.cern/news/opinion/accelerators/updated-schedule-cerns-accelerators (visited on 07/28/2025).

[78] SHiP Collaboration. 'A facility to search for hidden particles at the CERN SPS: the SHiP physics case'. In: *Reports on Progress in Physics* 79.12 (Oct. 2016), p. 124201. DOI: 10.1088/0034-4885/79/12/124201. URL: https://dx.doi.org/10.1088/0034-4885/79/12/124201.

[79] M. A. Jebramcik, P. Arrutia, and N. Charitonidis. *Ideas for a slow extraction via SPS LSS4 or LSS6 to a future PBC-SBN beamline*. Tech. rep. CERN, 2024. URL: https://cds.cern.ch/record/2918573.

[80] D. Manglunki. *Contribution PS/SPS User Meeting*. 2015. URL: https://indico.cern.ch/event/385590/contributions/912478/attachments/1155188/1660160/PS50_FE_SE_CT_MTE_v11.pdf.

[81] I. Efthymiopoulos et al. 'HiRadMat: A New Irradiation Facility for Material Testing at CERN'. In: (2011). URL: https://cds.cern.ch/record/1403043.

[82] F. Acerbi et al. *NP06/ENUBET annual report 2022 for the SPSC*. Tech. rep. co-spokesperson F. Terranova. Geneva: CERN, 2022. URL: https://cds.cern.ch/record/2805716.

[83] F. Iacob et al. 'ENUBET: a monitored neutrino beam for the precision era of neutrino physics'. In: *Journal of Physics: Conference Series* 2156.1 (Dec. 2021), p. 012234. DOI: 10.1088/1742-6596/2156/1/012234. URL: https://dx.doi.org/10.1088/1742-6596/2156/1/012234.

[84] F. Borgato et al. 'Characterisation of highly irradiated 3D trench silicon pixel sensors for 4D tracking with 10 ps timing accuracy'. In: *Frontiers in Physics* Volume 12 - 2024 (2024). ISSN: 2296-424X. DOI: 10.3389/fphy.2024.1393019. URL: https://www.frontiersin.org/journals/physics/articles/10.3389/fphy.2024.1393019.

[85] The DUNE Collaboration. 'Design, construction and operation of the ProtoDUNE-SP Liquid Argon TPC'. In: *Journal of Instrumentation* 17.01 (Jan. 2022), P01005. DOI: 10.1088/1748-0221/17/01/P01005. URL: https://dx.doi.org/10.1088/1748-0221/17/01/P01005.

[86] The DUNE collaboration. 'DUNE Phase II: scientific opportunities, detector concepts, technological solutions'. In: *Journal of Instrumentation* 19.12 (Dec. 2024), P12005. DOI: 10.1088/1748-0221/19/12/P12005. URL: https://dx.doi.org/10.1088/1748-0221/19/12/P12005.

[87] M. Barbi et al. *Proposal for A Water Cherenkov Test Beam Experiment for Hyper-Kamiokande and Future Large-scale Water-based Detectors*. Tech. rep. Geneva: CERN, 2020. URL: https://cds.cern.ch/record/2712416.

[88] M. A. Jebramcik et al. 'The latest design for a future short-baseline neutrino beamline'. English. In: *Proc. 16th International Particle Accelerator Conference* (Taipei, Taiwan). IPAC'25 - 16th International Particle Accelerator Conference 16. JACoW Publishing, Geneva, Switzerland, June 2025, pp. 960–963. ISBN: 978-3-95450-248-6. DOI: 10.18429/JACoW-IPAC25-TUPB009. URL: https://indico.jacow.org/event/81/contributions/7896.

[89] FLUKA Collaboration. *The official CERN FLUKA website*. Accessed: 2025-08-01. 2025. URL: https://fluka.cern.

[90] C. Ahdida et al. 'New Capabilities of the FLUKA Multi-Purpose Code'. In: *Frontiers in Physics* Volume 9 - 2021 (2022). ISSN: 2296-424X. DOI: 10.3389/fphy.2021.788253. URL: https://www.frontiersin.org/journals/physics/articles/10.3389/fphy.2021.788253.

[91] G. Battistoni et al. 'Overview of the FLUKA code'. In: *Annals of Nuclear Energy* 82 (2015). Joint International Conference on Supercomputing in Nuclear Applications and Monte Carlo 2013, SNA + MC 2013. Pluri- and Trans-disciplinarity, Towards New Modeling and Numerical Simulation Paradigms, pp. 10–18. ISSN: 0306-4549. DOI: https://doi.org/10.1016/j.anucene.2014.11.007. URL: https://www.sciencedirect.com/science/article/pii/S0306454914005878.

[92] G. Hugo et al. 'Latest FLUKA developments'. In: *EPJ Nuclear Sci. Technol.* 10 (2024), p. 20. DOI: 10.1051/epjn/2024023. URL: https://doi.org/10.1051/epjn/2024023.

[93] A. Donadon et al. 'FLAIR3 – recasting simulation experiences with the Advanced Interface for FLUKA and other Monte Carlo codes'. In: *EPJ Web Conf.* 302 (2024), p. 11005. DOI: 10.1051/epjconf/202430211005. URL: https://doi.org/10.1051/epjconf/202430211005.

[94] S. Roesler, R. Engel, and J. Ranft. 'The Monte Carlo Event Generator DPMJET-III'. In: *Advanced Monte Carlo for Radiation Physics, Particle Transport Simulation and Applications*. Ed. by Andreas Kling et al. Berlin, Heidelberg: Springer Berlin Heidelberg, 2001, pp. 1033–1038. ISBN: 978-3-642-18211-2.

[95] A. Fedynitch. 'Cascade equations and hadronic interactions at very high energies'. PhD thesis. KIT, Karlsruhe, Dept. Phys., Nov. 2015.

[96] T. J. Roberts et al. 'G4Beamline particle tracking in matter dominated beam lines'. In: *Proceedings of 2011 Particle Accelerator Conference, New York, NY, USA*. 2011, pp. 2776–2779.

[97] Special Metals Corporation. *INCONEL® Alloy 718*. Technical Bulletin, Publication Number SMC-045. 2010. URL: https://www.specialmetals.com/documents/technical-bulletins/inconel/inconel-alloy-718.pdf (visited on 07/30/2025).

[98] D. Baillard et al. *Design, development, and construction of the new beam stoppers for CERN's injector complex*. 2024. arXiv: 2408.01074 [hep-ex]. URL: https://arxiv.org/abs/2408.01074.

[99] A. Bertarelli. *Analytical Study Of Transient Thermal Stresses In Graphite Target Rods For Cern Neutrinos To Gran Sasso (CNGS) Facility*. Tech. rep. CERN, 2003. URL: https://edms.cern.ch/document/383454/1.

[100] Entegris, Inc. – POCO Materials. *Graphite Properties and Characteristics*. Technical manual on properties and characteristics of graphite. Entegris, Inc. 2020. URL: https://poco.entegris.com/content/dam/poco/resources/reference-materials/brochures/brochure-graphite-properties-and-characteristics-11043.pdf.

[101] The NA62 Collaboration. 'The beam and Detector of the NA62 experiment at CERN'. In: *Journal of Instrumentation* 12.5 (2017). ISSN: 17480221. DOI: 10.1088/1748-0221/12/05/P05025.

[102] NORMA - The CERN Normal Conducting Magnets database. *MAGNET DESIGN ID CARD: PXMBXHDCWP*. https://norma-db.web.cern.ch/magdesign/idcard/188/. Accessed: 2025-03-05.

[103] NORMA - The CERN Normal Conducting Magnets database. *MAGNET DESIGN ID CARD: PXMQNEFTWP*. https://norma-db.web.cern.ch/magdesign/idcard/335/. Accessed: 2025-03-05.

[104] NORMA - The CERN Normal Conducting Magnets database. *MAGNET DESIGN ID CARD: PXMQNFBTWC*. https://norma-db.web.cern.ch/magdesign/idcard/350/. Accessed: 2025-03-05.

[105] G. Mazzola and L. Salvatore Esposito. 'P42 T4/XTAX transmission efficiency - FLUKA'. In: (2023). URL: https://cds.cern.ch/record/2865692.

[106] HiRadMat Collaboration, CERN. *The HiRadMat Facility at SPS, CERN*. Accessed: 2025-08-01. 2025. URL: https://hiradmat.web.cern.ch/.

[107] M.W. Jr. Chase. *NIST-JANAF Thermochemical Tables, Fourth Edition*. 1998. DOI: 10.18434/T4D303. URL: https://doi.org/10.18434/T4D303.

[108] K. Zhang, E. Gaganidze, and M. Gorley. 'Development of the material property handbook and database of CuCrZr'. In: *Fusion Engineering and Design* 144 (2019), pp. 148–153.

[109] SpaceMatDB / ATI (Allegheny Technologies). *Grain-Oriented Electrical Steel – Technical Data Sheet*. Tech. rep. Version 1 (March 1, 2012). Accessed: 2025-08-02. SpaceMatDB / ATI, USA, 2012. URL: https://www.spacematdb.com/spacemat/manudatasheets/crgo.pdf.

[110] A. Bertarelli. 'Beam-Induced Damage Mechanisms and their Calculation'. In: *2014 Joint International Accelerator School: Beam Loss and Accelerator Protection*. 2016, pp. 159–227. DOI: 10.5170/CERN-2016-002.159. arXiv: 1608.03056 [physics.acc-ph].

[111] L. Xiaowei, R. Jean-Charles, and Y. Suyuan. 'Effect of temperature on graphite oxidation behavior'. In: *Nuclear Engineering and Design* 227.3 (2004), pp. 273–280. ISSN: 0029-5493. DOI: https://doi.org/10.1016/j.nucengdes.2003.11.004. URL: https://www.sciencedirect.com/science/article/pii/S0029549303003595.

[112] A. Ojha and A. Jain. '"Reliability Analysis of Nuclear Grade Graphite having Bimodularity"'. PhD thesis. Indian Institute of Technology (Banaras Hindu University) Varanasi, Nov. 2019.

[113] M. J. Boschini, P. G. Rancoita, and M. Tacconi. *SR-NIEL–7 Calculator: Screened Relativistic (SR) Treatment for NIEL Dose, Nuclear and Electronic Stopping Power Calculator (version 10.20)*. 2014. URL: https://www.sr-niel.org/ (visited on 08/13/2025).

[114] M. Addison et al. 'Characterisation of 3D trench silicon pixel sensors irradiated at $1 \cdot 10^{17}$ 1 MeV neq cm^{-2}'. In: *Frontiers in Physics* Volume 12 - 2024 (2024). ISSN: 2296-424X. DOI: 10.3389/fphy.2024.1497267. URL: https://www.frontiersin.org/journals/physics/articles/10.3389/fphy.2024.1497267.

[115] K. S. Krane and D. Halliday. *Introductory nuclear physics*. New York: Wiley, 1987. ISBN: 978-0-471-80553-3.

[116] E. Nowak and Ahdida C. *Radiation Protection Assessments for the nuSCOPE experiment (EDMS 3324948)*. Tech. rep. CERN, 2025. URL: https://edms.cern.ch/document/3324948/1.

[117] H. Vincke and C. Theis. 'ActiWiz 3 – an overview of the latest developments and their application'. In: *Journal of Physics: Conference Series* 1046.1 (June 2018), p. 012007. DOI: 10.1088/1742-6596/1046/1/012007. URL: https://dx.doi.org/10.1088/1742-6596/1046/1/012007.

[118] Swiss Confederation. *(ORaP) - Swiss Radiological Protection Ordinance (RPO)*. Jan. 1, 2022. URL: https://www.fedlex.admin.ch/eli/cc/2017/502/en.